LCF AND TMF CRACK GROWTH IN CAST NICKEL-BASED SUPERALLOYS

KME-702



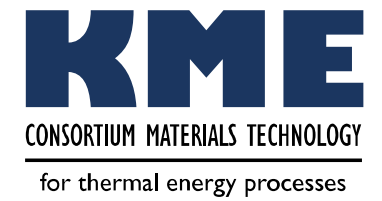




CONSORTIUM MATERIALS TECHNOLOGY for thermal energy processes







LCF AND TMF CRACK GROWTH IN CAST NICKEL-BASED SUPERALLOYS

KME-702

DANIEL LEIDERMARK
JOHAN MOVERARE
KJELL SIMONSSON
DAVID GUSTAFSSON
CHRISTIAN BUSSE
FRANS PALMERT

Preface

The project has been performed within the framework of the materials technology research programme KME, Consortium materials technology for thermal energy processes, period 2014-2018. The consortium is at the forefront of developing material technology to create maximum efficiency for energy conversion of renewable fuels and waste. KME has its sights firmly set on continuing to raise the efficiency of long-term sustainable energy as well as ensuring international industrial competitiveness.

KME was established 1997 and is a multi-cliental group of companies over the entire value chain, including stakeholders from the material producers, manufacturers of systems and components for energy conversion and energy industry (utilities), that are interested in materials technology research. In the current programme stage, eight industrial companies and 14 energy companies participate in the consortium. The consortium is managed by Energiforsk.

The programme shall contribute to increasing knowledge within materials technology and process technology development to forward the development of thermal energy processes for efficient utilisation of renewable fuels and waste in power and heat production. The KME goals are to bring about cost-effective materials solutions for improved fuel flexibility, improved operating flexibility, increased availability and power production with low environmental impact.

KME's activities are characterised by long term industry and demand driven research and constitutes an important part of the effort to promote the development of new energy technology with the aim to create value and an economic, environmentally friendly and long term sustainable energy society.

The industry has participated in the project through own investment (60 %) and the Swedish Energy Agency has financed the academic partners (40 %).

Bertil Wahlund, Energiforsk



Abstract

Within this project a method for conducting thermomechanical fatigue crack growth testing has been developed and verified. Two different types of cast nickel-based alloys for turbine blades has been investigated. One of them is a newly developed alloy specially designed for industrial gas turbines to meet the challenges with increasing renewable energy, that is, better corrosion resistance to cope with biofuels and better resistance to fatigue in order to manage the increasing number of start and stop cycles introduced when the use of other intermittent energy sources increases. For validation of the method also the traditional cast poly-crystalline superalloy IN792 has been investigated. Significant amount of material data has been generated and the failure mechanisms have been studied in detail.

The other main objective of this work has been to model the fatigue crack growth behaviour in single-crystal nickel-base superalloys. To achieve this, the influence of the crystal orientations on the cracking behaviour was assessed. The results show that the crystal orientation is strongly affecting the material response and must thus be accounted for. Furthermore, a linear elastic crack driving force parameter suitable for describing crystallographic cracking has been developed. This parameter is based on resolved anisotropic stress intensity factors and is able to predict the correct crystallographic cracking plane after a transition from a Mode I crack. Finally, a method to account for inelastic deformations in a linear elastic fracture mechanics context was also investigated. This method is based on the residual stress state from an uncracked finite-element analysis with an appropriate elastic-plastic material model and superimposed on the stress state in the corresponding cracked analysis with a linear elastic model during the determination of the crack driving force. The modelling work has been validated based on material testing of two different specimen geometries at different temperatures with good prediction of the experimental behaviour.



Sammanfattning

I dagens samhälle finns en allt större efterfrågan på gasturbiner för ökad cyklisk drift, vilka behövs som komplement till intermittenta förnyelsebara energikällor såsom soloch vindkraft. Eftersom stationära gasturbiner för energiproduktion traditionellt har designats för kontinuerlig baslast ger en sådan ändring i driftsvillkor, i termer av ökande antal start-stopp-cykler, en ökad risk för maskinell skada och driftstörning. Detta, tillsammans med krav på bränsleflexibilitet, gör att nya, mer korrosionsbeständiga, material och skyddsbeläggningar behöver introduceras i maskinerna.

I detta projekt har termomekanisk utmattningssprickväxt undersökts för två olika typer av gjutna nickelbaserade turbinbladsmaterial. Den ena av dem utgörs av en välbeprövad legering, medan det andra är ett nyutvecklat enkristallint turbinmaterial, speciellt framtaget för att möta ovan beskrivna krav, där dock avsaknaden av korngränser gör att sprickväxtbeteendet skiljer sig markant från konventionella material. Detta blir bland annat uppenbart då sprickan under vissa temperatur- och lastförhållanden kan byta till kristallografisk sprickväxt; ett beteende som utifrån ett tillämpningsperspektiv är oerhört centralt att kunna förstås och predikteras, och som därför legat i fokus i projektet.

Mekanisk provning och materialstudier har genomförts i projektet och använts för att ta fram förbättrade beräkningsmetoder och materialspecifika parametrar för sprickväxtprediktering i gasturbinblad. För verifiering av de framtagna nya prov- och beräkningsmetoderna, så har det ovan nämnda konventionella gastturbinmaterialet använts.

Projektresultat har avrapporterats i form av en större mängd vetenskapliga tidskriftspublikationer och konferensbidrag, och täcker alla inom projektet specificerade delområden. Resultat från projektet har också redan implementerats av SIEMENS Industrial Turbomachinery AB i dess designprocess för nya turbiner med fokus på bränsleflexibilitet och cyklisk drift.

Nykelord:

Spricktillväxt, gjutna nickelbaserade superlegeringar, termomekaniskutmattning, kristallografisk respons



Summary

Today, there is a growing demand for gas turbines for cyclical operation. These turbines are needed as a complement to the intermittent energy sources such as solar and wind power, which cannot be regulated in the same way as a gas turbine. Since gas turbines have traditionally been designed for base loads, a change in operating conditions, such as more start stop-cycles, will lead to an increased risk for damage and failure. In addition, the requirements for fuel flexibility also increases, which means that new and more corrosion-resistant materials and coatings must be introduced.

In this project, we have investigated crack growth during thermomechanical fatigue in two different types of cast nickel-based alloys for turbine blades. One of them is a newly developed alloy specially designed for industrial gas turbines to meet the challenges described above. As the alloy is a so-called single-crystal, completely without grain boundaries, crack growth differs significantly from conventional materials. Among other things, these materials show two distinctly different modes of crack propagation behaviour as the crack under certain load and temperature conditions changes to a crystallographic failure mode. In the project, this behaviour has been mapped for a variety of temperature and load conditions.

The results from material studies and mechanical testing have been used to develop a new calculation methodology and new fracture mechanics parameters for crack growth in material for gas turbine blades. To verify the new test and calculation methods developed within the project, a more traditional conventionally cast nickel-base alloy has also been studied.

Results from the project are already implemented by Siemens Industrial Turbomachinery AB, in their development of new turbines focusing on fuel flexibility and cyclical operation.

Keywords:

Crack growth, cast nickel-base superalloys, thermomechanical fatigue, crystallographic response



List of content

1	Introd	luction		10				
	1.1	Backg	round	10				
	1.2	Descri	ption of the research field	13				
	1.3	Goal		12				
	1.4	Projec	ct organisation	13				
2	Metho	ods		15				
	2.1	Mater	rials	15				
	2.2	Test s	pecimens	15				
	2.3	2.3 Isothermal Mechanical testing						
		2.3.1	DCT-specimen	17				
		2.3.2	Isothermal testing using the Kb-specimen	19				
	2.4	Therm	nomechanical fatigue crack growth testing	19				
		2.4.1	Optical crack length measurement	19				
		2.4.2	Crack length measurement by the compliance method	20				
		2.4.3	Stress intensity factor	23				
		2.4.4	Evaluation tool	26				
	2.5	Crack	driving force parameter	27				
		2.5.1	Crack opening force	28				
	2.6	micrus	structural investigations	28				
		2.6.1	Fracture surfaces	28				
		2.6.2	Crystallographic orientation and misalignments	32				
	2.7	Mode	lling	33				
		2.7.1	Finite element context	33				
		2.7.2	Crack growth anisotropy	34				
		2.7.3	Crystallographic crack driving force	34				
		2.7.4	Handling inelasticity	38				
	2.8	Comp	onent-near demonstrator	39				
		2.8.1	Test setup	40				
3	Result	s and a	nalyses	43				
	3.1	ISO th	ermal results and analyses – DCT specimen	43				
		3.1.1	DCT results at 20°C	43				
		3.1.2	DCT results at 500°C	48				
		3.1.3	DCT results at 750°C	52				
		3.1.4	Summary of fracture appearance	55				
		3.1.5	Influence of crystal orientation	55				
		3.1.6	Influence of temperature	56				
		3.1.7	Influence of hold time	57				
	3.2	TMF C	Crack growth results and analyses	59				
		3 2 1	IN792 IP-TMF compared to isothermal results	50				



		3.2.2	IN792 OP-TMF		62
		3.2.3	IN792 crack propagation mechanisms		62
		3.2.4	STAL15 SX IP-TMF compared to isother	mal results	63
		3.2.5	STAL15 SX OP-TMF		64
		3.2.6	Influence of long term ageing on TMF p	properties of STAL15	64
	3.3	Mode	lling results		65
		3.3.1	Numerical study of the influence of cry and misalignments	stallographic orientation	65
		3.3.2	Crystallographic crack driving force		69
4	Conclu	usions			75
5	Goal f	ulfilme	nt		77
6	Sugge	stions f	or future research work		78
	6.1	Experi	mental work		78
	6.2	Mode	lling work		78
7	Litera	ture ref	erences		80
8	Public	ations			82
9	Apper	ndices		Fel! Bokmärket är inte definier	rat.



1 Introduction

1.1 BACKGROUND

Due to the intermittent nature of renewable energy sources like solar and wind power, there is a need for flexible backup power for balancing the grid, a task well suited for gas turbine and combined cycle power plants. However, these increased demands on cyclic capacity and reduced start up times, in combination with increased demands on higher temperatures and fuel flexibility, calls for improved material knowledge and life prediction methodologies to ensure structural integrity of key components of these machines. It is here to be noted that structural components in gas turbines, as well as in steam turbines, are subjected to rather complex stress and temperature cycles due to the temperature gradients that occur during engine start-up and shut-down or within components during steady-state operation. The accumulated effect of such stress and temperature cycles leads to the possibility of failure by thermomechanical fatigue (TMF), which must be avoided by appropriate design of the components and choice of operating conditions. However, the service life of many hot components is not fully restricted by the number of cycles to crack initiation since, especially close to stress concentrations; one has also to rely on stable and predictable crack propagation, which means that a certain amount of crack propagation is allowed before the component has to be replaced in service. Such damage tolerant approaches demand accurate predictions of the fatigue crack propagation (FCP) under the influence of simultaneous cycling of temperature and mechanical loads. Although methods have been developed to predict FCP rates under isothermal conditions over a wide range of temperatures, frequencies and load ratios, as well as under sustained load/dwell times, only very few published studies on crack propagation under TMF conditions are available. Furthermore, since the translation of isothermally obtained fatigue crack propagation data into a true TMF context is questionable, the need for more experimental studies in this field is obvious. Unfortunately, mechanical testing under dynamic temperature conditions is more complex than other more traditional isothermal testing techniques.

Crack propagation in single-crystal materials add an extra dimension of complexity since the failure modes are complicated due to the material anisotropy, the effect of crystal orientation and the very high temperatures that are typically of interest for single-crystal components. In addition, previous studies within KME-403, KME-410 and KME-502 have shown that the deformation in single-crystal materials is often very localized to a number of crystallographic deformation bands and that cracks follow these bands very easily. Thus, the cracks cannot be expected to follow the Ki-dependency (i.e. crack growth perpendicular to the applied load) commonly observed in conventional materials.

Based on the above described indutrial needs, previous work and current state of knowledge (cf. next section), the here reported project has focused on the following two goals of the KME-programme:

"To test and validate new materials and surface coatings for future industrial gas turbines in order to permit high fuel flexibility, availability and efficiency, as well as cyclic operation."

"To evaluate the mechanical properties and service life of various materials in relation to new material requirements for more efficient electricity production"



Furthermore, two different materials have been investigated in the project; (1) Conventionally cast IN792 which is commonly used in turbine blades for industrial gas turbines, (2) the newly developed single-crystal material STAL15.

In what follows, after a first description of the research field and project tasks, goals and organisation, the project results will be presented and discussed. Finally, conclusions will be drawn, goal fulfillment discussed and suggestions for future research work presented.

1.2 DESCRIPTION OF THE RESEARCH FIELD

The fatigue process in single-crystal nickel-base alloys are, despite the absence of grain boundaries, remarkably complex. Both crystallographic and non-crystallographic fracture modes are observed where their occurrence is depending upon temperature and stress-state. Crystallographic fracture is usually along multiple {111} planes but can, under certain conditions, appear as cleavage along cubic (001) planes. The later behaviour can often be associated with environmental effects, such as hydrogen embrittlement or sulphidation [1][2]. Studies have also shown that TMF cracks of single-crystal nickel-base alloys have different appearances depending on whether a compressive hold time at maximum temperature was introduced or not [3]. The introduction of a hold time in compression promotes the formation of twins and according to the findings in the previous KME-projects, crack propagation occurs rapidly along these twin planes [4][5][6]. This indicates that the deformation introduced in the material prior to the crack initiation is an important factor for

Kersey et al. [7] have studied out-of-phase (OP) TMF crack growth from laser drilled holes in the single-crystal alloy PWA1484. In this study it was found that major crack propagation took place at the low temperature portion of the cycle but there were also noticeable damage accumulation during the high temperature compressive load portion of the cycle. As a consequence it was found that crack propagation under TMF loading conditions is faster than corresponding isothermal LCF crack growth at similar temperature and loading conditions as for the tensile part of the TMF cycle. Furthermore, in this study is was found that the cracks started at the holes and initially propagated crystallographically and later changed to a non-crystallographic mixed mode growth.

Okazaki et al. [8] performed fatigue crack growth experiments at room temperature on the single-crystal alloy CMSX-4 with different primary and secondary orientations of the single-crystal relative to the specimen configuration and applied load. On the basis of apparent Mode I stress intensity factor range, the [001] specimens revealed the highest rates and the [111] specimens the lowest. However, the fatigue fracture was driven on the crystallographic {111} slip planes in all specimens. However, the dependency of crystallographic orientation almost disappeared when the rates instead were correlated to the stress intensity for shear mode fracture.

Bouvard et al. [9] have proposed a crack growth model for single-crystal superalloys at high temperatures that follows the framework of classical linear elastic fracture mechanics (LEFM) that can capture time dependent mechanisms such as creep-fatigue and oxidation-fatigue interactions. The model was also verified against TMF tests but the effect of different crystallographic orientations were not taken into consideration. Others like Zhao et al. [10] have considered elastic-plastic fracture mechanics (EPFM) parameters such as the J-integral and COD in the context of anisotropy and notch orientation of single-crystal superalloys.



Single-crystal superalloys often display significant rafting, i.e. directional coarsening of the strengthening particle γ' [11]. Compressive loading at high temperature, as typically seen for OP TMF, leads to rafting parallel to the loading axis. Neuner et al. [12] have shown that this will enhance the TMF life since rafts along the loading direction will hinder crack propagation.

As shown by the examples above crack propagation in single-crystal superalloys is a complex phenomenon and so far no unified model that takes all kind of microstructural and environmental effects into account is available. Thus, the need for more work in this field is necessary.

1.3 GOAL

The overall goal of the here reported research project has been to address and solve material related research questions central for the next generation of advanced gas turbines, and in this way contribute to the development towards a sustainable and efficient global energy system.

The specific goal of the project has been to validate materials and lifing methods for future industrial gas turbines where there is a strong need for high fuel flexibility, availability and efficiency, as well as cyclic operation, with main focus on TMF loading situations and single-crystal materials.

The following project goals have been defined and carried out. Each task is further elaborated in what we mean with them.

- 1. Validation of a TMF crack growth test method that can be used to generate high quality data for cast nickel-based superalloys, including single-crystals.
 - As there is no standard for how to do TMF-crack growth testing we must be confident that our method can generate reliable and satisfactory results. This can be done by scrutinizing the results from many different aspects, i.e. repeatability, amount of scatter, consistency between different test conditions and comparison with isothermal data.
- 2. Generation of high quality test data for TMF crack growth in conventionally cast IN792 and the single-crystal superalloy STAL15.
 - The amount of data generated in the project should be enough in order to generate at material model that can describe the general material behaviour under relevant temperarures and load conditions.
- Improvement of the knowledge regarding the mechanisms that controls the crack growth rate for conventionally cast superalloys as well as for single-crystal superalloys (e.g. influence of crystal orientation, phase shift and temperaturestrain history).
 - As the research project progresses, knowledge with respect to the above mentioned goal and underlying phenomna will be gained.
- 4. Development of TMF crack growth models and life prediction methodologies that will reduce the need high safety margins. Today the safety of single-crystal crack growth is in the order of three decades. The idea is to bring this order of magnitude down by one decade.



To predict the life of a single-crystal component, a crack growth model is needed to evaluate the observed cracking behaviour. A working methodology will, in turn, contribute in reducing the conservative safety margin of today, through increased knowlegde about the driving force.

5. Validation of the models for component near conditions.

More specifically, a validation of the crack growth methodology on a component like geometry with an engine relevant load cycle is to be performed.

1.4 PROJECT ORGANISATION

The project has been conducted in collaboration between the divisions of Engineering Materials and Solid Mechanics at Linköping University (LiU) and Siemens Industrial Turbomachinery AB in Finspång (SIT).

The responsibilities for the different partners is briefly summarised below:

LiU - Engineering Materials:

- Project lead
- Metallography
- Mechanical testing (TMF and crack growth)

LiU – Solid Mechanics:

- Modelling and evaluation of test results
- Implementation of crack growth models

Siemens Industrial Turbomachinery AB:

- Mechanical testing (LCF, TMF, Creep and crack growth)
- Supply of test materials
- Test of in-service like set-up (component)

The activities at Linköping University have mainly been carried out by Ph.D. students, which, so far, have generated one Licentiate of Engineering-degree. A second Licentiate of Engineering-degree is planned for in October 2018.

The total budget for the project has been 14.435.480 SEK, by which 5.735.480 has been funded by KME.

The key personnel involved in the project are listed below:

Key role	Personnel
Project manager	Prof. Johan Moverare, LiU
Reference group	Associate Prof. Magnus Colliander (Hörnqvist), Chalmers Dr. Rikard Norling, Swerea KIMAB



Supervisor group	Prof. Johan Moverare, LiU					
	Associate Prof. Daniel Leidermark, LiU					
	Prof. Kjell Simonsson, LiU					
	Dr. David Gustafsson, SIT					
	Lic. Eng. Björn Sjödin, SIT					
Ph.D. students	Lic. Eng. Christian Busse, LiU					
	M.Sc. Frans Palmert, SIT					

Role descriptions:

Project manager

- · Ensure that the boundaries of scope are kept.
- · Follow up budget.
- · Follow up on deliverables.
- · Call for meetings and reviews.

Reference group

- · To secure resources to the project and commitment for the solution.
- · Provide overall guidance and decisions.
- · Follow up on progress, budget and compliance to project targets.
- · Key competence and project guidance to ensure that the project results are useful for the participating company and the academia.

Supervisors

· Will plan scientific work and support the Ph.D. students.

Ph.D. students

· Key role for the project. Will participate in all planning and decisions regarding the project.



2 Methods

2.1 MATERIALS

One of the tested material is an alternative single-crystal nickel-base superalloy developed by Siemens Industrial Turbomachinery AB, similar to the alloy described in a publication by Reed et al [13]. Its main alloying elements, in order of decreasing wt%, are as follows: Ni-Cr-Ta-Co-Al-W-Mo-Si-Hf-C-Ce. The microstructure mainly consists of a γ -matrix precipitation strengthened by approximately 50 vol% of γ' -particles. The majority of the γ' is in the form of primary cuboidal particles, but smaller secondary γ' particles are also present within the γ -channels. In addition, the microstructure also contains carbides and casting pores.

The other material of interest has been IN792, a conventional cast γ' -precipitation hardened nickel-based superalloy. The chemical composition is Ni–12.4Cr–8.9Co–1.8Mo–4.0W–3.5Al–4.0Ti–4.1Ta–0.08C–0.017B–0.019Zr (wt.%). After conventional casting the material was hot isostatically pressed (HIP) at 1195 °C and 150MPa for 2 h followed by solution heat treatment at 1121 °C for 2 h and ageing at 850 °C for 24 h. Typically the grain size is rather large and a lot of carbides are formed at the interdendritic areas, carbides together with borides can also be observed in the grain boundaries. The primary γ' -phase typically has a size about 0.6–0.7 μ m and can have both an irregular and a cubic appearance. In addition, much smaller secondary γ' -particles are also present along with larger γ/γ' eutectic domains.

2.2 TEST SPECIMENS

Three different test specimen geometries for crack propagation testing has been used within project. They are briefly described below.

Isothermal crack growth testing has been performed on the single-crystal material using disk shaped compact tension (DCT) specimens. The specimens were extracted, in three different crystallographic orientations, from a round bar with a diameter of 25mm, see Figure 1. The side surfaces of the specimens were polished down to 2400 grit paper. Precracking was performed at room temperature using the compliance method for determination of the crack length. At elevated temperature, crack growth was monitored by direct current potential drop (DCPD).

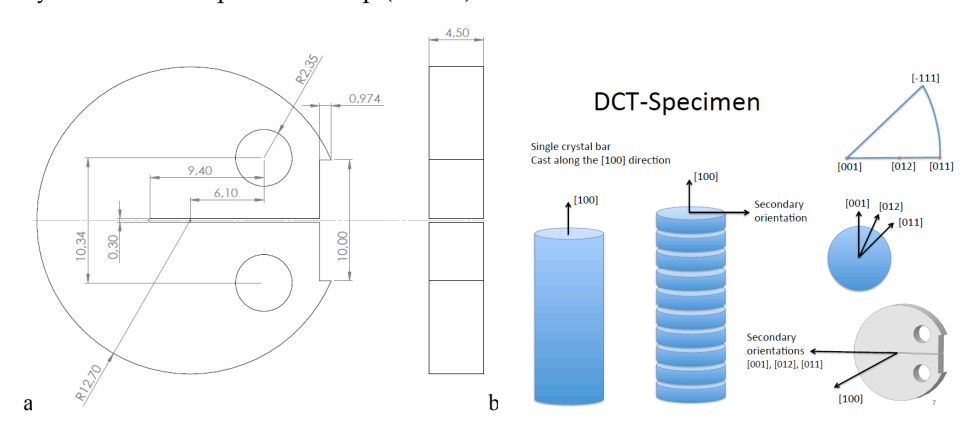


Figure 1: (a) Drawing of DCT specimen in units of mm. (b) Description of test specimen extraction.



Isothermal fatigue crack growth tests were performed on both materials using a Kb-type (surface crack) specimen with rectangular cross sections of 4.3×10.2 mm, see Figure 1. The initial notch was created by electro discharge machining (EDM), and the subsequent pre-cracking was done at room temperature. Crack growth was monitored by direct current potential drop (DCPD).

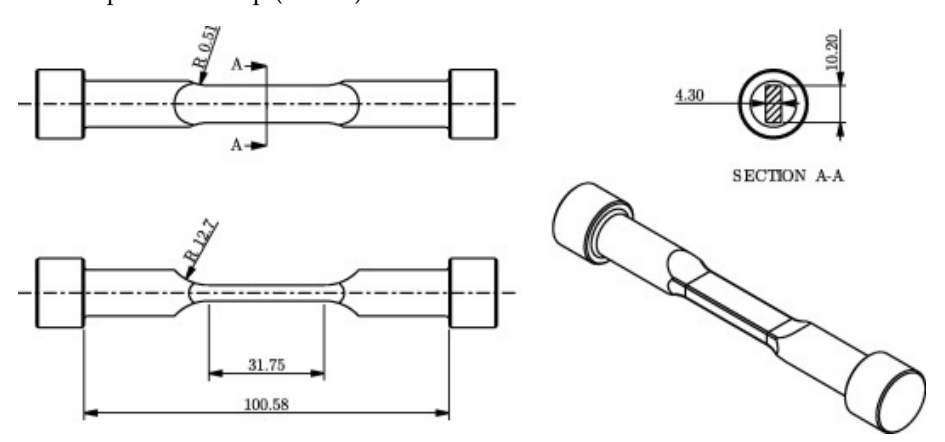


Figure 2: Drawing of Kb-specimen with the rectangular cross section, dimensions in mm.

Thermo-mechanical fatigue crack growth testing was performed on both materials using a single-edge notched (SEN) specimen geometry, seen in Figure 3. Crack growth was monitored using the compliance method as outlined in ASTM E647 and further modified by Ewest et.al. [14].

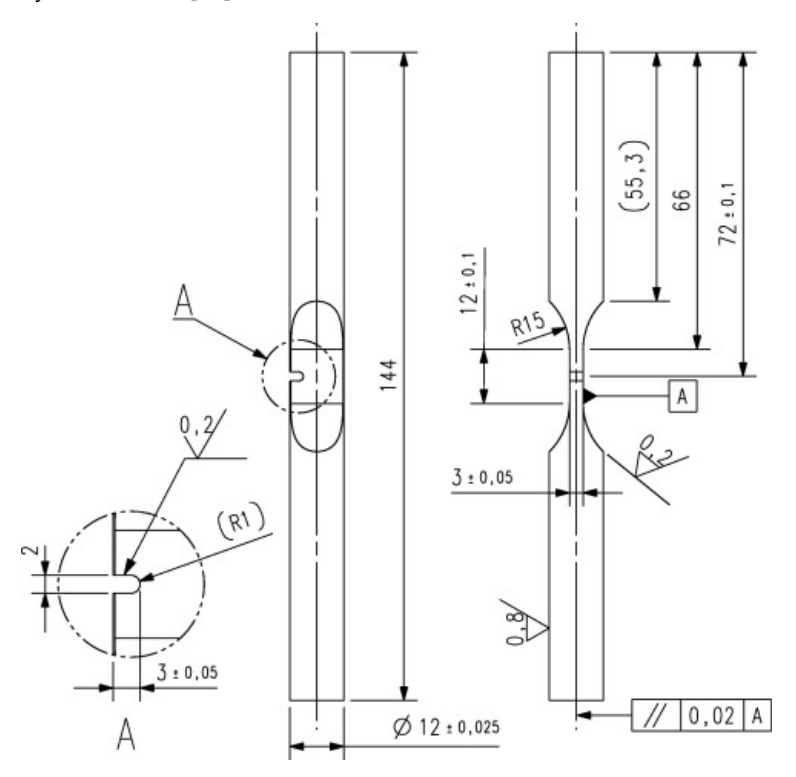


Figure 3: The SEN specimen geometry used for TMF crack growth testing, units given in mm.



2.3 ISOTHERMAL MECHANICAL TESTING

2.3.1 DCT-specimen

Fatigue crack growth testing of STAL15 SX was performed according to ASTM E647. Tests were run at 20°C, 500°C and 750°C with stress ratio R=0.1. The specimens had an Electro Discharge Machined (EDM) starter notch and were fatigue pre-cracked at room temperature with a frequency of 10 Hz. During the pre-cracking and room temperature testing, the crack opening displacement was measured using a clip gauge extensometer and the crack length was determined by the compliance method described in ASTM E647. The fatigue crack growth tests at elevated temperature were run in a 100kN Zwick servo-electric tensile testing machine (Kappa 50DS), with a three zone furnace. The tests at 500°C were run with a hold time of 30s at maximum force in each cycle. At 750°C tests were run with 30s, 1h and 24h hold time at maximum force. The hold times were varied in blocks within the same test. The crack length was monitored using pulsed direct current potential drop measurement (DCPD). The crack length was calculated from the DCPD signal following Johnson's formula for the CT specimen

$$a/W = \frac{2}{\pi} \cos^{-1} \left[\frac{\cosh(\pi Y_0 / 2W)}{\cosh \left[\frac{V}{V_0} \cosh^{-1} \left\{ \frac{\cosh(\pi Y_0 / 2W)}{\cos(\pi a_0 / 2W)} \right\} \right]} \right]$$

where a is the crack length, W is the specimen width, a_0 is the reference crack size, with respect to the reference voltage V_0 , Y_0 is half the distance between the output voltage leads and V is the output voltage. The initial crack size a_0 was taken as the average of the crack length obtained from the compliance at the end of pre-cracking and the optically measured crack length at the specimen surfaces. The optically measured crack length was obtained as an average of two measurements, one at each side of the specimen.

Stress intensity factor for non-crystallographic cracks

The mode I stress intensity factor (*K*) for the DCT specimen was calculated based on the equations by Newman included in ASTM E399 [15]. It has been reported by Chan et al. [16] that the elastic anisotropy of MAR-M200 single-crystals has no significant influence on *K* for mode I cracks in CT specimens. However, more recent work by Tinga [17] has indicated that the use of isotropic *K* solutions for CMSX-4 single-crystal corner crack specimens is inappropriate, since the anisotropy has a significant influence on the local stress distribution around the crack tip.

In the present work, simulations have been performed in order to evaluate the influence of crystal orientation on *K* for the DCT specimen. The simulations were performed in the FE-environment Abaqus V6.12 and coupled with the crack growth tool FRANC3D V7.0.5, which is used to subsequently grow the crack and remesh the FE-model. In FRANC3D, the stress intensity factors are calculated by the LEFM M-Integral. All simulations were performed in a 3D-context and an elastic anisotropic material description was used in order to handle the anisotropic material behaviour. Three ideal crystallographic orientations were simulated, i.e. <001>, <011> and <012>, representing the experiments. The procedure to insert, grow and evaluate the stress intensity factors corresponds to Method 1 presented in the modelling section of this report where it is thoroughly explained. Furthermore, a simulation with isotropic material behaviour was



performed for the sake of comparison. For the isotropic reference case, the calculated *K* as a function of crack length agrees fairly well with the *K* solution by Newman, see Figure 4. The presently calculated *K* for the isotropic case is approximately 7% higher than the isotropic *K* solution by Newman. In the same figure, it can also be seen that the difference in *K* between the different crystal orientations is small. The presently calculated *K* for the anisotropic cases is 19-27% higher than the isotropic *K* solution by Newman for identical crack lengths, depending on crack length and crystal orientation. For the sake of comparability with previous work, the isotropic *K* solution by Newman is used for all crack growth rate evaluations in the present work.

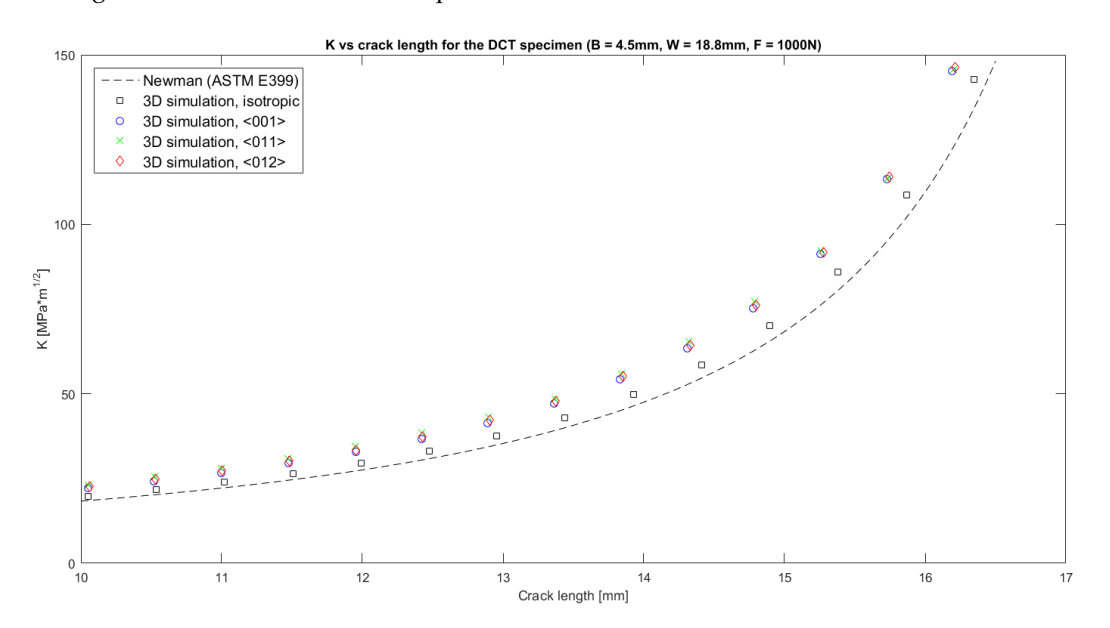


Figure 4 – K vs a for the DCT specimen at 1000N. Present simulation results compared with the K solution from ASTM E399.

Partly crystallographic cracks

In some tests performed in the present work, crystallographic crack growth along [111] planes were observed. In these tests, the crystallographic crack growth was limited to certain parts of the crack front. The central part of the crack front remained noncrystallographic and perpendicular to the loading direction throughout all tests. The abovementioned K solution does not provide an adequate description of the driving force for crack growth in cases where a significant fraction of the crack is crystallographic. However, the crack growth rate was monitored by potential drop measurement also during crystallographic crack growth. The crack length measured by potential drop correlates with the remaining uncracked ligament of the specimen, which means that the measured crack length is approximately equal to the average projected crack length in the direction perpendicular to the loading direction. Based on the crack length measured by potential drop it is possible to apply Newman's K solution, in spite of its questionable applicability, and thereby evaluate the crack propagation rate da/dNvs the stress intensity factor range ΔK also for the partly crystallographic cracks. In the results section this evaluation of crack growth rates is included for comparison. The results for partly crystallographic cracks are plotted as dashed lines in order to indicate that the physical basis for the evaluation of these results is questionable.



2.3.2 Isothermal testing using the Kb-specimen

Fatigue crack growth testing of surface flawed Kb specimens in material IN792 and STAL15 SX was done according to the guidelines provided in the ASTM E647-15 test specification. The fatigue crack growth testing was done at temperatures of 500°C, 750°C and 850°C using a triangular waveform with 1s ramp up time and 1s ramp down time. Testing with hold times of 1h and 6h at maximum load was done at 750°C and 850°C. At these temperatures some static load crack growth tests were also performed. The tests were run in an MTS servo-hydraulic testing machine with a test capacity of 89kN. Prior to testing, a semi-circular surface flaw was introduced by electro discharge machining (EDM). The notch was centered on one of the large surfaces of the specimen gauge section. The test specimens were then fatigue pre-cracked to the desired initial crack length. The crack length was monitored using direct current potential drop measurement (DCPD). The specimens were heat tinted at least 3 times during the test, in order to mark the crack front and enable calibration of the potential drop measurement.

2.4 THERMOMECHANICAL FATIGUE CRACK GROWTH TESTING

TMF crack growth testing on IN792 and STAL15 SX was performed using the notched SEN-type specimen seen in Figure 3. For most test on STAL15 SX the nominal crystal orientation was <001> in the axial direction and <010> in the crack depth direction.

The TMF crack growth testing was performed at Siemens in Finspång using an MTS 810 servo-hydraulic machine, with a 100 kN load cell with. The gauge length of the extensometer was 12 mm. The specimen was heated by a 2-1-2 "barrel-shaped" induction coil, as can be seen in Figure 5. The specimen was cooled by compressed air from two cooling nozzles. A similar set-up has also been established at LiU.



Figure 5 - Test set-up for TMF crack growth testing at Siemens, Finspång.

2.4.1 Optical crack length measurement

A camera was used to monitor the crack and record images from one side (front) of the specimen (see Figure 6). An image is recorded automatically at pre-defined cycle intervals. On the opposite (back) side of the specimen, there is no automatic recording of images, however for tests performed in Finspång, photographs were taken manually in order see if there was a significant difference in the size and shape of the crack on the two sides. Prior to testing, reference scribes have been placed on the surface of the specimen in order to facilitate the crack length evaluation. The optical crack length measurements were generally not used in the evaluation of crack growth rate, since this



was done based on the crack length from the compliance method. The optical crack length measurements were mainly used to facilitate the control of the tests and to verify the results from the compliance method. During isothermal pre-cracking, the live view of the camera was used to determine when the pre-crack had reached its desired length.

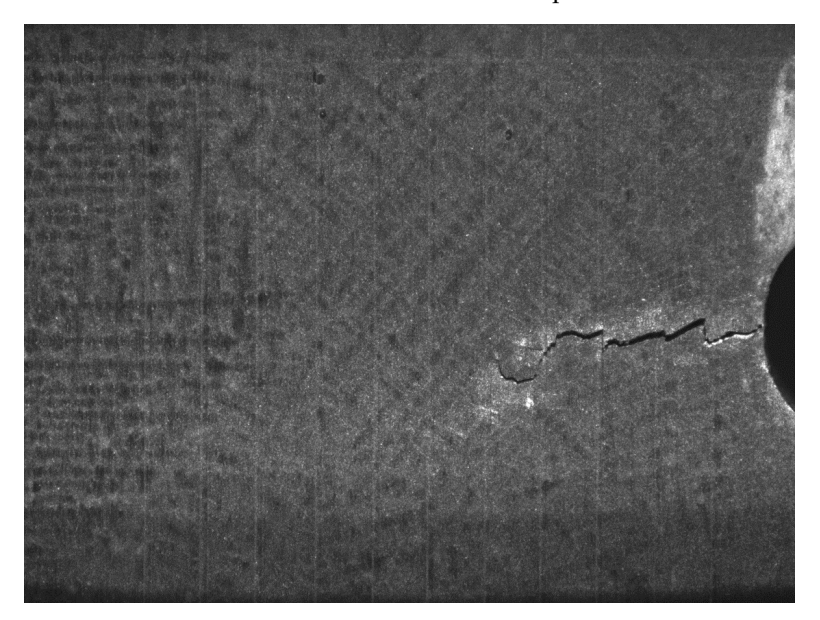
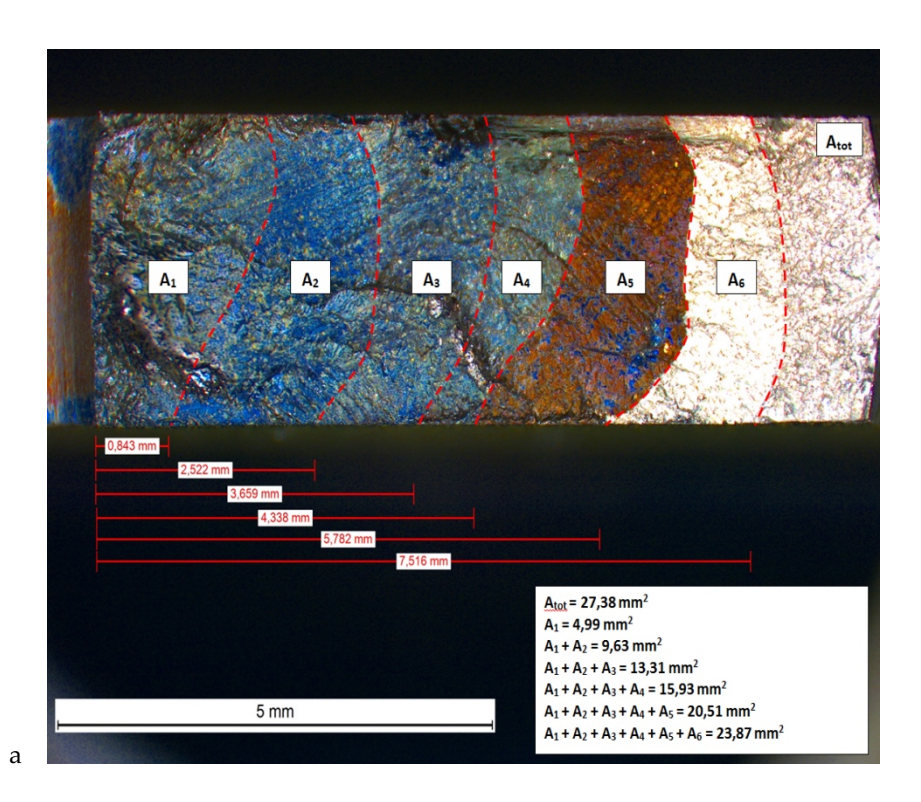


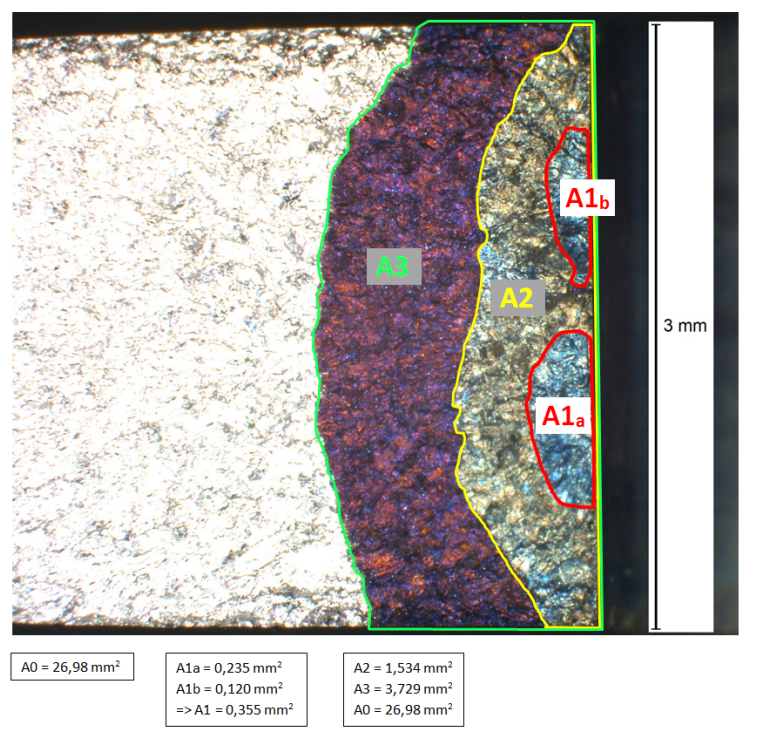
Figure 6 - Image taken during an OP 100-750°C on IN792.

2.4.2 Crack length measurement by the compliance method

The crack length in each cycle was determined using the compliance method, adapted for TMF conditions. A detailed description of the method has been published by Ewest et al. [14]. The relationship between the relative stiffness decrease and the crack length (average along the crack front) was obtained from a simulation in FRANC3D/Abaqus, see solid line in Figure 8. The simulation was verified by measurements of the crack length on the fracture surfaces of tested specimens, see markers in Figure 8. Measurements were made both of the final crack front and on crack fronts marked by heat tinting, see Figure 7). The average crack length along the crack front was determined from at least 5 measurements or calculated thru area measurements. Figure 8 shows the results for specimen geometry according to drawing in Figure 3. The applicability of this compliance curve was verified by comparing da/dN evaluated by the compliance method with da/dN evaluated based on optical measurements, see Figure 9. For the optical evaluation, crack length measured at the side surface of the specimen was corrected to match the final crack length measured on the fracture surface (average along the crack front), see Figure 10.







b

Figure 7 – Crack length measurements on the fracture surface of specimen tmf3911 (a) and specimen tmf3833 (b).

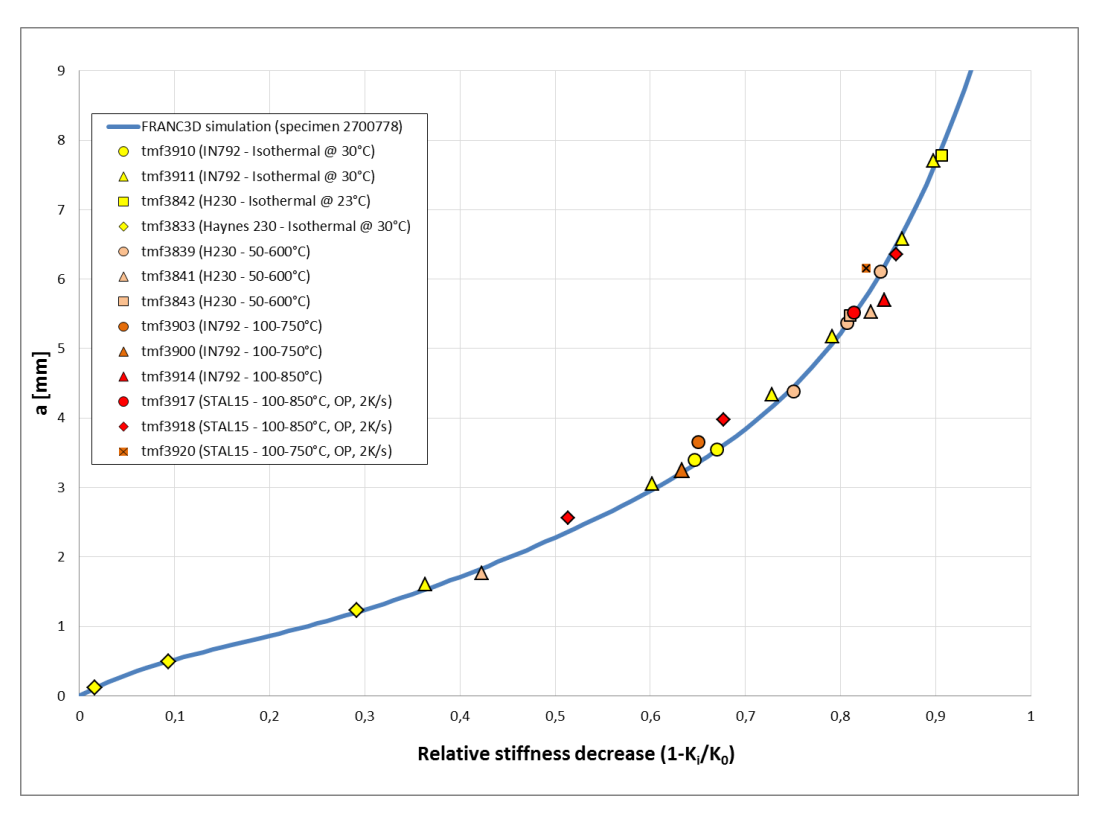


Figure 8 – Crack length vs relative stiffness decrease. Compliance calibration curve for specimen 2700778.

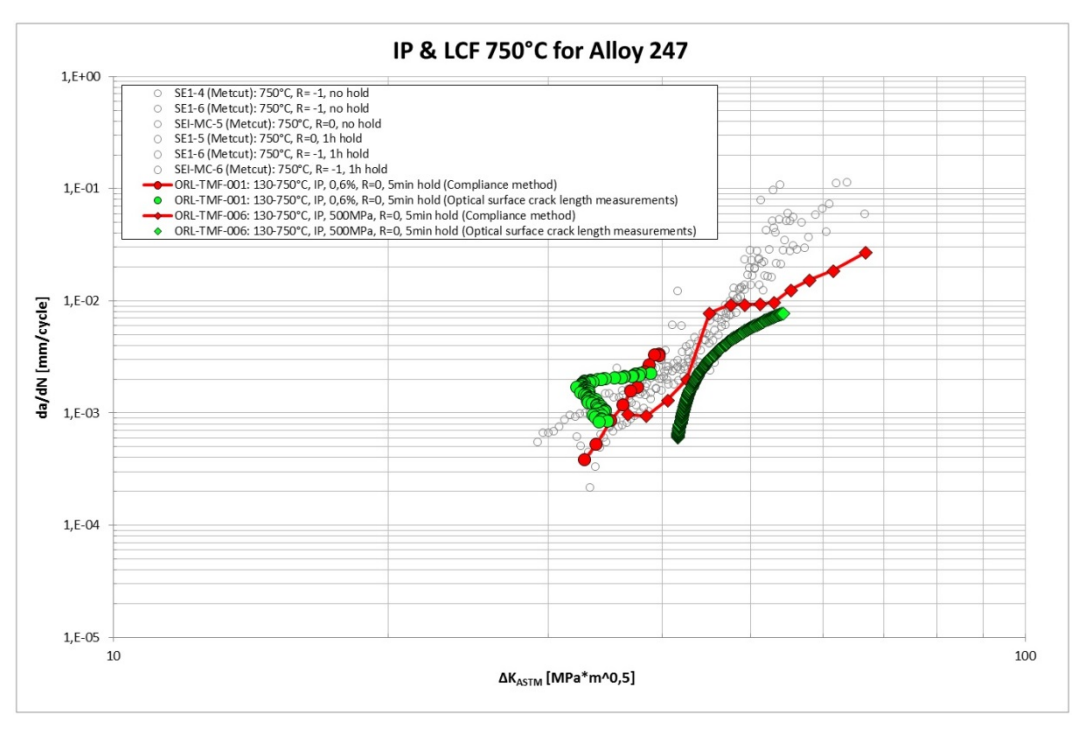


Figure 9 – Comparison between compliance evaluation and optical crack length evaluation.



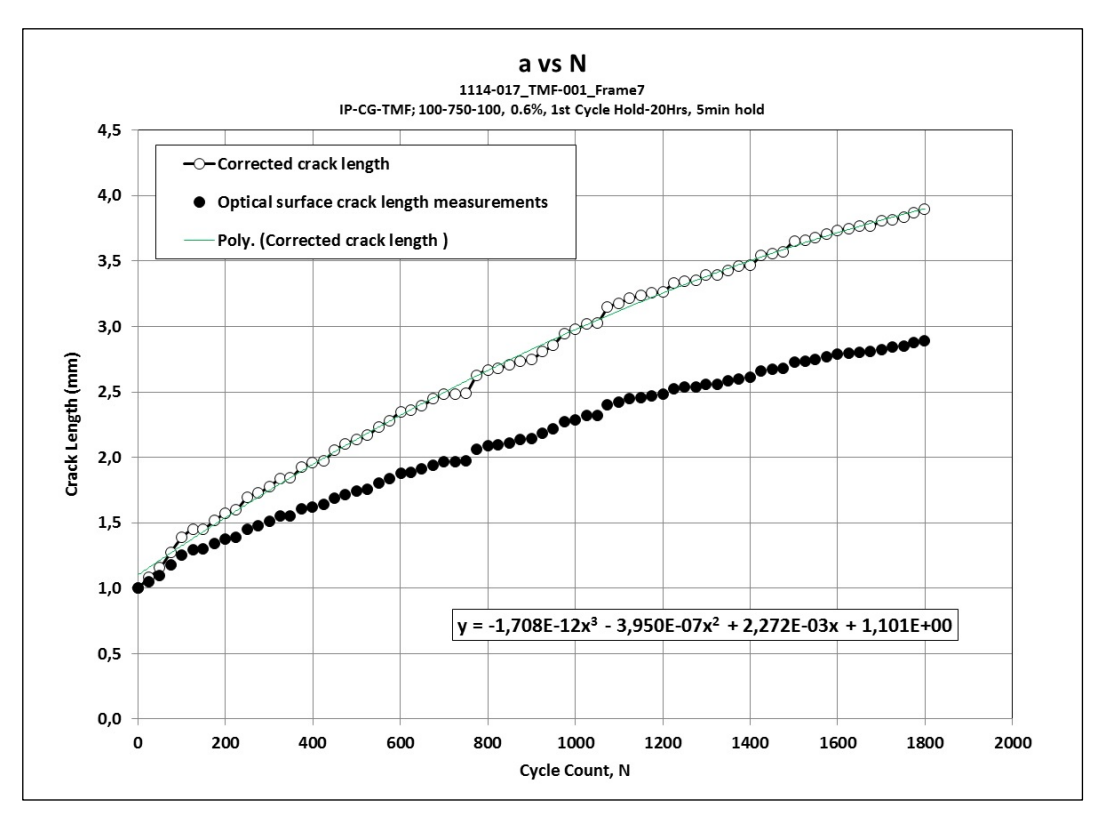


Figure 10 – Example of correction of the crack length measured at the side surface of the specimen to match final crack length measured on the fracture surface.

2.4.3 Stress intensity factor K

For the single-edge notch specimen, no previous satisfactory stress intensity factor (SIF) solutions were available and had to be derived. The simulations were performed in the FE-environment Abaqus V6.12 and coupled with the crack growth tool FRANC3D V7.0.5, which is used to subsequently grow the crack and remesh the FE-model, where the SIFs are calculated by the LEFM M-Integral. All simulations were performed in a 3D-context, see Figure 11.

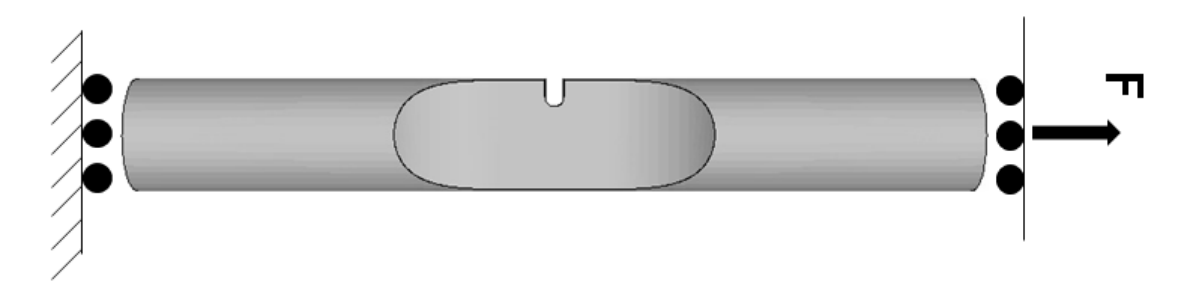


Figure 11: Model of SEN specimen for TMF crack growth with applied boundary conditions.

The FE model was loaded with a concentrated force at reference point. The loaded side of the specimen is free to contract but all nodes move equally in the loading direction. On the constrained side the surface, nodes are constrained in the axial direction to a fixed reference node but the surface is allowed to contract freely.



The cracks are modelled with straight crack fronts and planar with respect to crack surface, see Figure 12.

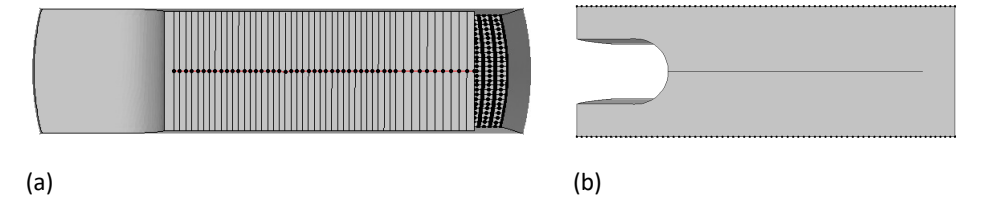


Figure 12: a, Showing the modelled straight crack fronts. b, Showing the planar crack

The SIFs was evaluated in 3 paths 0.25, 0.5 and 0.75, see Figure 13. The stress intensity factor *K* is varying over the crack front and the crack length *a* varies slightly depending on path, see Figure 14. Thus, a mean value was calculated both for *a* and *K*.

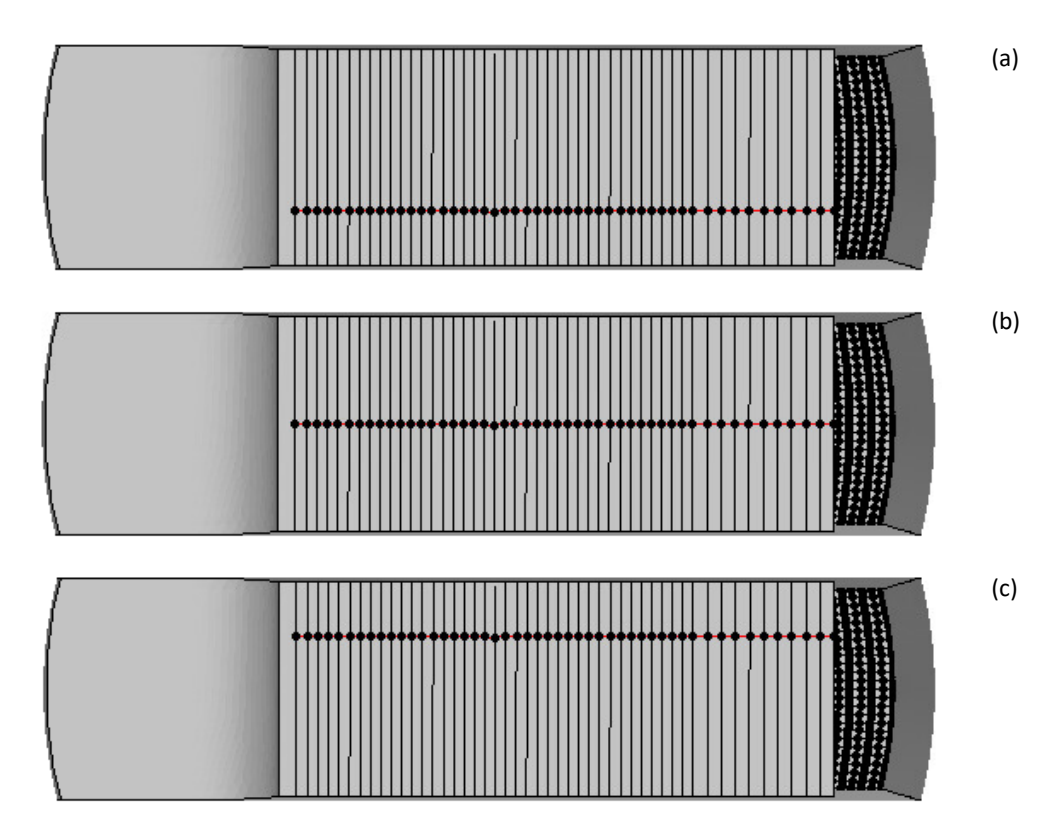


Figure 13: a, Showing path 0.25. b, Showing path 0.5. c, Showing path 0.75



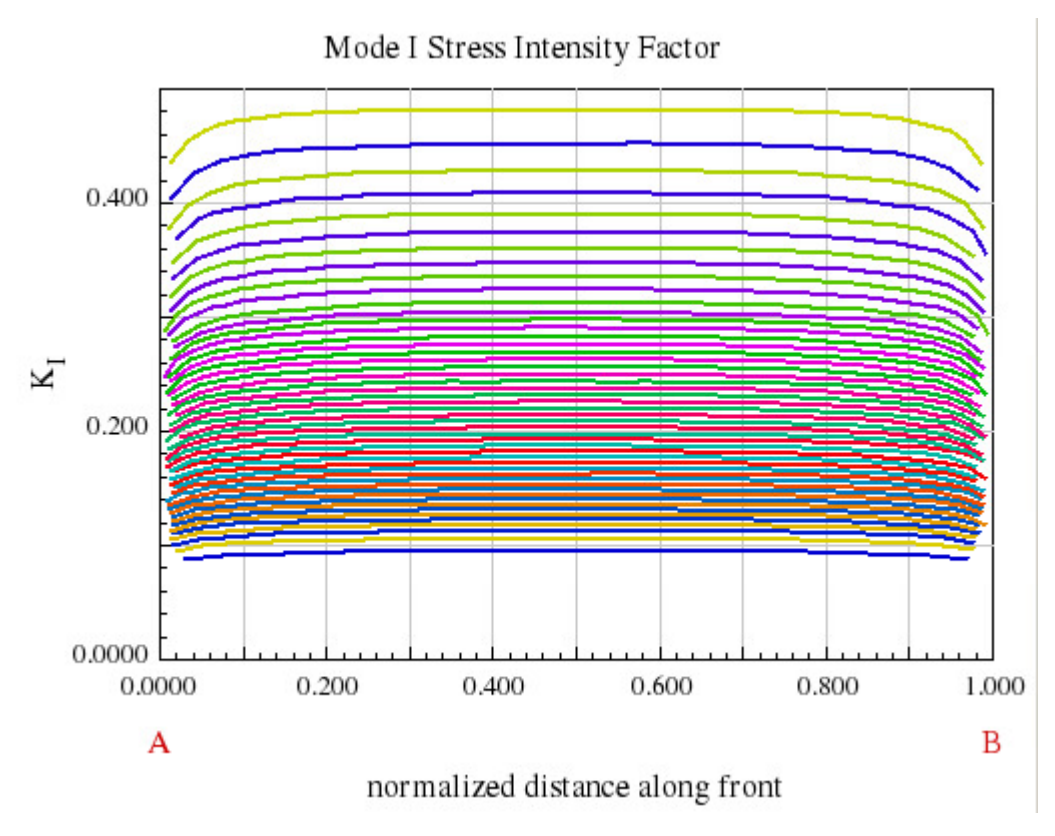


Figure 14: K as a function of normalized distance along crack front for all evaluated crack fronts.

The mean values of the stress intensity factor K and the crack length a are used for obtaining f(a), see the equation below

$$K = \sigma \sqrt{\pi a} \cdot f(a)$$

Where K is the stress intensity factor, σ is the stress, a is the crack length and f(a) is the geometry function. σ and a are defined according to Figure 15 on the test specimen.

Results for f(a) for are shown in Figure 16. These functions are implemented in the evaluation tool described later this report.

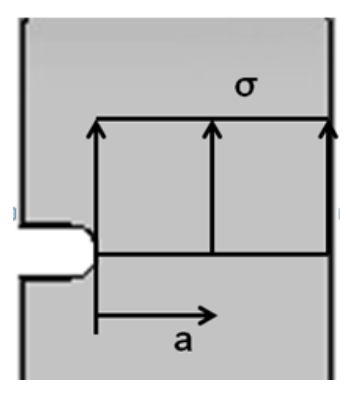


Figure 15: Definition of $\boldsymbol{\sigma}$ and a in the test specimen.



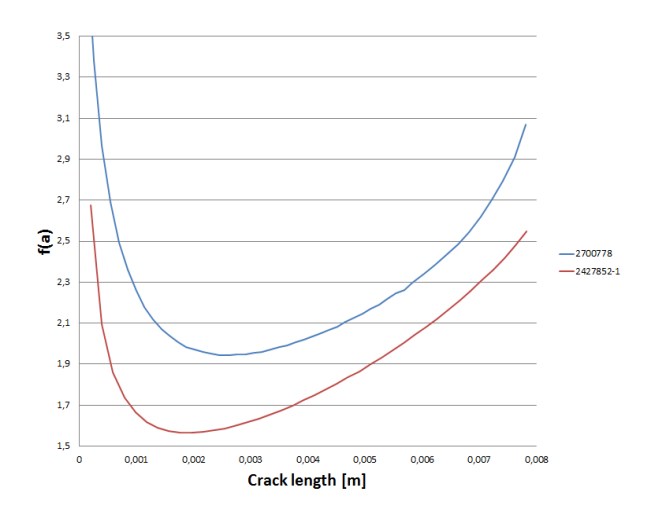


Figure 16: f(a) for different specimens. The blue line (2700778) is for the SEN specimen in Figure 3

2.4.4 Evaluation tool

A Matlab code was developed to evaluate the data. The evaluation is done in three steps as described below. The crack length vs cycles raw data contains considerable noise and must therefore be filtered before da/dN can be evaluated. The filtering process is described by a flowchart, see Figure 17. The data filtering process is semi-automatic, in the sense that it requires the test engineer to set the value of the "smoothing parameter" a_{tol} and check that the resulting filtered data is in good agreement with the raw data. If necessary, the evaluation is re-run with a manually adjusted value of a_{tol} . For tests run using the same test set-up, the noise level is similar and consequently only small adjustments of a_{tol} are required from test to test. For the present testing a_{tol} was typically in the range of 0.01-0.05mm.

1. Part0 - Characterization of thermal strain error

- 1a. Characterize the systematic error in thermal strain¹ calculated by the testing software, for the specific specimen and temperature cycle.
- 1b. Fit two piecewise polynomial functions describing the error vs temperature during heating and cooling respectively.
- 1c. Plot functions and raw data to ensure a reasonable fit and save the functions as two piecewise polynomial structures.

2. Part1 – Evaluation of crack length vs cycles

- 2a. Correct the thermal strain, based on input from "Part0", in order to obtain the correct mechanical strain.
- 2b. Identify characteristic points of each cycle; e.g. start, end, max stress and min stress.
- 2c. Evaluate the stiffness in each cycle and calculate the crack length based on a calibration curve and the un-cracked stiffness of the specific specimen.
- 2d. Plot and save the results.

KME

26

¹ In the MTS testing software, the thermal strain as a function of temperature is described by a single polynomial function fitted to a thermal cycle at zero load. In practice, the thermal strain during heating differs from the thermal strain during cooling. The use of a single polynomial function, that represents both heating and cooling, results in a systematic error in thermal strain.

3. Part2 - Evaluation of da/dN vs ΔK

- 3a. Read data output from Part1.
- 3b. Filter the crack length vs cycles data and evaluate *da/dN* vs cycles. The filtering algorithm is described in Figure 17.
- 3c. Calculate fracture mechanics parameters (ΔK , ΔK_{ASTM} , ΔJ).
- 3d. Plot to ensure reasonable data filtering and save the results.

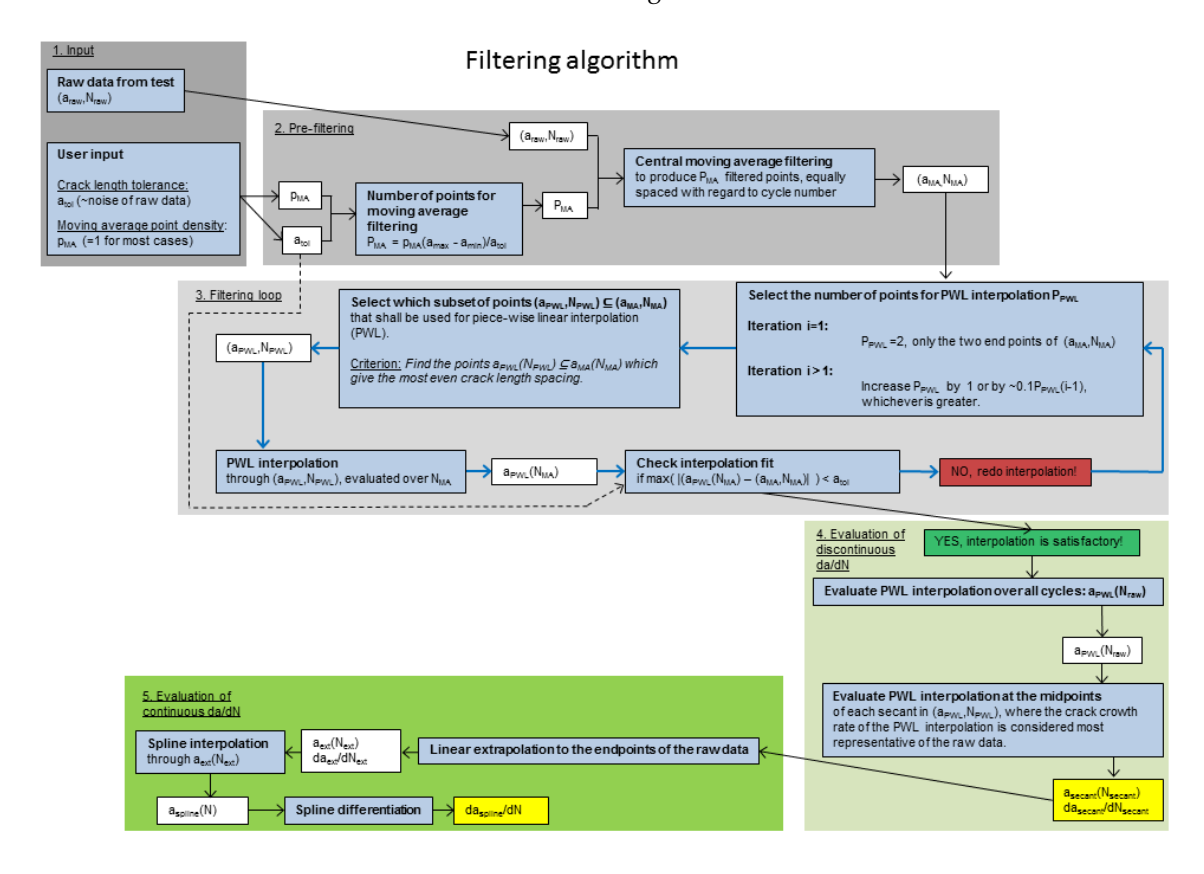


Figure 17 - Algorithm used to filter the raw crack length vs cycles data.

2.5 CRACK DRIVING FORCE PARAMETER

In order to enable comparisons between all the different types of test results generated, it was decided to use the effective stress intensity factor range ΔK_{ASTM} , according to the equation below, as crack driving force parameter for the evaluation of all tests. Thus, the results are presented as plots of da/dN vs ΔK_{ASTM} .

$$\Delta K_{ASTM} = K_{\text{max}} - (K_{\text{min}})_{+}$$
$$(K_{\text{min}})_{+} = \left[\text{Re}(\sqrt{K_{\text{min}}}) \right]^{2}$$

The crack length used to evaluate K_{max} and K_{min} is the average crack length along the crack front, as measured by the compliance method. It is possible to evaluate ΔK_{ASTM} even for crystallographic cracks which are non-perpendicular to the loading direction. However, the physical basis for such evaluation is questionable and therefore the data for



crystallographic cracks has been plotted as dashed lines. ΔK_{ASTM} was evaluated based on the K-solution for mode I cracks, using the apparent average crack length as measured either by the compliance method or by the potential drop method calibrated for mode I cracks. Finding a suitable description of the driving force for crystallographic crack growth is a complex task, which will not be further discussed here (treated within an ongoing PhD project).

2.5.1 Crack opening force

 ΔK_{ASTM} may be regarded as the effective ΔK under the assumption that the crack opening force is either zero or equal to the minimum force of the cycle, whichever is greater. For the isothermal tests performed, it is not possible to evaluate the actual crack opening force since the strain was not measured in these tests. For the TMF crack growth tests it may be possible to evaluate the actual crack opening force, but a suitable evaluation method is yet to be developed.

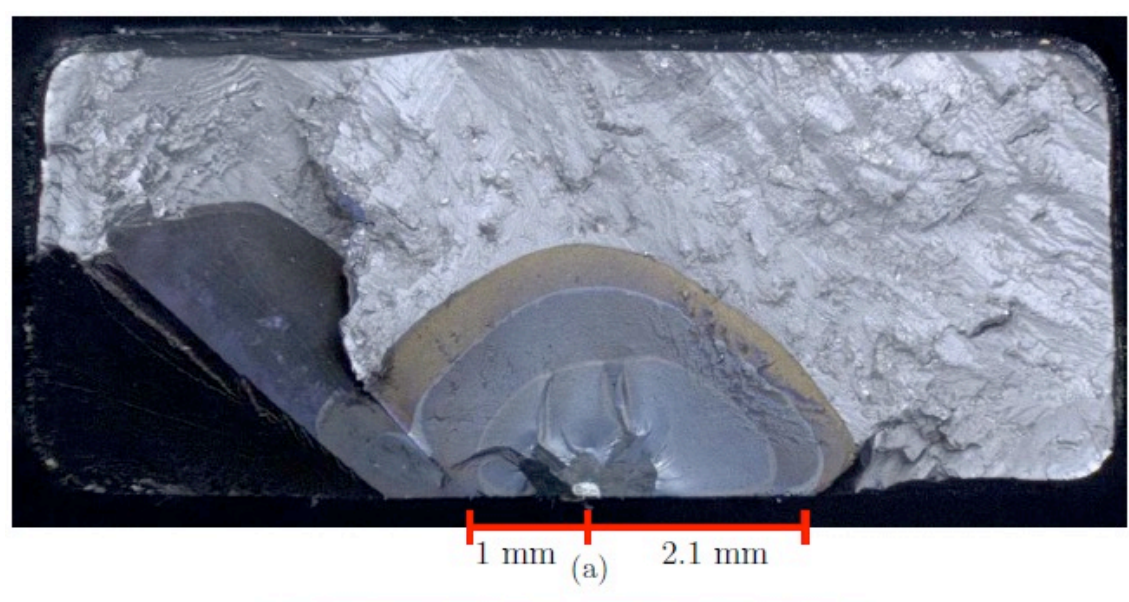
2.6 MICRUSTRUCTURAL INVESTIGATIONS

After testing, specimens were examined in stereo microscope and scanning electron microscope (SEM). Both fracture surfaces and polished cross-sections were examined in the SEM (Hitachi SU70 FEG-SEM for cross-sections and JEOL JSM-6610LV for fracture surfaces). In all micrographs of polished cross-sections, the loading axis is aligned in the vertical direction. For the purpose of determining the crystallographic orientation of the DCT and Kb specimens, the specimens were polished and etched with Kalling's #1 (5g CuCl2, 100ml HCl, 100ml ethanol) in order to reveal the dendrite structure.

2.6.1 Fracture surfaces

After finishing the testing, the fracture surfaces were examined in an optical microscope to determine the crack lengths when the cracking mode switches from Stage II to Stage I crack growth, as initially a Stage II crack is present in every specimen. From the fracture surfaces it could be observed that each crack has continued to grow a distance as a Stage II crack after the precrack until transitioning to a Stage I crack, except in the Kb2 and Kb3 specimens where the cracks transitioned directly after the precracking stage. Examples of these transition crack length measurements can be seen in Figure 18. The transition crack lengths were measured from the center of the EDM notch for the Kb specimens and for the DCT specimens at the plane surfaces, see Figure 18. It should be noted, that these measurements are from the optical microscopy examinations and not from DCPD measurements. This procedure was done for all Kb and DCT specimens and the results are summarised in Table 1, where the plane on which Stage I crack growth occurred first is marked with an asterisk. It should be noted, that some Stage I crack growth is visible even for cracks shorter than the transition crack length. This is neglected, since the crack switches back to Stage II crack growth until the transition crack length is reached. Additionally, it can be seen in Figure 18 that the Stage II crack surfaces are tortuous which in reality might be Stage I growth on two conjugate slip planes on a microscopic level [18]. However, a higher magnification Scanning Electron Microscope (SEM) image, see Figure 19, indicates that the crack has grown between the γ' -particles and thus, considering the context of this work, which is from an engineering point of view, the cracking mode which is perpendicular to the loading direction is macroscopically regarded as a Stage II crack.





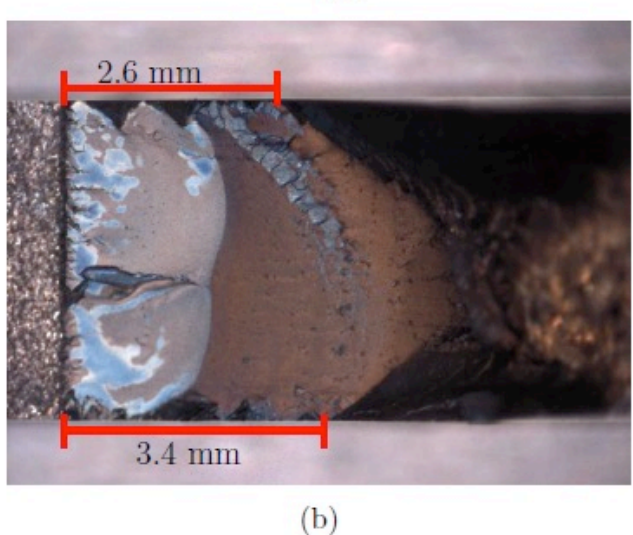


Figure 18: Measurements of the transition crack lengths on the fracture surface of the (a) Kb4 and the (b) DCT1 specimen.

Table 1: Crystallographic cracking planes and the maximum K_I value along the crack front at the first transition of the crack.

Specimen	Kb1	Kb2	Kb3	Kb4	DCT1	DCT2	DCT3	DCT4
Left cracking plane	111*	111*	111*	111*	111	111	111*	no Stage I cracking
Transition crack length left [mm]		0.1225(direct)	0.1225(direct)	1	3.4	3.5	2.4	no Stage I cracking
Right cracking plane	111	111	111	111	111*	111*	111	no Stage I cracking
Transition crack length right [mm]	1	0.85	0.9	2.1	2.6	3.1	3.6	no Stage I cracking
Max. K_I at transition crack length [MPa \sqrt{m}]	19.5	9.13	5.9	15.6	33.1	37.8	22.2	no Stage I cracking

*first active crystallographic slip plane



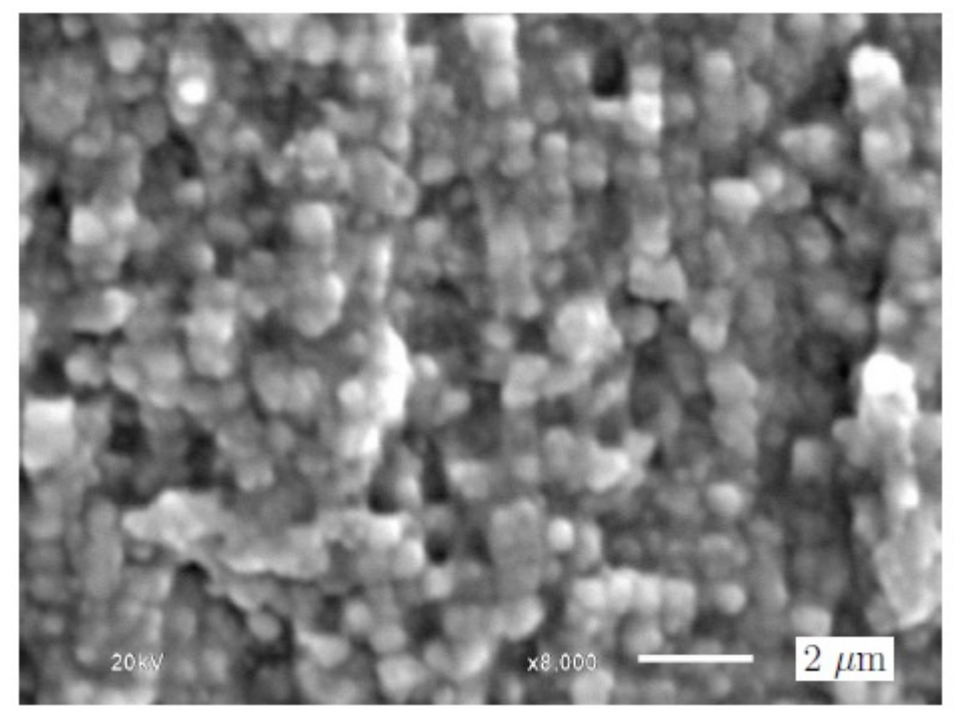


Figure 19: SEM image of the Stage II fracture surface of the specimen DCT1 at a length of approximately 2 mm from the notch in the center of the specimen.

For the Kb specimens, the shape of the growing crack can be seen due to heat tinting during the testing, cf. Figure 18a, and can be approximated to be semi-circular. No heat tinting was done in the testing of the DCT specimens and therefore semi-elliptical crack front shapes with a shallow depth have been assumed. The fracture surfaces of the specimens were also scanned in an Atos Triple Scan machine to acquire a 3D representation of the fracture surfaces in terms of mesh data. These were imported to an FE-preprocessor, where planes with the corresponding normals to the {111}-planes were added for visualisation. This is a convenient procedure to identify the crystallographic plane on which the Stage I crack grew.

In Figure 20 the scanned fracture surface of the Kb1 and DCT1 specimens are depicted, where the EDM notches and the two obtained Stage I cracking planes are highlighted. This was done for all Kb and DCT specimens and the results are summarised in Table 1, which also shows the maximum K_I values along the crack front at the transition crack length in order to establish a comparison between the specimens. From this evaluation it could be seen that the DCT4 specimen does not show any Stage I cracking. The scanned fracture surface of DCT4 is shown in Figure 21a, containing the visualised (1 -1 -1)-plane, which intersects the fracture surface exactly parallel to the crack growth direction. Figure 21b illustrates this schematically in order to visualise the location of the (1 -1 -1)-plane in relation to the Stage II cracking plane.



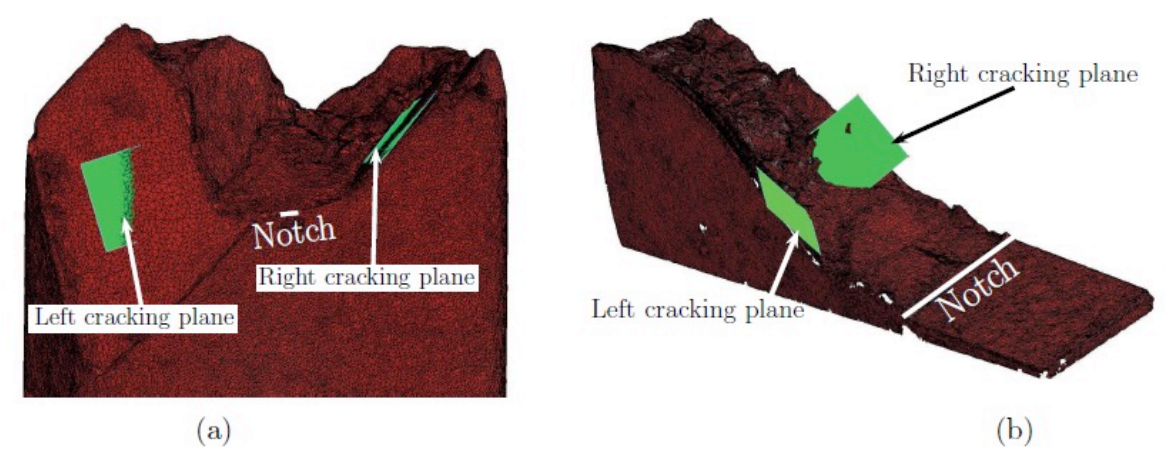


Figure 20: The scanned fracture surface of (a) Kb1 and (b) DCT1 with visualized Stage I cracking planes.

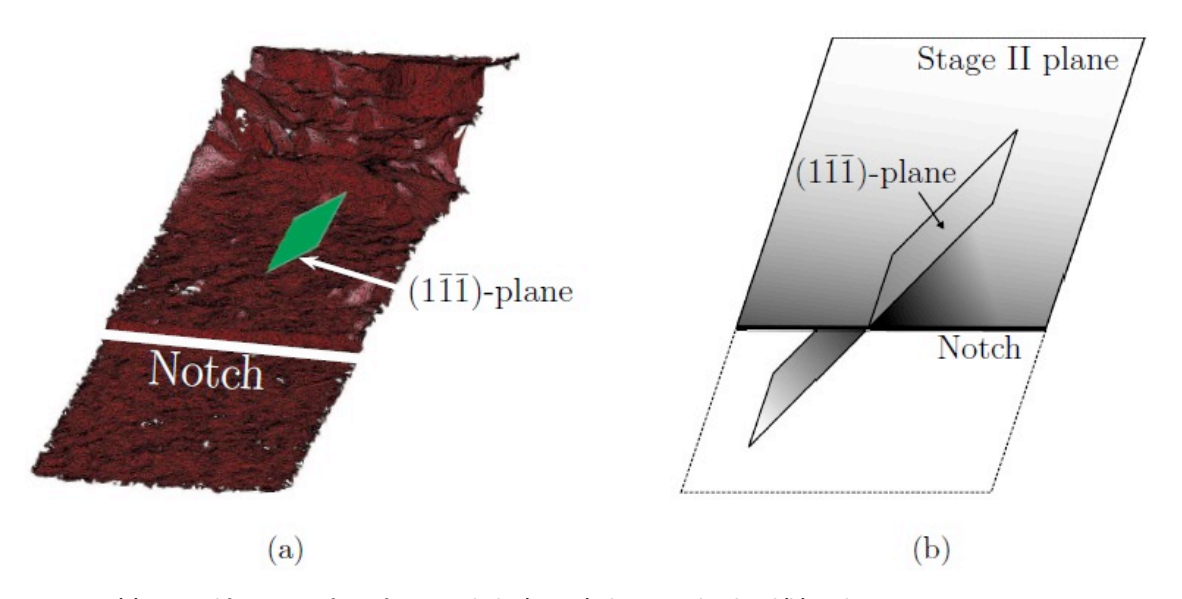


Figure 21: (a) Scanned fracture surface of DCT4 with the (1 - 1 - 1)-plane visualized and (b) a schematic representation of the intersection of the Stage II cracking plane with the (1 - 1 - 1)-plane.

2.6.2 Crystallographic orientation and misalignments

The importance of the crystallographic orientation and misalignments has been pointed out earlier. On each specimen, three orthogonal faces were polished and etched. The dendrites visible on these surfaces represent the projection of the crystallographic lattice vectors in vertical and horizontal direction; cf. Figure 22a where some are highlighted. The angles between each visible dendrite projection and the vertical and horizontal axis of each surface relative to the global coordinate system were measured. This is schematically shown in Figure 22b in terms of a cube representing the three orthogonal faces, where the angles $\zeta_{-1,2,3}$ and $\eta_{-1,2,3}$ are quantified.



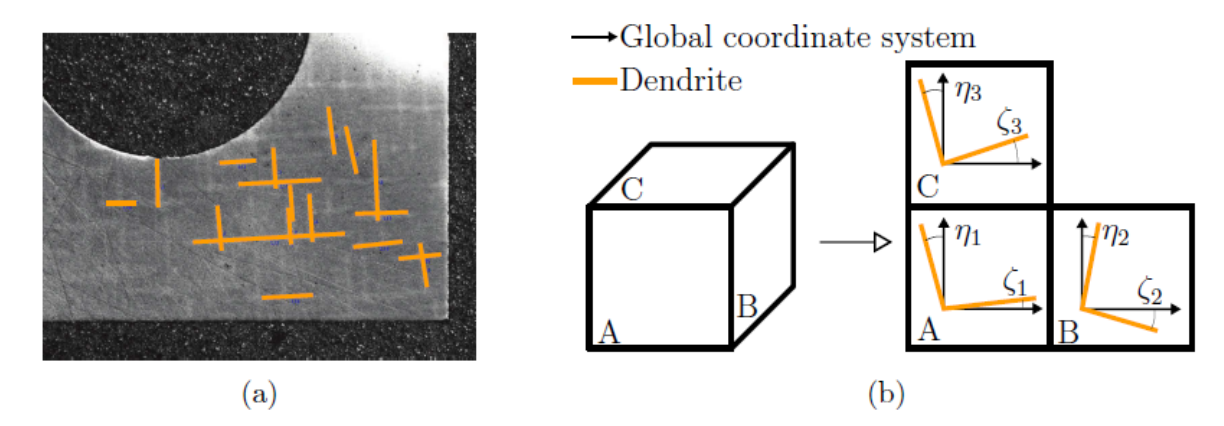


Figure 22: Depiction of the dendrites on one side of (a) the DCT1 specimen and (b) the studied surfaces for the measurement of the crystallographic orientation on the specimens.

These measurements of the dendrites contain a scatter, due to measurement inaccuracies and inhomogeneous crystallographic structures. In other words, not all measured angles for the visible dendrites are equal for the respective surface. This scatter was accounted for by calculating the mean value and its standard deviation in a 95% confidence interval. This means that for each surface in Figure 22b a vertically and horizontally mean angle and associated confidence interval was quantified, hence six angles for all surfaces were generated. It is to be noted that these angles are not intermutually orthogonal in this case. Based on this, an optimisation procedure was carried out to ensure intermutual orthogonality between the angles, to define the crystallographic orientations in the specimens to be used in the FE-context. Thus, a Matlab [19] script was written, which iteratively uses all possible permutations of the six generated angles above (mean, maximum and minimum for the six angles, 3⁶ = 729) as input. The objective here was to minimise the Root-Mean Square Errors (RMSE) of the input angles relative to the calculated crystallographic lattice vectors. This was done to account for the scatter of the measurement data in the modelling work and to calculate error ranges. Note, that the 95% confidence interval is valid for the measured angles of the dendrites and not for the calculated crystallographic orientations. The optimised crystallographic orientations are shown in Table 2, in terms of the sequential rotations about the global coordinate axes. Furthermore, the RMSEs for the optimised crystallographic orientations are shown, in order to quantify the error between the generated angles of the dendrites on the surfaces and the obtained crystallographic orientations in the optimisation routine. An RMSE value of zero indicates that there is no error, meaning that the generated angles of the dendrites on the surfaces and the crystallographic orientations coincide. The higher the RMSE value the higher the error between them.

Table 2: Optimised mean crystallographic orientation accounting for the misalignment in terms of sequential rotation about the global x-, y- and z-axis and the RMSEs.

Specimen	Kb1	Kb2	Kb3	Kb4	DCT1	DCT2	DCT3	DCT4
Rotation about x-axis [°]	1.7	-0.7	-1.4	6.3	-4.7	-3.7	-6.4	-2.0
Rotation about y-axis [°]	0.1	0.1	-2.3	-4.9	0.2	-3.6	-0.14	-3.2
Rotation about z-axis [°]	-2.8	-5.5	-5.8	-7.7	-5.4	-2.7	-19.9	-46.4
RMSE [°]	0.94	0.69	0.64	1.24	0.94	0.47	2.31	2.41



2.7 MODELLING

2.7.1 Finite element context

To analyse the crack growth behaviour, or more precisely, to model the actual crack growth in a finite element (FE) context, a crack propagation software is needed in conjunction with the adopted FE-solver. In this project, the FE-solver Abaqus [20] is paired with the crack propagation tool FRANC3D [21]. This enables computations for arbitrary geometries, materials and load cases. The crack propagation software is used to automatically grow a crack through the FE-model based on the stress intensity factors along the crack front by the use of the M-integral. In order to be computationally more efficient, FRANC3D divides the FE-model into a local and a global domain, where only the local domain is remeshed in each crack growth step to meet the current crack front shape, and where the global domain retains its initial mesh, see Figure 23. A schematic overview of the procedure is shown in Figure 24. For a more detailed description of the procedure, please see e.g. [22].

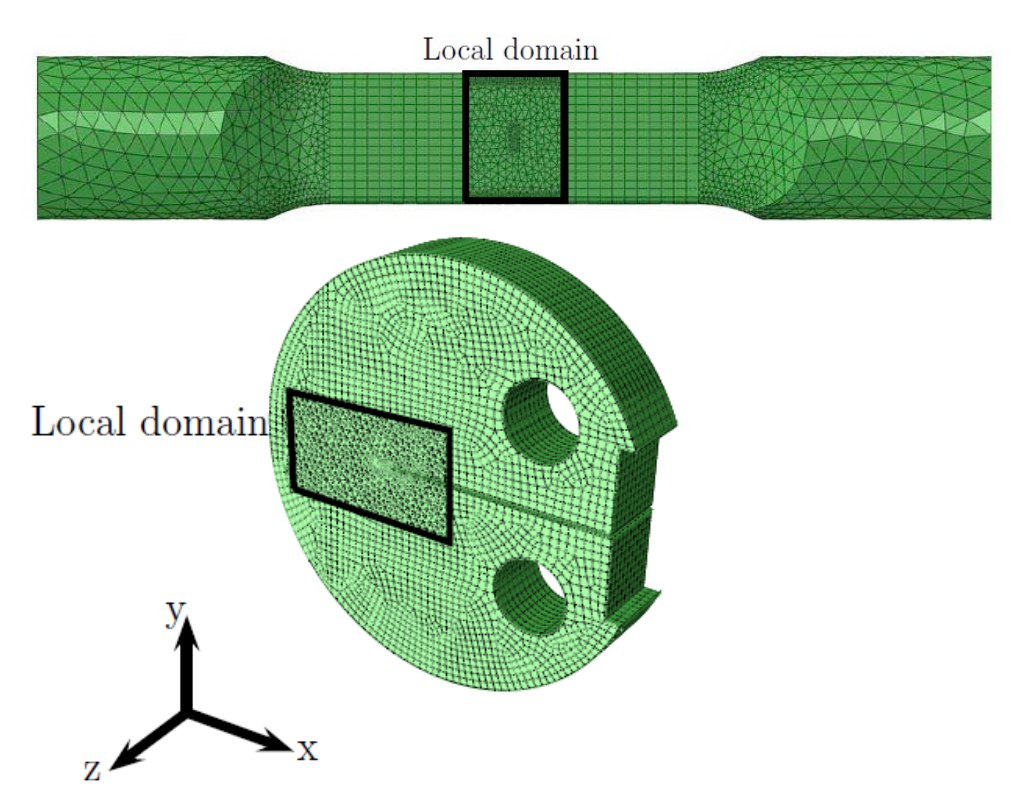


Figure 23: FE-models of two specimens, where the respective local domain is highlighted.



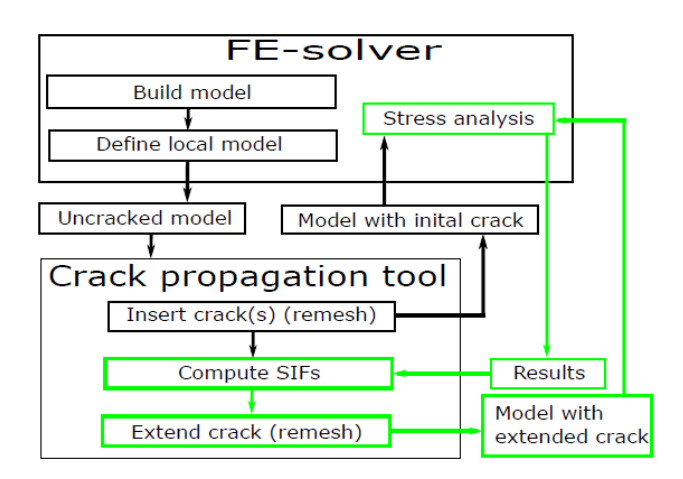


Figure 24: Figure 2. Workflow of the crack propagation procedure.

2.7.2 Crack growth anisotropy

The anisotropy present in single-crystal nickel-base superalloy materials bring many difficulties in terms of modelling, evaluation and prediction of fatigue crack growth. The influence of the crystal orientation, as well as the influence of misalignments of the crystal orientation due to the casting process have been investigated in [23]. It was shown that both the crystal orientation and the misalignment from the ideal crystal orientation are important for the crack driving force. The realistic (industry praxis) maximum limit of 10° misalignment was considered. It could be observed from the results that the crack growth behaviour is highly influenced by the misalignment. This knowledge is of great interest for the academia and the gas turbine industry in order to evaluate the crack growth in single-crystal components more accurately.

2.7.3 Crystallographic crack driving force

As discussed and displayed above, cracks in single-crystal nickel-base superalloys tend to grow on crystallographic {111} slip planes. Since the crack path can deviate substantially from conventional Mode I cracks, the traditional approach of computing the stress intensity factors on the crystallographic planes is not suitable and, hence, a new crack driving force parameter needs to be introduced. The relation between crack propagation rate and stress intensity factor range in Paris' law is usually based on the conventional Mode I stress intensity factor K_I. This holds for most cases where the crack grows orthogonal to the maximum tensile stress, i.e. in most cases considering isotropic materials. In anisotropic materials like single-crystal nickel-base superalloys this is not necessarily valid, especially for crystallographic cracking. Thus, an appropriate crack driving force parameter is needed in order to predict cyclic crack growth in these materials in a similar fashion to Paris' law. Most research suggests that shear stress intensity factors (as in Ku and Ku) resolved onto a crystallographic plane are suitable candidates [17],[24],[25],[26]. This is motivated by the assumption that crystallographic cracking is coupled to the dislocation motion based on shearing, which is predominantly localised to the crystallographic slip planes.

The above presented M-integral can be used to compute the stress intensity factors in an anisotropic material. The anisotropic stress intensity factors are adopted to calculate the



stress field around the crack tip using the definitions for anisotropic materials developed by Hoenig [27], according to:

$$\begin{cases} \sigma_{xx} \\ \sigma_{yy} \\ \sigma_{yz} \\ \sigma_{xz} \\ \sigma_{xy} \end{cases} = \frac{1}{\sqrt{2\pi r}} \begin{cases} Re\left(\sum_{i=1}^{3} \frac{\mu_{i}^{2}N_{ij}^{-1}K_{j}}{Q_{i}}\right) \\ Re\left(\sum_{i=1}^{3} \frac{N_{ij}^{-1}K_{j}}{Q_{i}}\right) \\ -Re\left(\sum_{i=1}^{3} \frac{\lambda_{i}N_{ij}^{-1}K_{j}}{Q_{i}}\right) \\ Re\left(\sum_{i=1}^{3} \frac{\mu_{i}\lambda_{i}N_{ij}^{-1}K_{j}}{Q_{i}}\right) \\ -Re\left(\sum_{i=1}^{3} \frac{\mu_{i}\lambda_{i}N_{ij}^{-1}K_{j}}{Q_{i}}\right) \\ -Re\left(\sum_{i=1}^{3} \frac{\mu_{i}N_{ij}^{-1}K_{j}}{Q_{i}}\right) \end{cases} = \frac{1}{\sqrt{2\pi r}} \begin{cases} f_{xx}\left(K_{I}, K_{II}, K_{III}, \theta\right) \\ f_{yy}\left(K_{I}, K_{II}, K_{III}, \theta\right) \\ f_{xz}\left(K_{I}, K_{II}, K_{III}, \theta\right) \\ f_{xy}\left(K_{I}, K_{II}, K_{III}, \theta\right) \end{cases}$$

$$\begin{split} \sigma_{zz} &= -\frac{\left(S_{31}\sigma_{xx} + S_{32}\sigma_{yy} + S_{34}\sigma_{yz} + S_{35}\sigma_{zx} + S_{36}\sigma_{xy}\right)}{S_{33}} \\ &= \frac{1}{\sqrt{2\pi r}} f_{zz} \left(K_{I}, K_{II}, K_{III}, \theta\right), \end{split}$$

It can by further rearrangement be seen, by using the projected stress state on the slip plane in the respective slip directions of interest, and multiplying with $\sqrt{2\pi r}$ and taking $\lim r \to 0$, that the resolved stress intensity factors (RSIFs) are defined accordingly:

$$k_{II} = n \cdot f'(K_{I}, K_{II}, K_{III}, \gamma, \beta) \cdot n$$

$$k_{II} = s \cdot f'(K_{I}, K_{II}, K_{III}, \gamma, \beta) \cdot n$$

$$k_{III} = t \cdot f'(K_{I}, K_{II}, K_{III}, \gamma, \beta) \cdot n$$

where n is the unit normal of the crystallographic slip plane, s is the evaluation direction vector, and t= s_n. Note that the resolved stress intensity factor parameters are denoted by a lower case k in order to distinguish it from the conventional parameter K. The parameters k_I, k_{II} and k_{III} correspond to the three modes of fracture resolved on a crystallographic slip plane, which can also be an arbitrary plane, in the given evaluation directions, cf. Figure 3. A discussion about appropriate evaluation directions is given in [28]. Based on the findings and previous research, one reasonable choice is to use the slip directions on the four crystallographic slip planes. An equivalent crack driving force parameter k_{EQ}, accounting for resolved normal as well as resolved shear stresses, was formulated and is based on the idea that the resolved shear stresses weaken the crystallographic plane by dislocation motion and that the resolved normal stress separates the surfaces [26]:

$$k_{EQ}(n,s) = \sqrt{\psi_I k_I^2 + \psi_{II} k_{II}^2 + \psi_{III} k_{III}^2},$$

where ψ_i , i = 1;2;3, are calibration parameters that can be fitted based on experiments.

The equivalent resolved stress intensity factor for each specimen was evaluated by use of two different approaches, Model 1 and Model 2.



Model 1

This model is physically inspired by the micromechanisms occurring on the crystallographic level. The deformations in these materials are localised to the crystallographic slip planes in specific directions, which are associated to the dislocation motion [29]. As the dislocation moves, the superpartial (101) will split up into two Shockley partials and their edge components (121), generating stresses in the primary and secondary crystallographic slip direction [30]. Furthermore, the normal stress to the crystallographic plane makes it easier or harder for slip to occur, and in turn for the crack to grow. In this model, the evaluation direction s corresponds to the primary crystallographic slip directions, i.e. Burgers' vectors b; cf. Table 6, where all slip systems α , with the corresponding slip plane normal n^{α} and slip direction b^{α} are defined. For all three slip directions per plane also the negative direction vector is evaluated and the maximum value is chosen, i.e. $k_{EQ}(s = b) = max\{k_{EQ}(b), k_{EQ}(-b)\}$. This is due to the assumption that the sign of the physical slip direction is of no importance. Furthermore, it can be said that in this physically inspired model; ku corresponds to the primary, ku to the secondary slip direction which is orthogonal to s and n, and k1 acts in the normal direction, which facilitates separation of the crack surfaces. An example for the slip direction is shown in Figure 25, where the three slip directions on the (111)crystallographic slip plane are illustrated. It should be noted that the depicted coordinate system is the local crack front coordinate system, and not the material coordinate system in which the slip plane normal direction and slip directions are defined.

Table 3: Definition of the slip systems α with corresponding slip plane normal n^{α} and direction b^{α} .

α	n^{lpha}	b^{lpha}
1	(111)	$[01\bar{1}]$
2	(111)	$[\bar{1}01]$
3	(111)	$[1\bar{1}0]$
4	$(1\bar{1}\bar{1})$	$[0\bar{1}1]$
5	$(1\bar{1}\bar{1})$	$[\bar{1}0\bar{1}]$
6	$(1\bar{1}\bar{1})$	[110]
7	$(\bar{1}1\bar{1})$	[011]
8	$(\bar{1}1\bar{1})$	$[10\bar{1}]$
9	$(\bar{1}1\bar{1})$	$[\bar{1}\bar{1}0]$
10	$(\bar{1}\bar{1}1)$	$[0\overline{1}\overline{1}]$
11	$(\bar{1}\bar{1}1)$	[101]
12	$(\bar{1}\bar{1}1)$	$[\bar{1}10]$



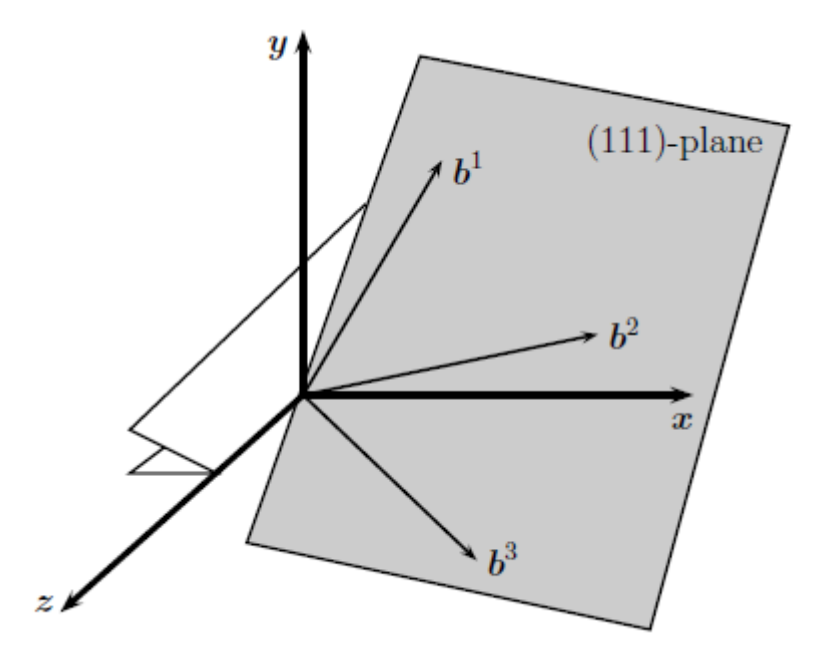


Figure 25: Figure 10: Evaluation directions for Model 1. Slip directions on the (111)-plane.

Model 2

In this model all possible evaluation directions s on the crystallographic slip planes are considered and the direction with the corresponding maximum k_{EQ} is extracted. It is assumed that the resistance for transition to crystallographic crack growth is isotropic in the sense that it is not a function of the evaluation direction s. This means, that the model considers the direction in which the shear and normal stresses are maximum (k_{II} , k_{II} and k_{III}), and is not coupled to the physical micromechanisms of the single-crystal material in question. Thus, the slip plane which results in the highest k_{EQ} value will be deemed to be the Stage I cracking plane. Therefore, k_{EQ} is computed for all possible directions s and the maximum is selected. It should be noted that all directions on the crystallographic plane are evaluated, i.e. in 360° about n in steps of 1°, illustrated in Figure 26. Thus, $k_{EQ} = \max(k_{EQ}(s))$, $\forall s$ on n, where the plane normal vector n of the corresponding crystallographic slip plane.



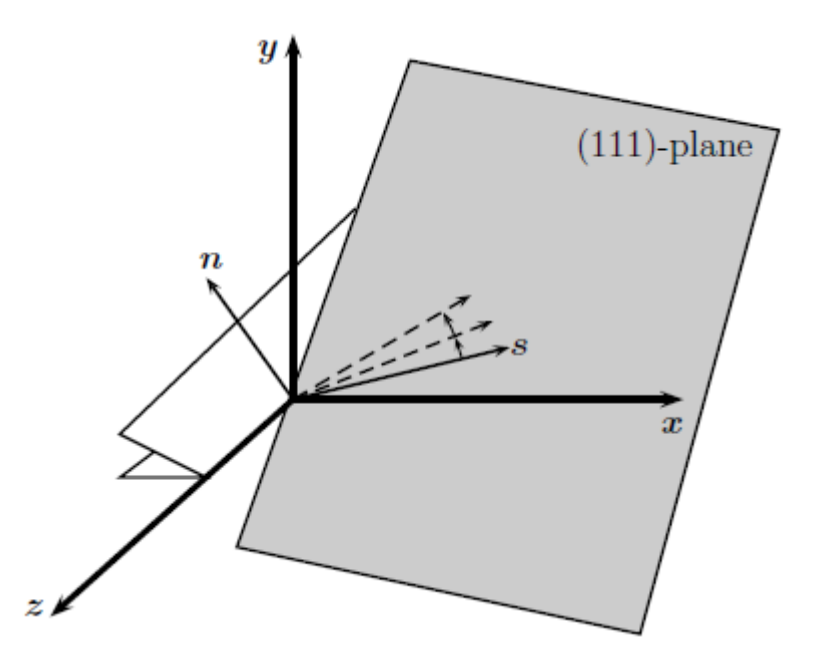


Figure 26: Figure 11: Evaluation directions on the (111)-plane for Model 2.

For anisotropic materials, as the investigated type of material is in this project, anisotropic SIFs are calculated along the crack front. These SIFs are then post-processed in order to calculate the resolved stress intensity factors k_I , k_{II} , k_{III} and k_{EQ} .

2.7.4 Handling inelasticity

In many applications, it is important to handle inelastic deformations that arises at stress concentrations like notches, which can influence subsequent crack growth in the material by residual stresses. However, the approach used in FRANC3D, to evaluate the stress intensity factors by the M-Integral, is restricted to linear-elasticity.

A method of handling residual stresses caused by inelastic deformations in a linear elastic crack growth context is presented in Fel! Hittar inte referenskälla. In brief, the residual stress field, obtained during unloading at the end of the first load cycles with a stable hysteresis of an uncracked FE-model in an elasto-plastic simulation, is superimposed to the linear elastic crack evaluation simulation of the corresponding cracked FE-model, see Figure 27. This enables the possibility to account for inelastic deformations when using the M-Integral to calculate the stress intensity factors. This approach is motivated by the assumption that after the initial shakedown no further inelastic deformations are accumulated. An appropriate material model has to be chosen in order to capture the correct inelastic behaviour, e.g. such as the one described in Leidermark et al. [31]. The above described method was utilized in Fel! Hittar inte referenskälla., with a perfect plastic material description, in order to handle the Mintegral context, see Figure 28. It should be noted, that the study in question was done based on the material IN718 in polycrystalline form, but the methodology is expected to be applicable to any type of material using an appropriate material description, i.e. also single-crystals nickel-base superalloys.



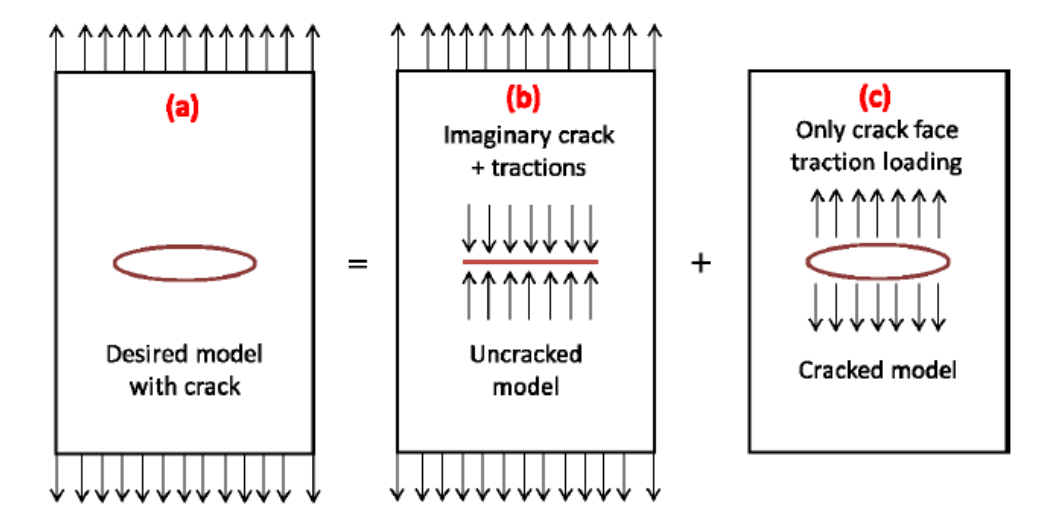


Figure 27: Figure 3: Superposition for crack face traction.

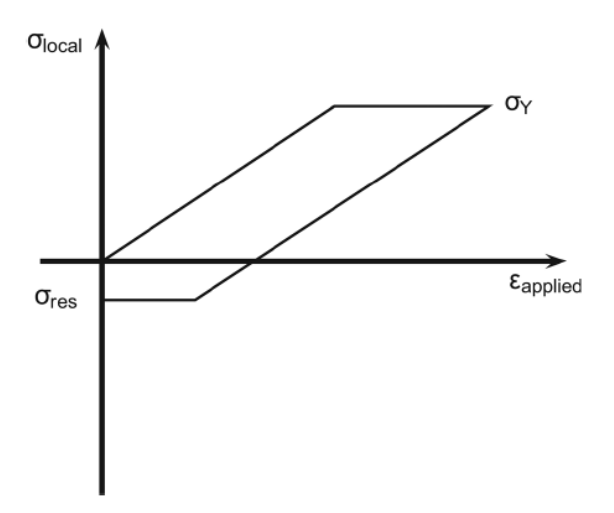


Figure 28: Figure 4. Schematic view of the stress-strain response in a stress-raising feature.

2.8 COMPONENT-NEAR DEMONSTRATOR

Cyclic fatigue testing is to be conducted on specimens closely resembling a turbine blade root at elevated temperature. The crack propagation behaviour will be studied with the aim to derive data "half way" to reality compared to standard lab fatigue testing.

Initial testing will be conducted to learn how to perform the testing. Initially it is planned to run tests at 500°C. Tests will be run for a limited number of cycles after which the testing will be stopped for inspection of test specimens using NDT. If cracks are found in the specimen their size will be quantified. The test sample will then be put back in the test rig for continued testing. This process will be repeated until blade off, see Figure 29. Based on experience derived here the final test plan will be set up.

After finished testing each test sample will undergo an extensive metallographic analysis to determine damage mechanisms, cycles to crack initiation, crack propagation characteristics etc.



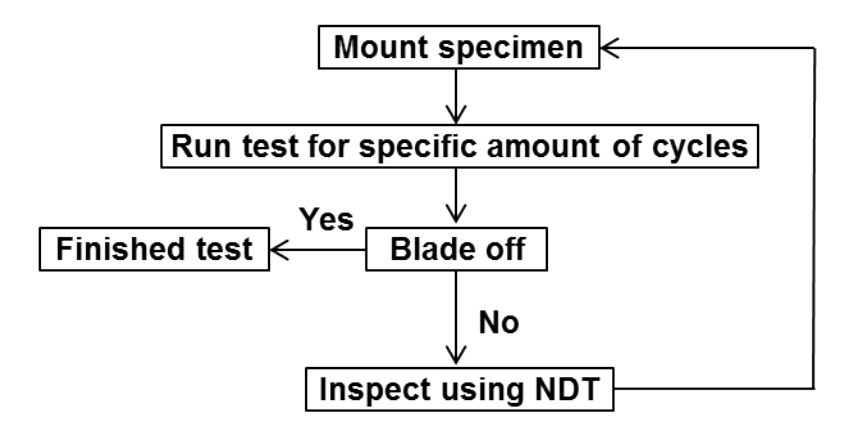


Figure 29. Test flow chart

2.8.1 Test setup

Extensive work has been performed in order to derive design the test setup, see 6. A number of finite element models were created to evaluate different concepts of the test setup. For an example of one of the evaluated models, see Figure 30. The models were evaluated with the intention of deriving the test setup best representing the loading conditions in a real blade root. All simulations were performed at a temperature of 500°C, see Figure 31 for an example of the root flank pressure distribution.

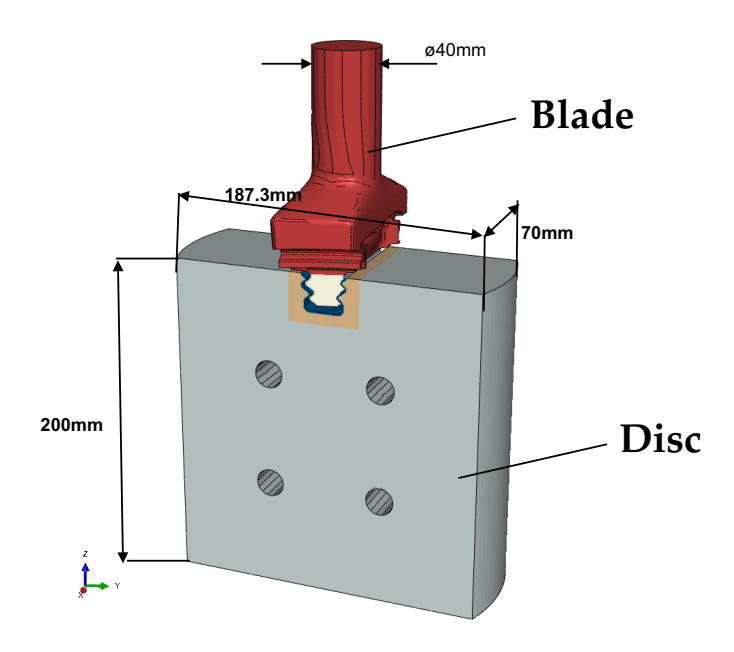


Figure 30: Example of FE model.



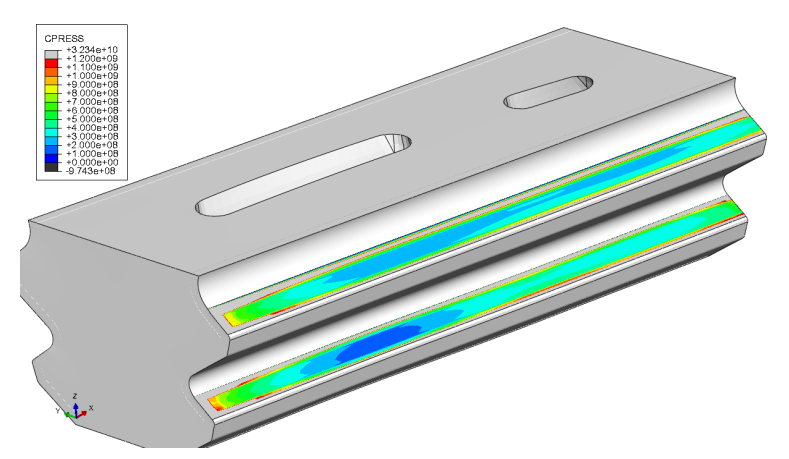


Figure 31: Contact pressure, pressure side.

Non-linear simulation has been done with to evaluate the cyclic life of the blade attachment. The cyclic life of the blade attachment grooves in the disc has been calculated using a strain-life method in which a kinematic plastic material model has been used.

As a result of this investigation the blade like test specimen seen in Figure 32 was derived.

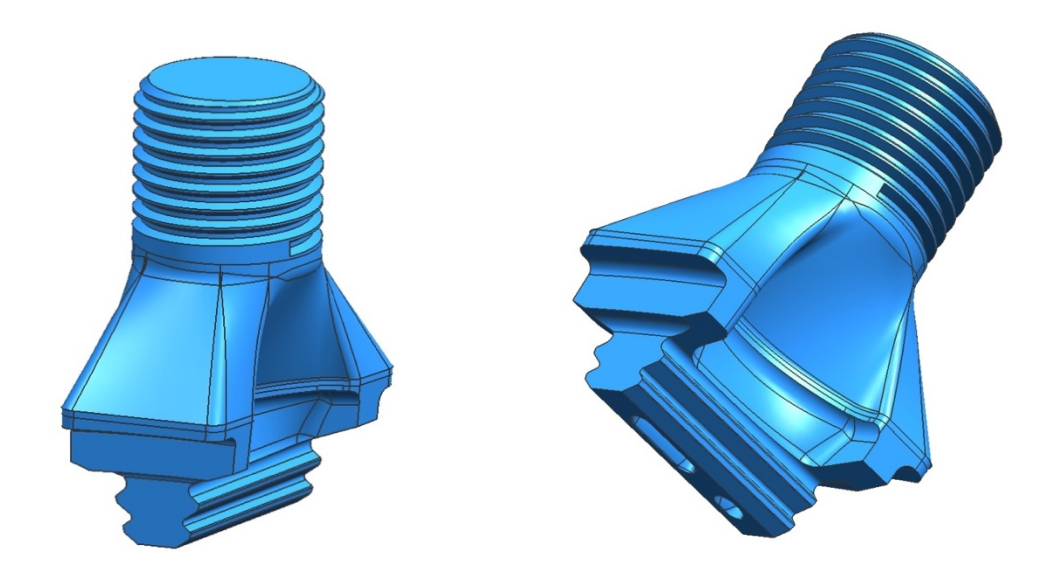


Figure 32: Derived blade specimen geometry.

Furthermore, based on these requirements the test rig seen in Figure 33 was decided to rebuild to handle this testing series. Parts were purchased from Instron according to the drawing in Figure 34.





Figure 33. LCF machine for component testing.

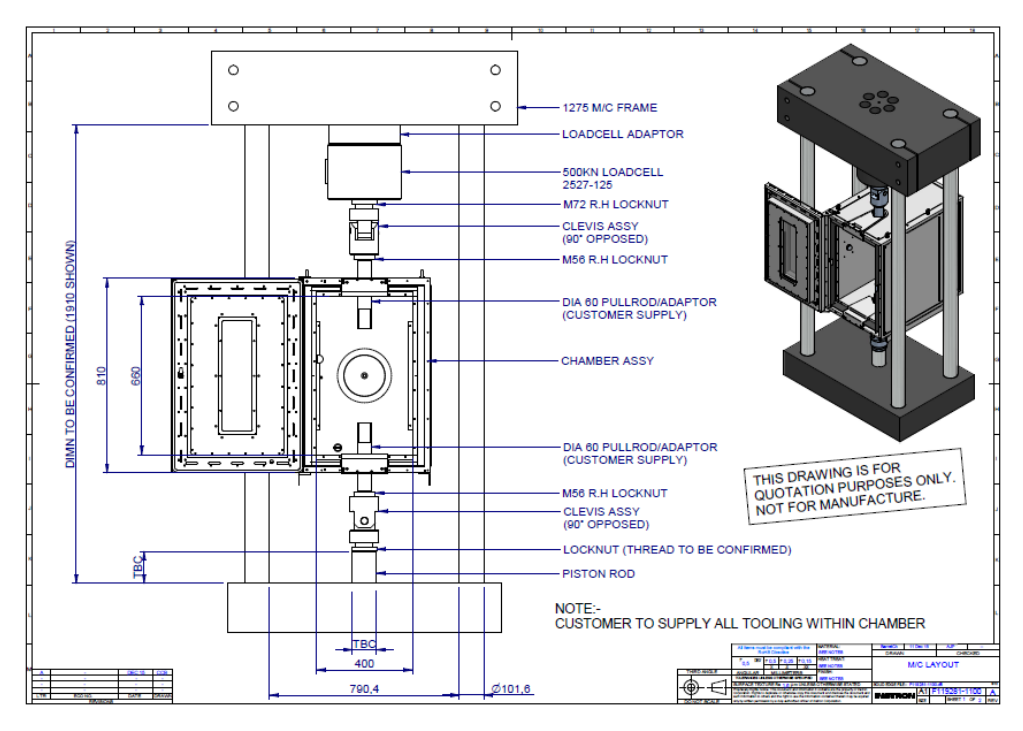


Figure 34. Instron machine upgrade.

The test machine is not yet fully assembled and thus, up until the date of writing this report, no tests have been performed.



3 Results and analyses

3.1 ISO THERMAL RESULTS AND ANALYSES – DCT SPECIMEN

3.1.1 DCT results at 20°C

Fracture appearance

In the 20°C tests, non-crystallographic cracking was dominant. Figure 35 shows the fracture surfaces of <001> specimens, tested at various force ranges. Small secondary crystallographic cracks are in some cases found at the surface of the specimens, where the stress state is close to plane stress. This is most clearly observed in the specimens tested at lower force range, see Figure 35 a and b. At intermediate force range, the fracture surface is rougher, but no large crystallographic crack facets are observed, see Figure 35 c. At the highest force ranges crystallographic secondary cracks can be found in the interior of the specimen, see Figure 35 d and e.

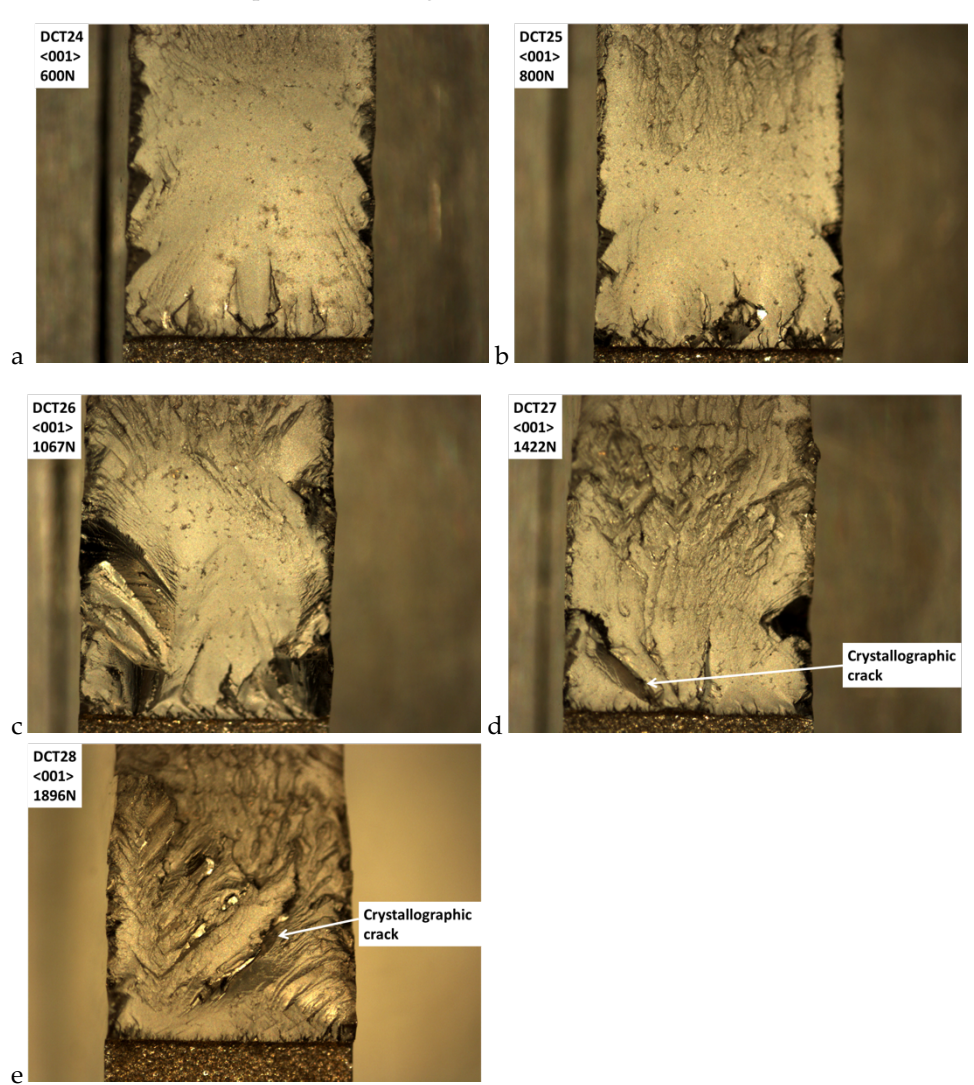


Figure 35 - Fracture surfaces of DCT specimens tested at various force ranges at room temperature. a: DCT24, 600N, b: DCT25, 800N, c: DCT26, 1067N, d: DCT27, 1422N, e: DCT28, 1896N. The EDM notch is in the bottom of each image and the crack has grown upwards.



The non-crystallographic cracks tend to propagate preferentially between the γ' particles, only rarely propagating through γ' particles, see Figure 36. The non-crystallographic cracks were studied at high magnification in order to investigate if there was any crystallographic preference as to the local crack path on the micro scale. However, no such preference was observed. The non-crystallographic cracks did not follow the γ/γ' -interfaces exclusively but were sometimes observed to pass through the middle of the γ -channels, see Figure 37c. The crack advance mechanism for Mode I crack growth was proposed by Saxena and Antolovich [18] for CMSX-2 does not seem to be applicable to the testing reported in this work.

The crystallographic secondary cracks propagate through the particles since they are confined to a specific crystallographic plane, see Figure 37. In the <011> specimens, secondary crystallographic cracks form along the {111} planes. The secondary crystallographic cracks mainly form along the {111} planes which are nominally parallel to the loading direction, see Figure 38. This may be seen as indication that the crystallographic cracks are mainly driven by shear stress rather than normal stress. Deformation bands can be seen with an orientation corresponding to the intersection of {111} planes with the surface of the specimen, Figure 39, which indicates octahedral slip. No deformation bands corresponding to primary cube slip were observed.

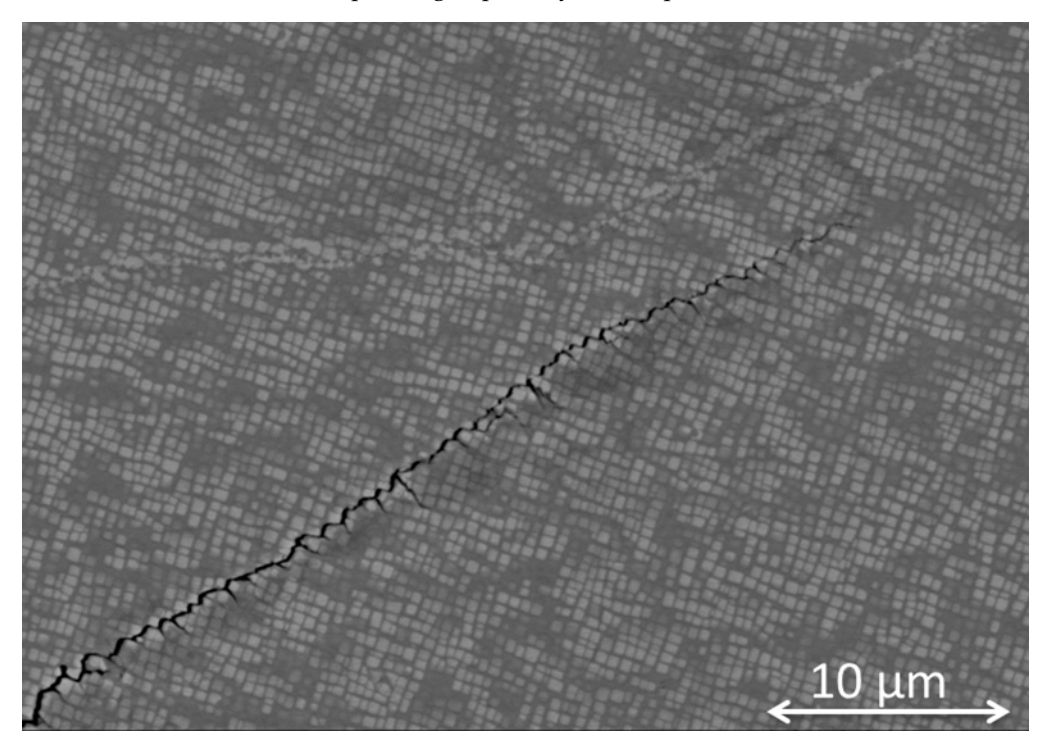


Figure 36 – Secondary crack in specimen DCT03. Notch orientation: <012>. The notch is oriented in the horizontal direction and the crack grows from left to right. The crack propagates preferentially between the primary y' particles rather than through them.



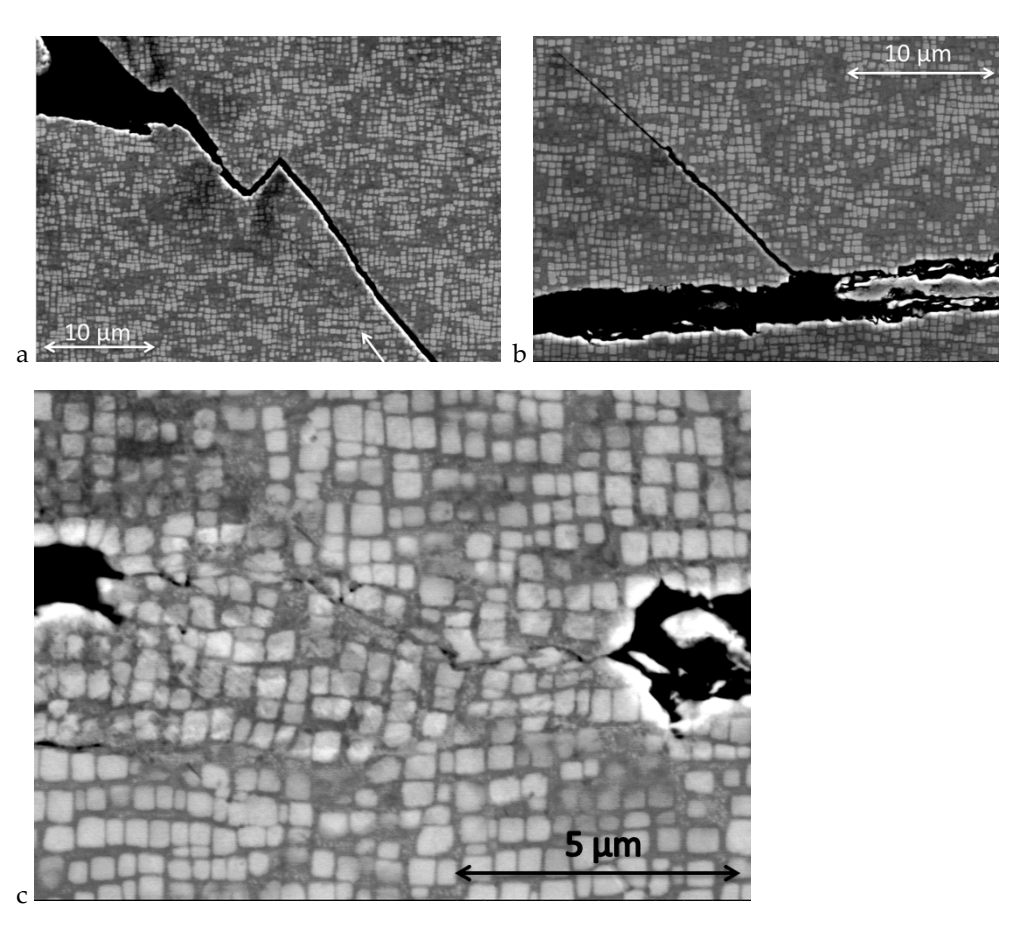


Figure 37 – Specimen DCT02. Notch orientation: <001>. The notch is oriented in the horizontal direction and the main crack grows from left to right. a: Crystallographic secondary crack and {111} deformation band close to the EDM notch marked by white arrow. b: Crystallographic secondary crack. c: Non-crystallographic crack propagating preferentially between the primary gamma prime particles.

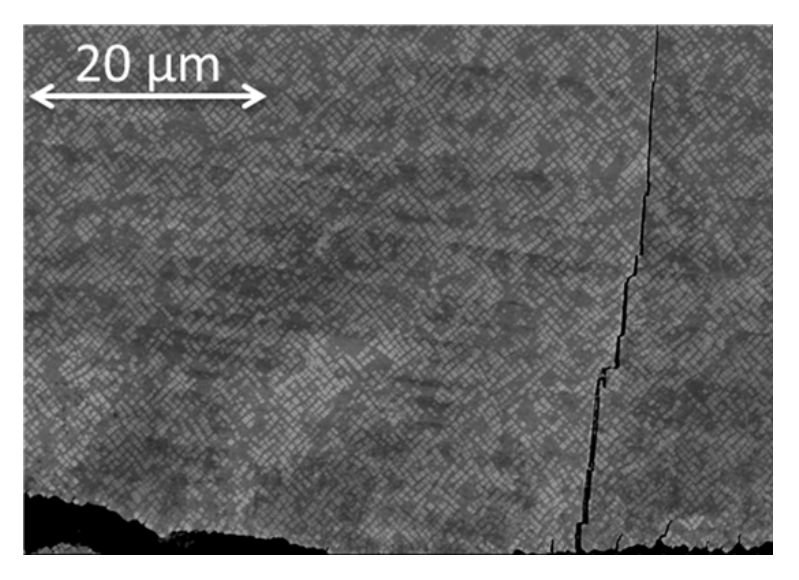


Figure 38 - SEM image of specimen DCT05. Notch orientation: <011>. Secondary crystallographic cracks form along the {111} planes. Deformation bands can be seen with an orientation corresponding to the intersection of {111} planes with the surface of the specimen.



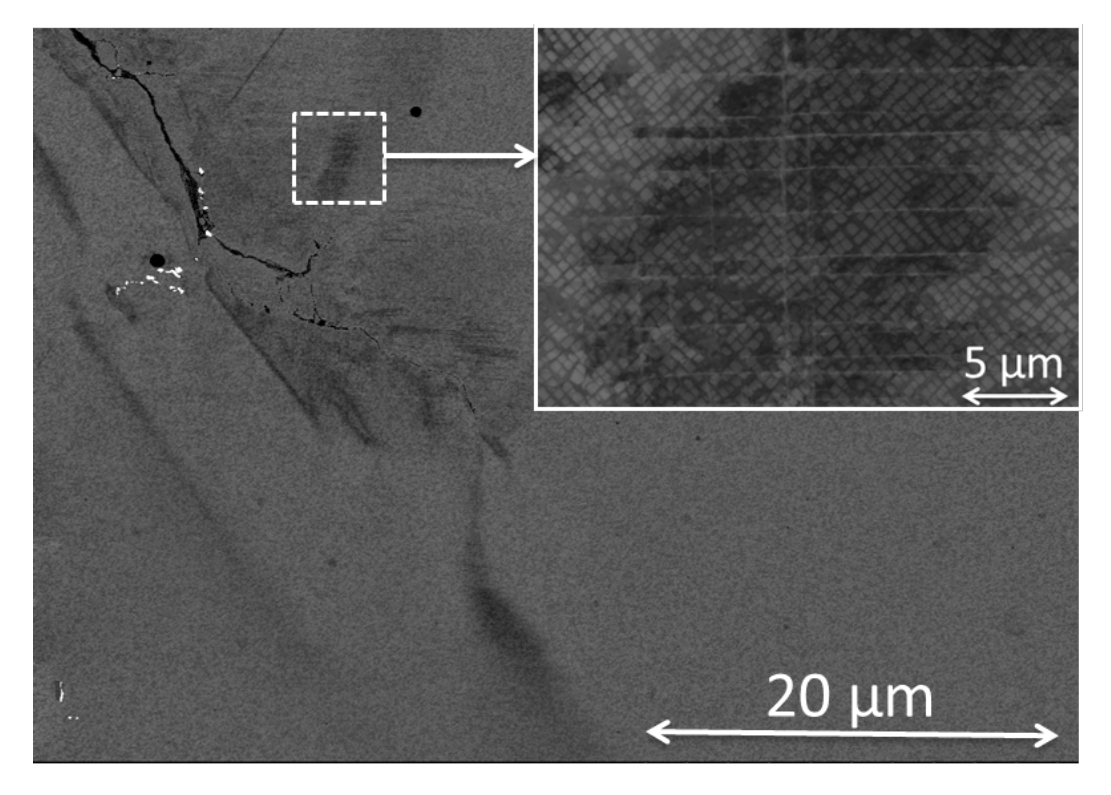


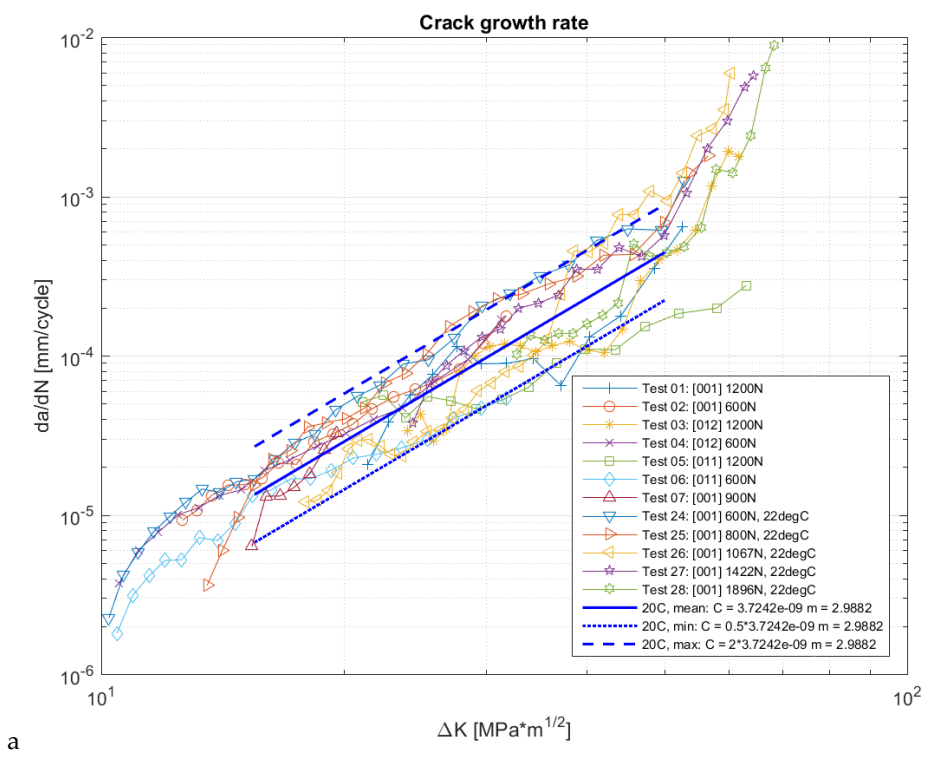
Figure 39 - SEM image of specimen DCT05, Notch orientation: <011>.

Crack growth rates

The crack growth rates at 20°C are plotted in Figure 40. Transient crack growth behaviour is observed at the beginning of the tests and at the end of the tests. The transient parts of the data were ignored for the purpose of curve-fitting. The scatter of da/dN vs ΔK within a certain test group was evaluated for the <001> specimens tested at 20°C. These are the testing conditions under which the largest number of specimens ha been tested. The scatter was evaluated graphically, by plotting da/dN vs deltaK. The upper and lower bounds of the scatter band were defined by applying suitable scaling factors to the average trendline.

It was found that the maximum crack growth rate could be described by a factor of 2 increase from the average trendline. Similarly the minimum crack growth rate could be described by a factor of 0.5 reduction of the average trendline (see Figure 40b). The same scatter band limits were found to cover the scatter seen in all test groups. It was also found that for each testing temperature the results for all tested orientations for the DCT-specimens could be bundled together and the scatter could still be covered by the same scatter band limits (see sections 3.1.1, 3.1.2 and 3.1.3).





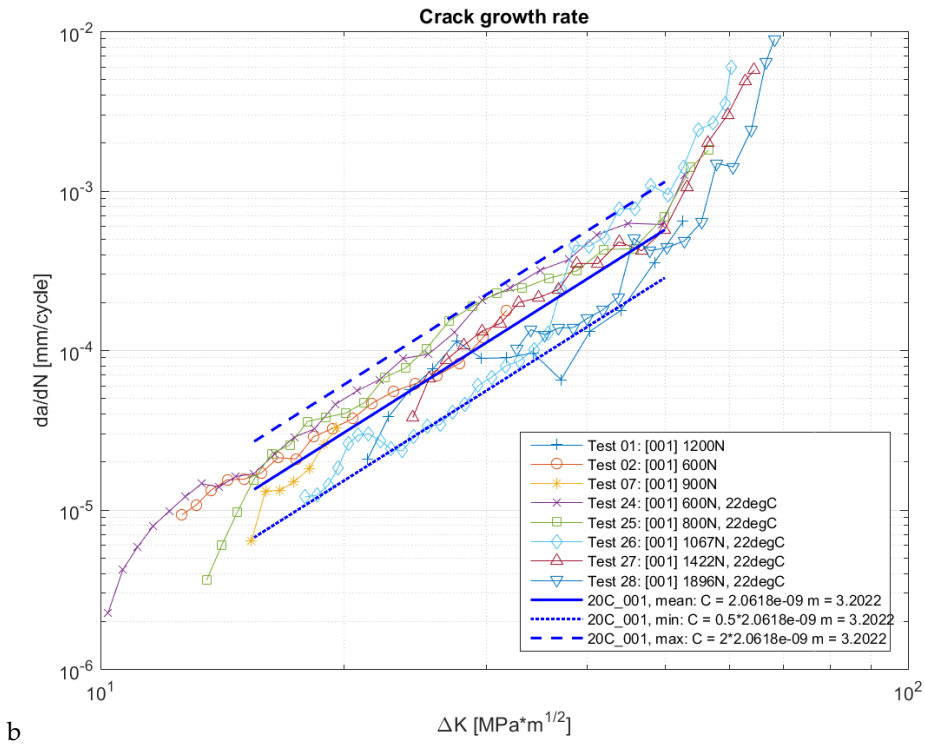


Figure 40 - da/dN vs ΔK at 20°C. a: All tests b: <001> tests.



3.1.2 DCT results at 500°C

Fracture appearance - Non-crystallographic crack growth

In the <011> tests at 500°C the crack growth was non-crystallographic throughout the entire tests, as can be seen in Figure 41c. In Figure 42 deformation bands can be seen with an orientation corresponding to the intersection of {111} planes with the surface of the specimen. This indicates octahedral slip.

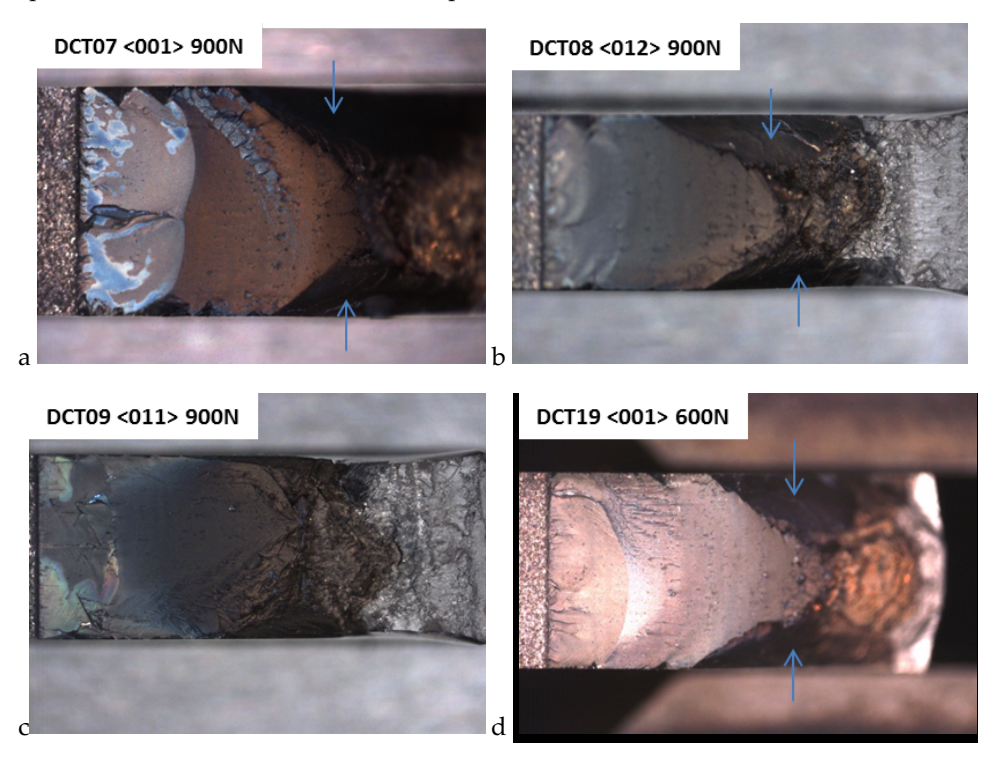


Figure 41 – Fracture surfaces of specimens tested at 500°C. Major crystallographic crack facets have been marked by arrows. a: DCT07, <001>, b: DCT08, <012>, c: DCT09, <011>, d: DCT19, <001>.

In the <001> and <012> tests, the crack growth was at first non-crystallographic, with small crystallographic crack facets only forming at the side surfaces of the specimens. These short crystallographic cracks are apparently non-sustainable, in the sense that they are outgrown by the non-crystallographic crack so that the non-crystallographic nature of the crack front is restored, see Figure 41 and Figure 43. For the purpose of crack growth rate evaluation, these short non-sustainable crystallographic cracks were neglected. Thus it was assumed that a suitable crack driving force parameter could be obtained from the *K* solution given in ASTM E399 without significant errors associated with the presence of short, non-sustainable crystallographic cracks. At low magnification, the non-crystallographic fracture surface appears flat (Figure 44a) but a higher magnification SEM image of the same area reveals a topography resulting from the avoidance of the primary gamma prime particles during non-crystallographic crack growth (Figure 44b).



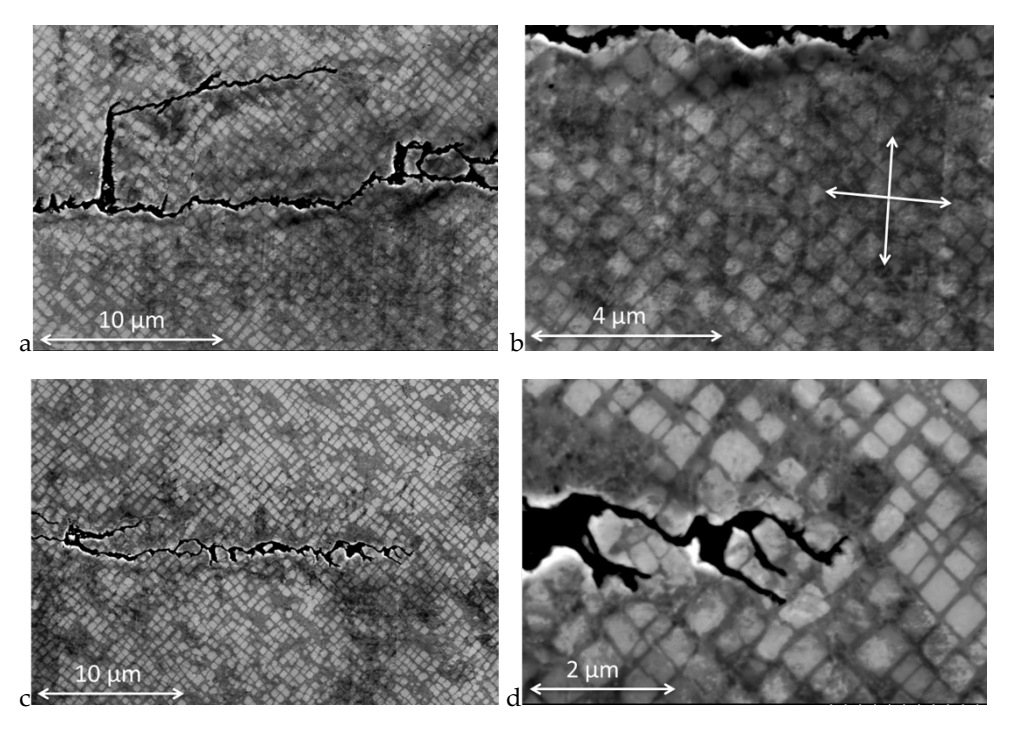


Figure 42 – DCT11, <011>, 500C. a: Deformation bands at an angle corresponding to the intersection of {111} planes with the surface of the specimen. b: Higher magnification image of the deformation bands from "a". The orientation of the deformation bands is shown by the white arrows c: Crack tip region. d: Higher magnification image of the crack tip.

Fracture appearance - Partly crystallographic crack growth

As the crack length increased in the <001> and <012> specimens, a point was reached where crystallographic cracks started to propagate into the specimen, so that the fraction of the crack which was crystallographic gradually increased, see Figure 43. These crystallographic cracks are sustainable, in the sense that they are not outgrown by the non-crystallographic crack, which means that the partly crystallographic nature of the crack front is sustained and even amplified as the crack grows. In all specimens there was a region in the middle of the crack front where the crack growth remained noncrystallographic throughout the entire test. Each crystallographic crack follows one of the {111} planes on a macroscopic level. However, the crystallographic crack growth occurs on several parallel planes, as can be seen in Figure 44c and d. Striation-like features can be seen in SEM images of the crystallographic fracture surfaces. These features will henceforth be referred to as "brittle striations". It should be emphasized that these brittle striations are not believed to be formed by the classical blunting/resharpening mechanism commonly referred to for ductile materials [32]. Both the apparent propagation direction and the distance between the brittle striations differ significantly between adjacent fracture planes, see Figure 44 d and e. On one of the planes, the striation distance is approximately 2µm and on an adjacent plane it is approximately 8µm. This corresponds to a crack growth rate of approximately 1-7µm per cycle in the global propagation direction at a crack length of 5.2mm. The crack growth rate evaluated from the PD measurement at this crack length was 1.4µm/cycle. It should be kept in mind that the crack growth rate evaluated from the PD measurement should be regarded as an average value across the entire crack front, which is partly crystallographic and partly non-crystallographic.



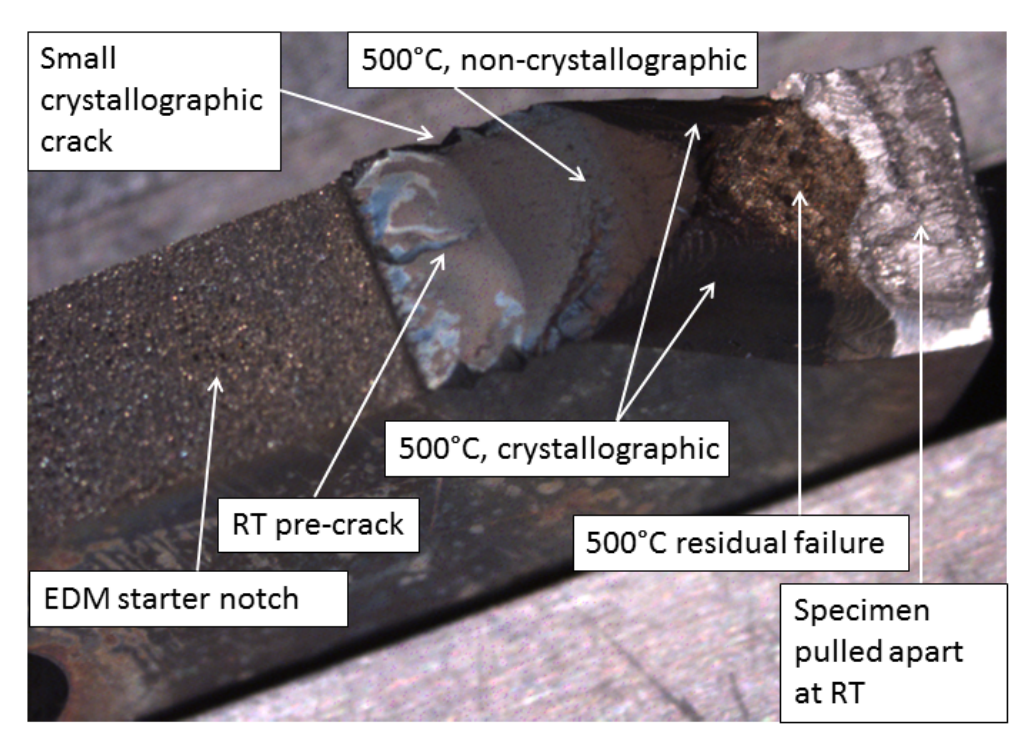


Figure 43 – Fracture surface overview for specimen DCT07, <001>, 500°C.



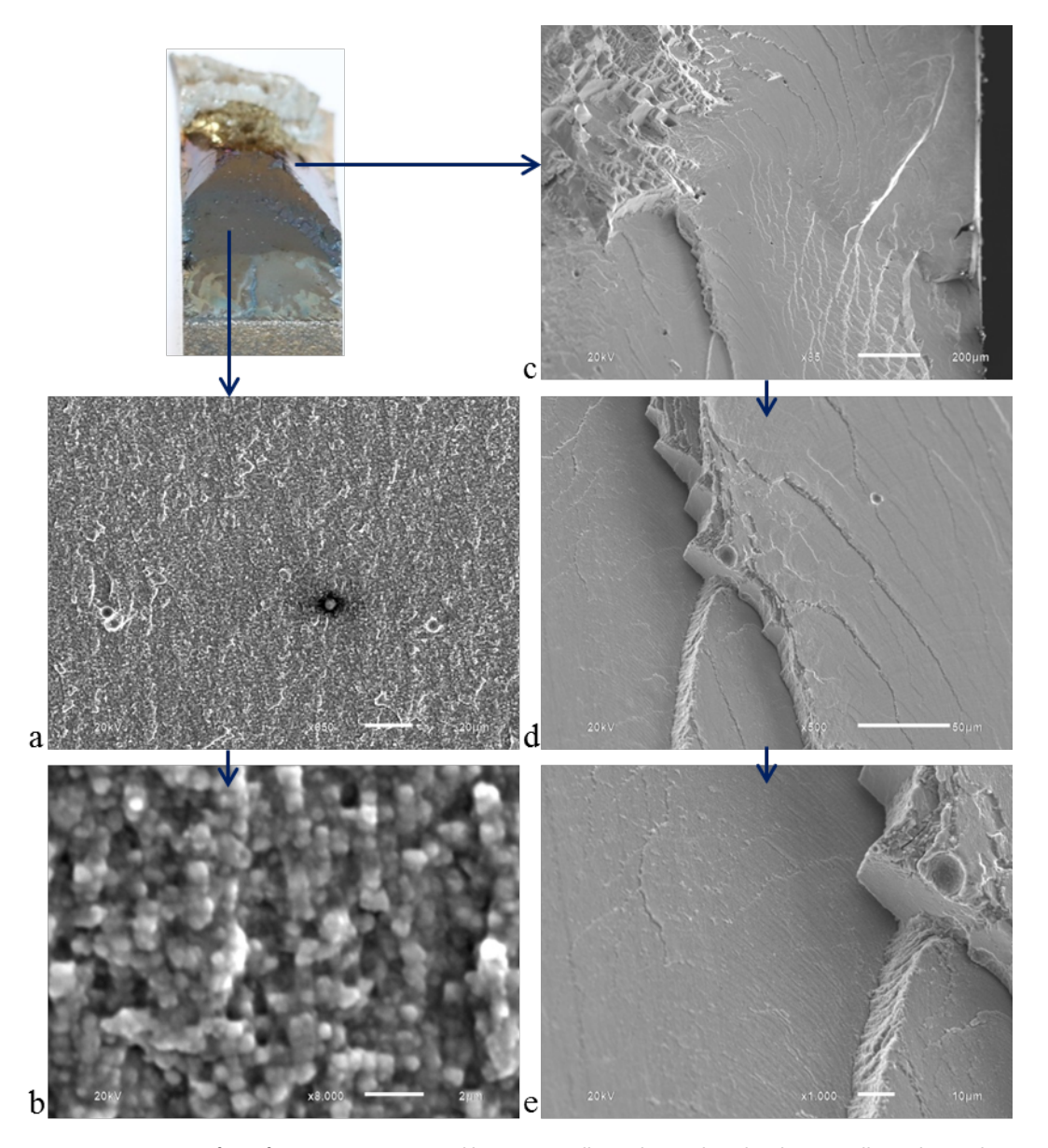


Figure 44 - Fracture surface of specimen DCT07. a and b: Non-crystallographic crack. c, d and e: Crystallographic crack.

Crack growth rates

At 500°C, tests were performed with three different notch orientations: <001>, <012> and <011>. The crack growth rate vs ΔK is plotted in Figure 45. It should be noted that crystallographic crack growth occurred in some of the tests. The crack growth rates of partly crystallographic cracks have been plotted using dashed lines, in order to indicate that the plotted stress intensity factor range ΔK is based on a K solution which is not valid for partly crystallographic cracks. The distinction between non-crystallographic and partly crystallographic crack growth was clarified in the previous subsections. It is noteworthy that the crack growth rates of partly crystallographic cracks fall within the scatter of the results for non-crystallographic cracks. As discussed in section 2.5, the physical basis for the evaluation of da/dN vs ΔK for partly crystallographic cracks is questionable.



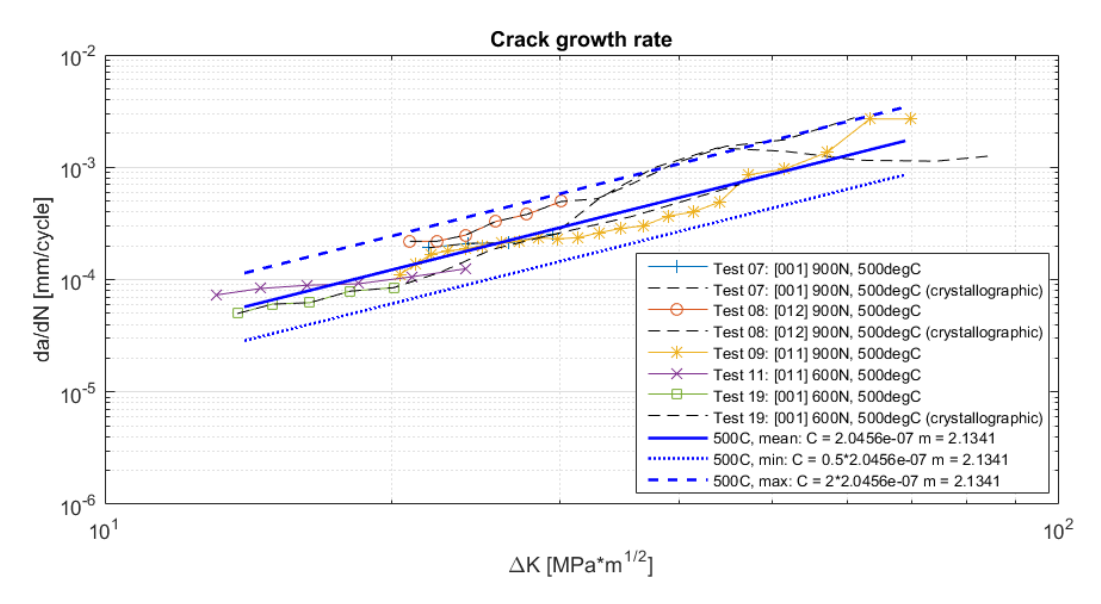


Figure 45 - da/dN vs ΔK for all tests at 500°C.

3.1.3 DCT results at 750°C

Fracture appearance

At 750°C, tests were performed with two different notch orientations: <001> and <012>. For orientation <001>, tests were run both with 30s hold time and with 1h hold time. The hold time tests were performed as block tests, where the hold time at maximum load was varied in testing blocks of 30s, 1h or 24h hold time. The block testing is further described in section 3.1.7. The crack growth was non-crystallographic in both cases. Both sides of the specimens were observed and the appearance of the crack was similar on both sides. Crack branching was observed, especially when a dwell time of 1h at maximum load was applied, see Figure 46 and Figure 47a, but also to some extent with 30s hold time, see Figure 46. The oxidation of the crack made it difficult to determine the exact crack path. In some cases recrystallization occurred in the γ' depleted zone beneath the oxide, see Figure 47c. At the final crack tip, there is no oxidation ahead of the crack but there are voids or micro-cracks ahead of the crack, see Figure 47d. There are pores in the material which originate from the casting process. At all tested temperatures, cracks are at times observed to pass through such pores. It appears that pores in the vicinity of the crack tip may influence the path of the crack, see Figure 47a. In the tests at 750°C, cracks have also initiated at pores ahead of the crack tip, see Figure 47b.

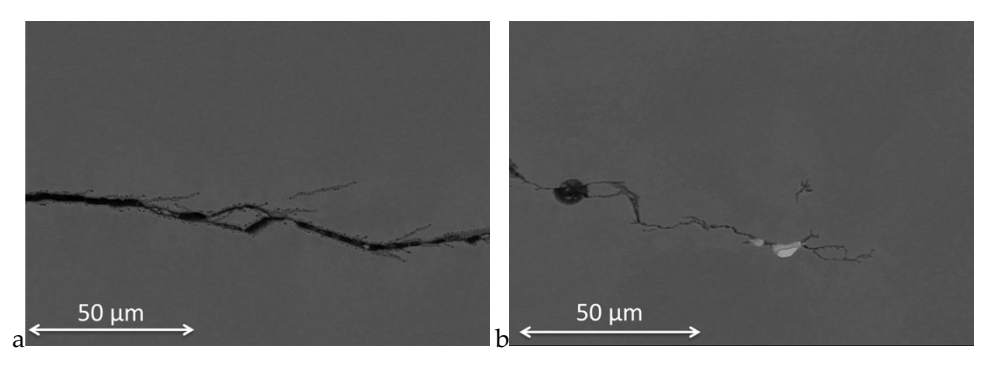


Figure 46 – DCT17, <001>, 30s dwell. a: Some crack branching is observed, but the crack stays macroscopically in mode I. b: Final crack tip.



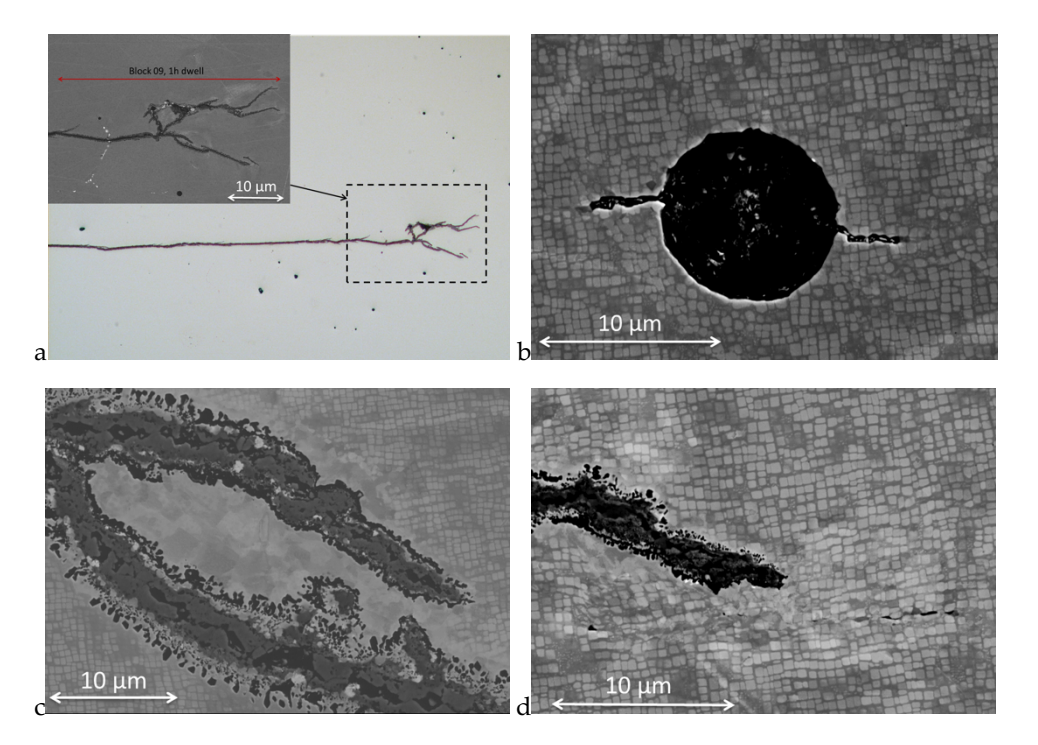


Figure 47 - DCT18, <001>, 1h dwell. a: Overview of the crack, showing the crack length interval of the last 1h dwell block based on the PD measurement. b: Casting pore ahead of the crack tip, from which cracks have initiated. c: Oxide has formed in the crack and the γ' depleted zone has recrystallized. d: Final crack tip. Voids or micro-cracks can be seen ahead of the crack tip.

Crack growth rates

The crack growth rates at 750°C are plotted in Figure 48. Tests were performed with two different notch orientations: <001> and <012>. For orientation <001> tests were run both with 30s hold time and with 1h hold time. The crack growth rate per cycle is increased when the hold time is increased from 30s to 1h. The crack growth rates for all tests at 750°C fall within the scatter band obtained by shifting the average trendline a factor of 2 for the upper bound and a factor of 0.5 for the lower bound. Note that for specimen #20 the test conditions were changed during the test and that each test condition is represented separately in the graphs, see section 3.1.7 for more details.

For the tests with 1h hold time a simple additive crack growth model was used where a Paris-like equation was used also for the time-dependent crack growth:

$$\frac{da}{dN} = C\Delta K^{m} + \int_{0}^{t_{dwell}} AK_{dwell}^{n} dt \approx C\Delta K^{m} + t_{dwell} AK_{dwell}^{n}$$

For the purpose of the present work the equation above was simplified using the approximation that K_{dwell} is constant throughout each dwell time. This approximation seems reasonable since the applied force is kept constant during each dwell and the crack growth during each dwell is small (<0.01mm). Note that the cyclic part of the equation is the same for both the 30s and 3600s tests.



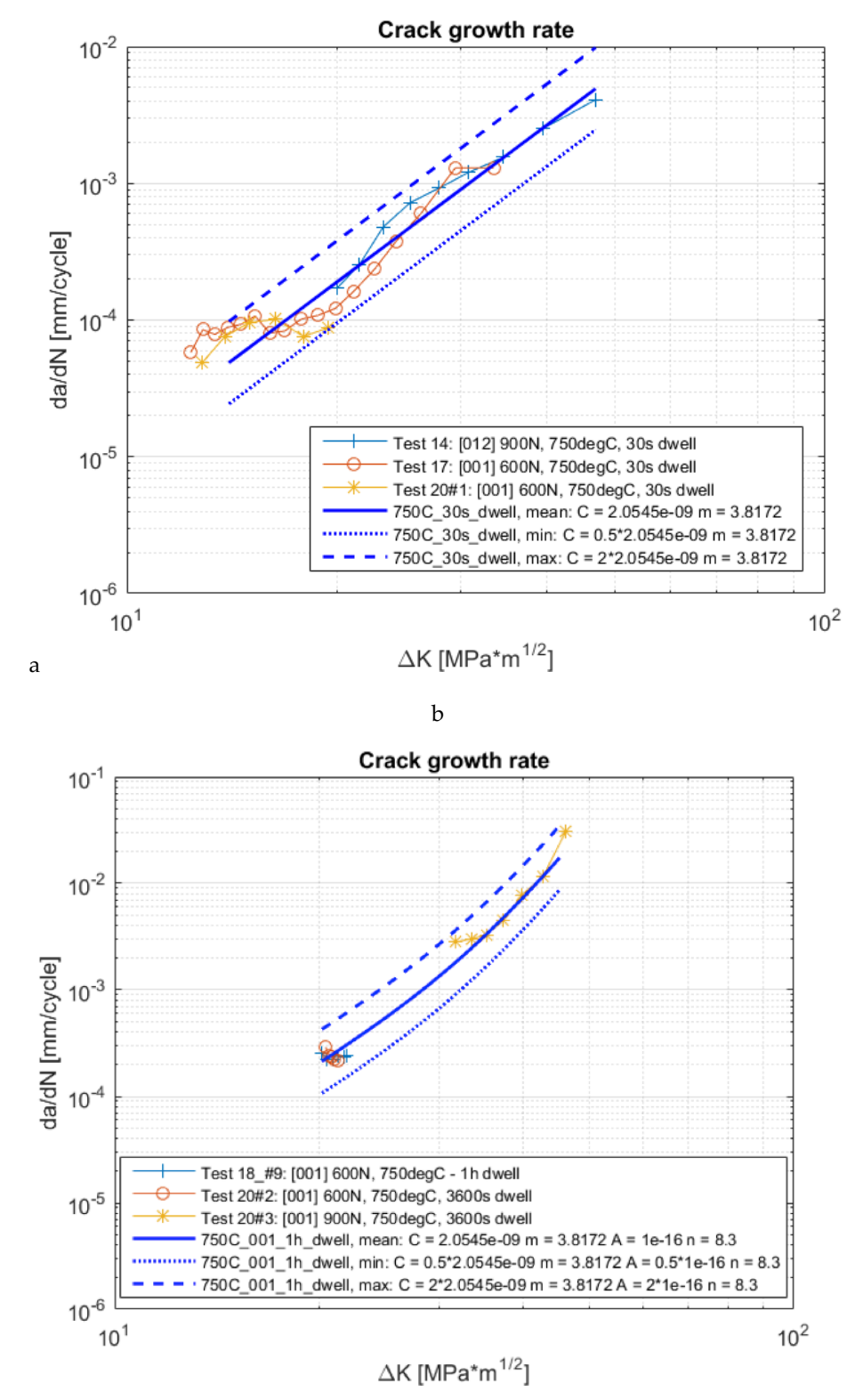


Figure 48 – da/dN vs Δ K at 750°C. a: 30s dwell, <001> and <012>, b: 1h dwell, <001>.



3.1.4 Summary of fracture appearance

The fracture appearance of the tested specimens is summarized in Table 4.

Table 4 – Fracture appearance of the tested specimens.

Temperature	Orientation	Fracture appearance	
20°C	<001>	Non-crystallographic, mode I cracking is dominant. Crystallographic	
	<012>	cracking occurs at the surface of the specimens. At the highest stress levels in <001> specimens crystallographic secondary cracks can also	
	<011>	be found in the interior of the specimen.	
500°C	<001>	Initially non-crystallographic, with crystallographic crack facets only forming at the side surfaces of the specimens. As the crack length increased, a point was reached where crystallographic cracks started to propagate into the specimen, so that the fraction of the crack which was crystallographic gradually increased. There was a region in the middle of the crack front where the crack growth remained non-crystallographic throughout the entire test.	
	<012>		
	<011>	Non-crystallographic. Small crystallographic cracks at the specimen side surfaces.	
750°C	<001> 30s dwell	Non-crystallographic Mode I cracking with some short crack branches. Crack branches pass through casting pores.	
	<012> 30s dwell		
	<001> 1h dwell	Non-crystallographic cracking with crack branches. Crack branches pass through casting pores. Cracks have also initiated at casting pores ahead of the final crack tip. Severe crack branching towards the end of the tests, with several branches of similar projected length. Voids are observed ahead of the crack tip (see Figure 47).	

3.1.5 Influence of crystal orientation

The propensity for crystallographic crack growth is strongly dependent on the crystallographic orientation. Crystallographic crack growth was observed in some of the <001> and <012> specimens. In the <011> specimens the main crack was in all cases noncrystallographic. The present evaluation of crack growth rates is limited to noncrystallographic cracks. During non-crystallographic crack growth the influence of crystal orientation on the crack growth rate is small. The da/dN vs ΔK results from all tested orientations were bundled together and one trendline for each temperature/hold time combination was fitted. The results from all orientations was covered by the same scatter band limits required to cover the scatter for one single-crystal orientation (see Figure 40, Figure 45 and Figure 48). The difference in non-crystallographic crack growth rate between the different orientations appears to be smaller than the scatter of the results for a certain crystal orientation.



3.1.6 Influence of temperature

Propensity for crystallographic crack growth

In the present tests, the propensity for crystallographic crack growth along {111} planes were highest at the intermediate temperature of 500°C. At 750°C, no crystallographic crack growth was observed and neither were any deformation bands. It is well known that the critical resolved shear stress for dislocation motion through the γ' phase increases with temperature, in the temperature range from 20°C up to a critical temperature of 700°C-800°C [33][34][35][36]. Based on earlier work on other singlecrystal superalloys it is likely that both primary cube slip and octahedral slip processes are active at 750°C [37]. It seems reasonable that, the reduced tendency for localization of inelastic strain at 750°C results in a reduced tendency for crystallographic crack growth. However, at 20°C it is more surprising to see a low tendency for crystallographic crack growth, since this is the testing temperature where the resistance of the γ matrix towards inelastic deformation is expected to be the highest and at the same time the critical resolved shear stress of the γ' -phase is expected to be the lowest [38]. This would be expected to favor shearing of the γ' -precipitates together with the γ matrix, resulting in localization of the inelastic strain to {111} planes and crack growth along these planes. Previous crack growth studies on CMSX-4 indicate that the propensity for crystallographic crack growth in this alloy is indeed higher at room temperature than at 500°C [39]. The reason for the unexpected crack growth behaviour observed at 20°C in the present work is a topic for future investigation. A possible explanation could be that the resistance of the primary γ' particles towards cutting by dislocations depends not only on the critical resolved shear stress of the individual phases, but also on the γ/γ' misfit and the properties of γ/γ' interface.

Mode I crack growth rate

In Figure 49, the Mode I crack growth rate is plotted vs ΔK for the three different testing temperatures. The crack growth rate increases with increased testing temperature. Data for CMSX-4 reported by Sengupta et al. [40] is also included for comparison (dashed lines). The CMSX-4 data is based on testing without hold time on CT-specimens with the notch oriented along <001>. The trendlines for CMSX-4 have been graphically evaluated by the author of the present work from the plotted results presented by Sengupta et al. A direct comparison between the materials is not possible since the testing conditions, such as temperature, frequency and hold time are not identical. It should be mentioned that Sengupta et al. report crystallographic zig-zag crack growth along {111} planes in the tests at 20°C, whereas non-crystallographic fracture in the gamma channels is observed in the present work.



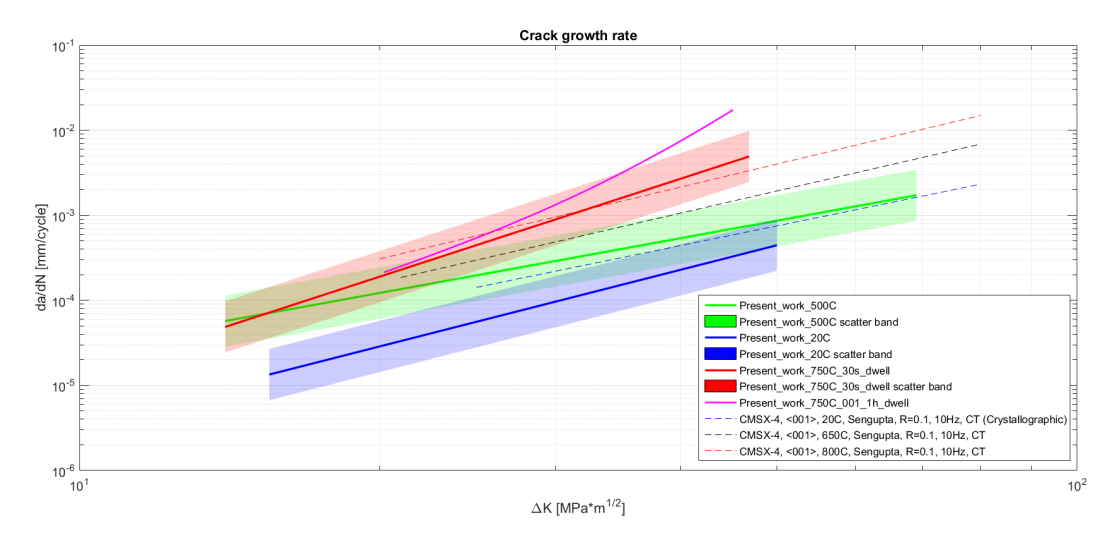


Figure 49 – Mode I crack growth rates of the present work, compared with previously published data for CMSX-4. The data for CMSX-4 at 20° C

3.1.7 Influence of hold time

At 750°C in the <001> direction two tests were run where the hold time at maximum load was varied in testing blocks of 30s, 1h or 24h hold time. The results from all tests at 750°C can be found in Figure 50. The number of cycles in each testing block was not predefined. The switching between the blocks was done manually by the test operator, in order to generate as useful hold time crack growth data as possible while keeping the overall duration of the test reasonable. In test 18, no data is given for the first block #1, since no crack growth was detected. In test 20, between block 20#2 and 20#3 the load was increased.

Steady-state crack growth

At low ΔK (<20MPa*m^0.5) the crack growth during the 1h and 24h dwell blocks did not approach any steady-state, but transient crack growth was observed throughout the whole duration of these testing blocks. Therefore, the hold time influence on the steady-state crack growth can only be evaluated for ΔK >20MPa*m^0.5. See Figure 51a.

At intermediate ΔK (20-22MPa*m^0.5) it appears that steady-state crack growth is approached during the 1h dwell time blocks and the steady state crack growth rate is almost identical to the crack growth rate observed during 30s dwell (see Figure 51). At high ΔK (ΔK >30MPa*m^0.5, da/dN>10^-3mm/cycle), steady-state crack growth occurs at a higher rate with 1h hold time than with 30s hold time, see Figure 50 and Figure 51. Based on these observations the crack growth rate with 1h dwell at maximum load can be roughly approximated by the trendline shown in Figure 50 and Figure 49.



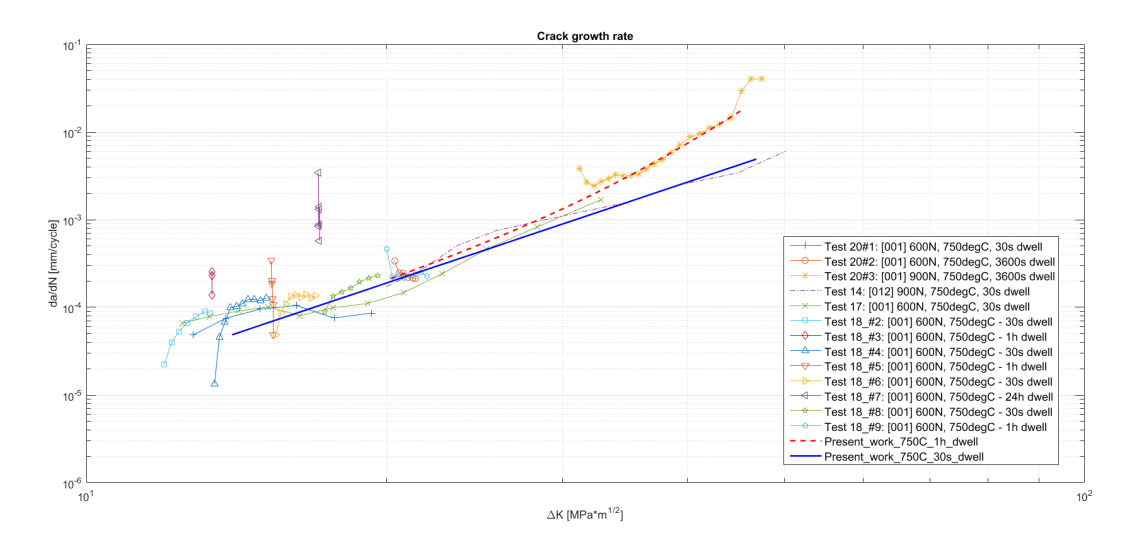
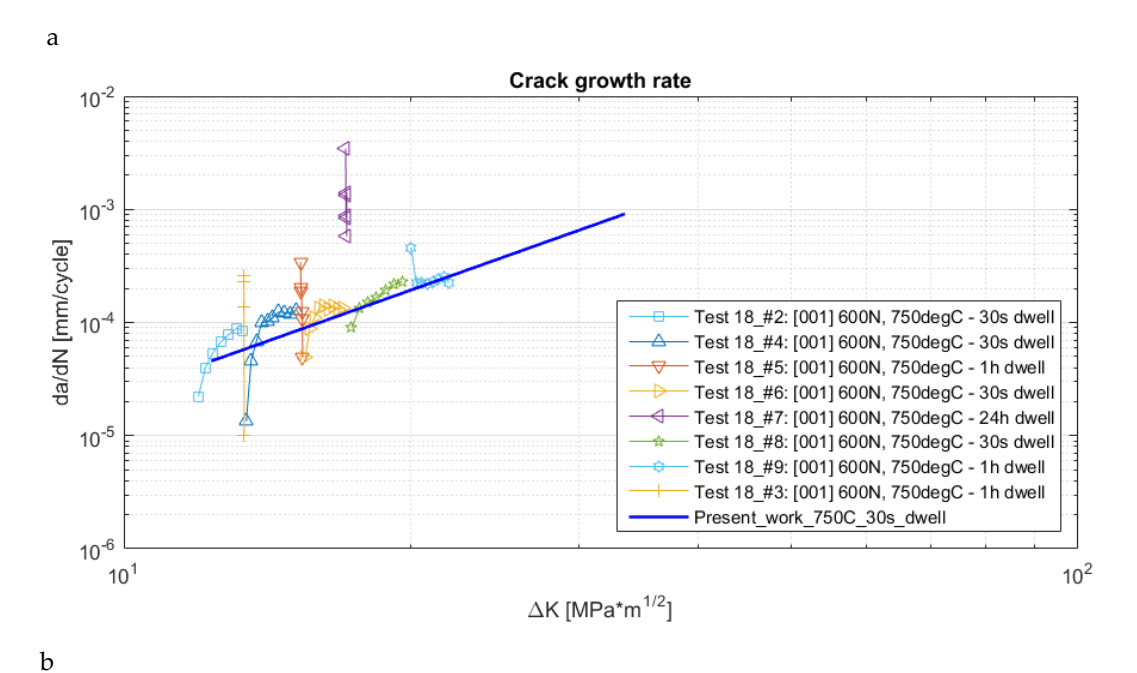


Figure 50 - da/dN vs Δ K for all tests at 750°C. In test 20, between block 20#2 and 20#3 the load was increased. In test 18, no data is given for the first block #1, since no crack growth was detected.

Transient crack growth

In the 1h hold time blocks at low ΔK (<20MPa*m^0.5) the crack growth rate was initially higher than with 30s hold time but then dropped down to a level even lower than the baseline for 30s hold time (see Figure 51a). As the hold time was switched back to 30s, the crack growth rate increased above the baseline level and then appeared to approach the baseline level. In block 7, where the hold time was 24h per cycle, the crack growth rate was initially very high, but immediately started to decrease. 13 cycles were run with 24h hold time, resulting in approximately 0.01mm of crack growth. If a larger number of cycles had been run with 24h hold time it seems likely that the crack growth rate would have dropped down to or below the baseline level in a similar way as in the 1h hold time tests. The reason for this transient hold time influence has not been investigated, but it seems likely that it is related to creep deformation and creep relaxation, which leads to crack tip blunting, and possibly also to oxide induced crack closure.





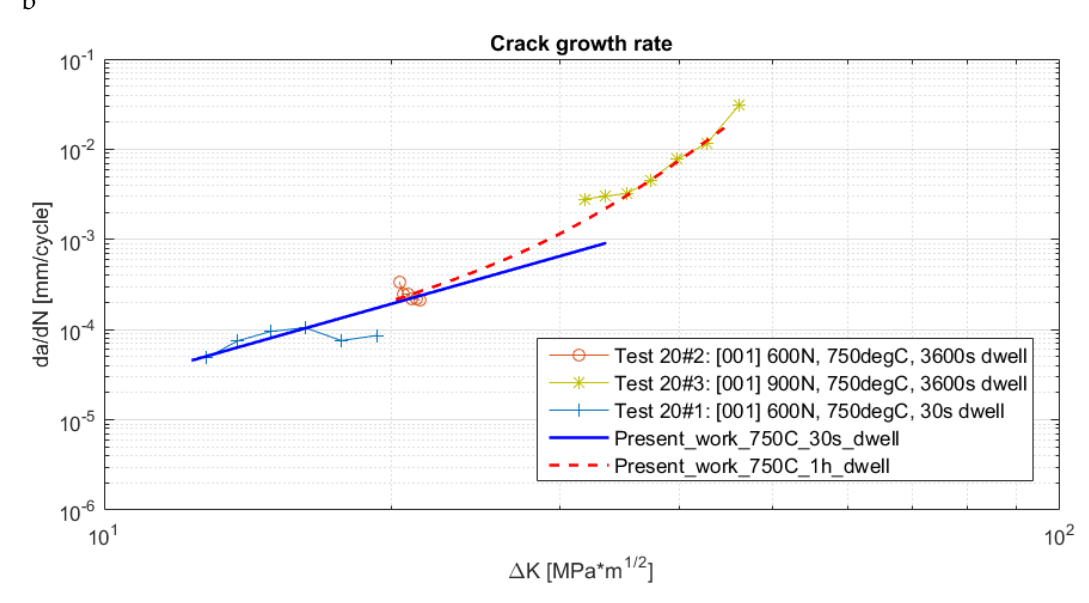


Figure 51 - a: DCT18 at 750° C with blocks of 30s, 1h and 24h hold time. b: DCT20 at 750° C initially with 30s hold time and then with 1h hold time. Between block 2 and 3 the load was increased.

3.2 TMF CRACK GROWTH RESULTS AND ANALYSES

3.2.1 IN792 IP-TMF compared to isothermal results

Figure 52 gives an overview of all the in-phase (IP) TMF and isothermal test results (using the Kb-specimen) done on IN792 to show how the curves for the different temperatures are located with respect to each other.

As seen more in detail in Figure 53, the isothermal tests at 500°C result in a distinct position and angle for the Paris region of steady state crack growth. No equivalent IP-TMF tests have been made for comparison at this temperature.



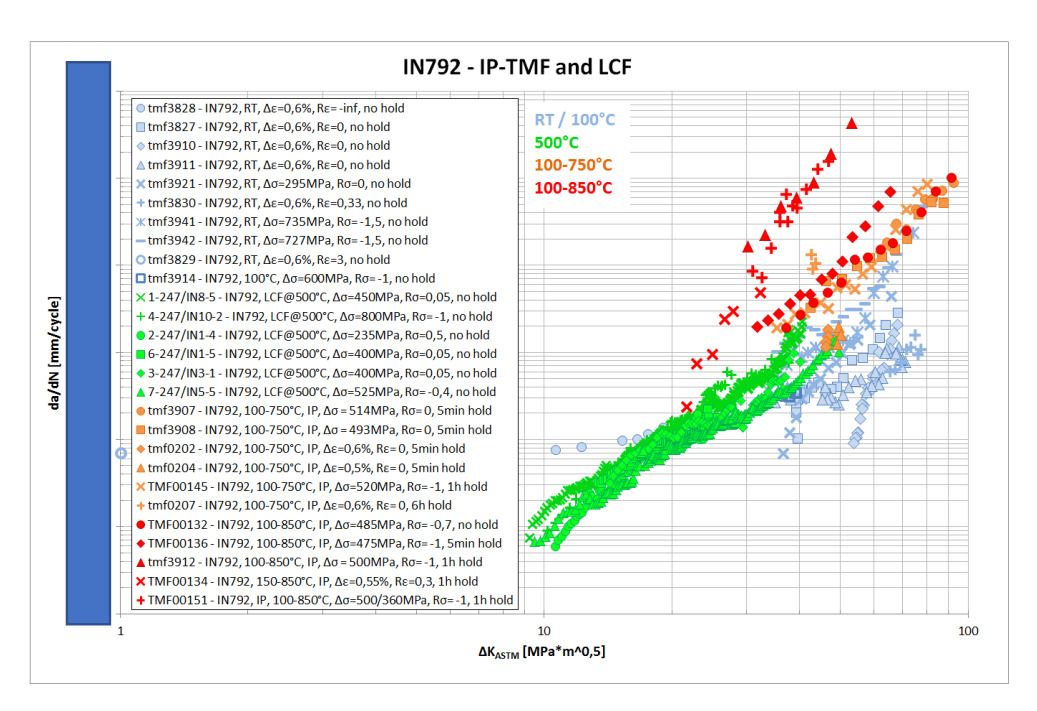


Figure 52 - da/dN vs ΔK_{ASTM} for IN792 under IP-TMF and LCF at different temperatures, including hold time data at the higher temperatures.

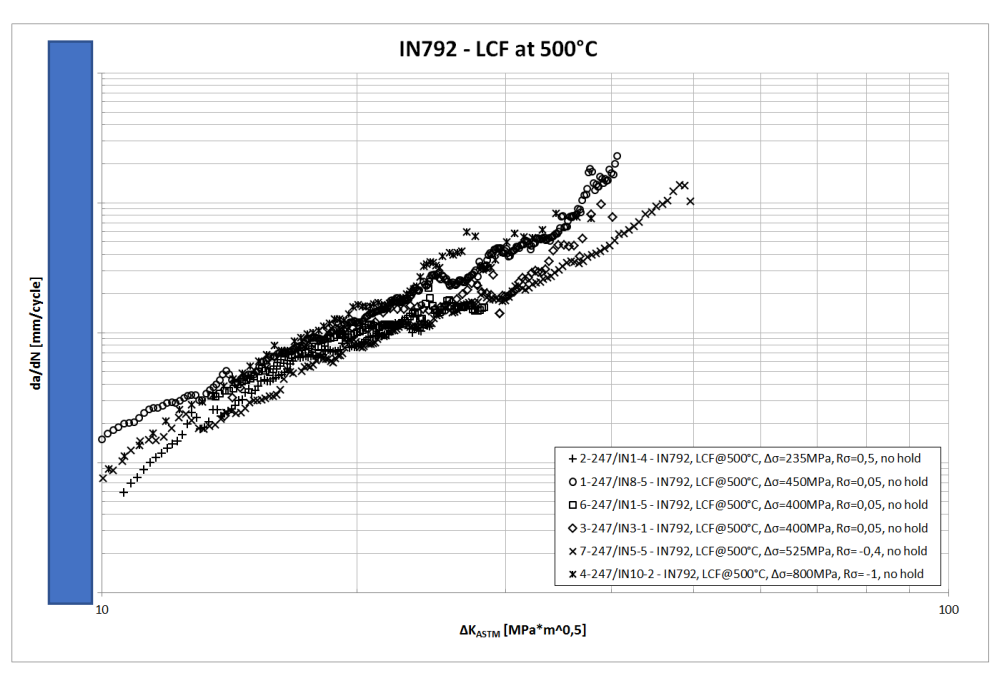


Figure 53 - da/dN vs ΔK_{ASTM} for IN792 under LCF at 500°C. Tests performed by Metcut on KB-specimens.

For crack growth of IN792 in the temperature range 100-750°C and 100-850°C, both IP-TMF and OP-TMF data have been generated. By plotting the crack growth rate per cycle, da/dN vs ΔK_{ASTM} for IP-TMF loading with and without hold time for the two temperatures it can be concluded that while IN792 displays only a minor hold time influence at 750°C (Figure 54), there is a strong hold time influence at 850°C, which



increases with increasing ΔK_{ASTM} (Figure 55), see Almroth and Gustafsson [41] for a more detailed discussion.

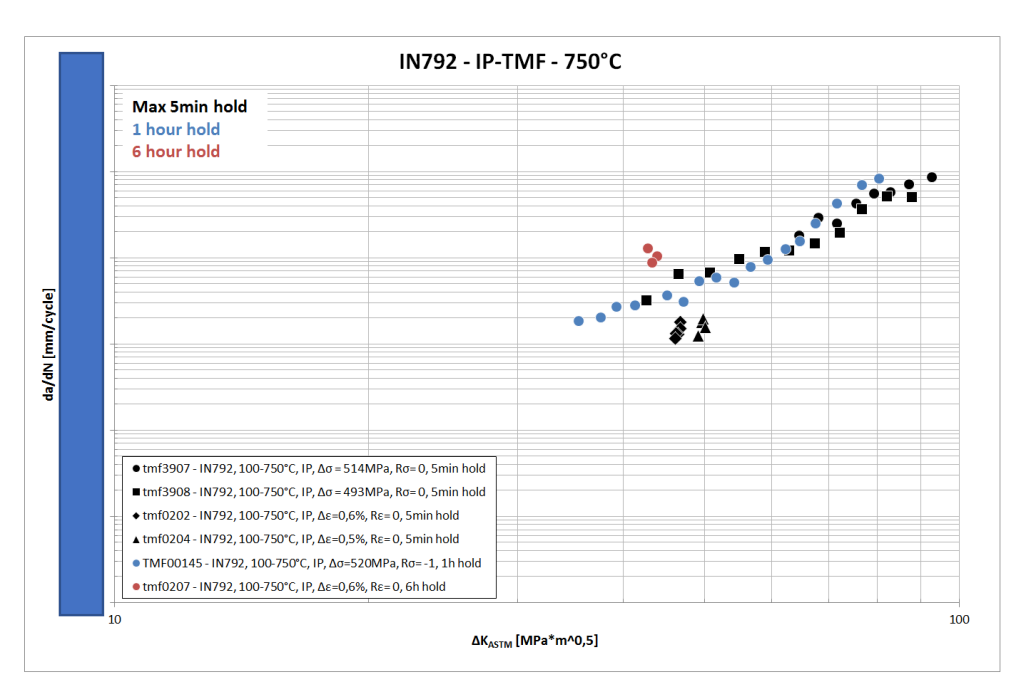


Figure 54 - da/dN vs ΔK_{ASTM} for IN792 under IP-TMF at 100-750°C.

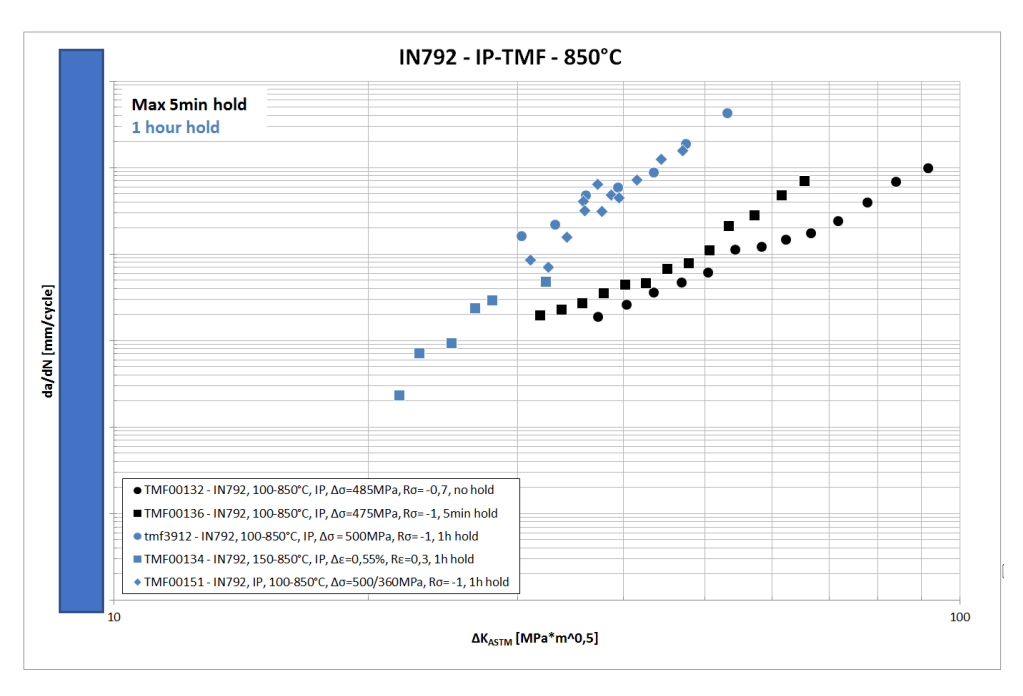


Figure 55 - da/dN vs ΔK_{ASTM} for IN792 under IP-TMF at 100-850°C.



3.2.2 IN792 OP-TMF

For the OP TMF tests, the maximum stress intensity factor occurs in the low temperature part of the temperature cycle. Having this in mind it is interesting to observe that a higher crack growth rate than intuitively could be expected is found for the OP TMF tests, as the data does not collapse on to the same trend-line as for the low temperature isothermal tests, see Figure 56.

Furthermore, the OP TMF tests are not showing any significant influence of maximum temperature or dwell time.

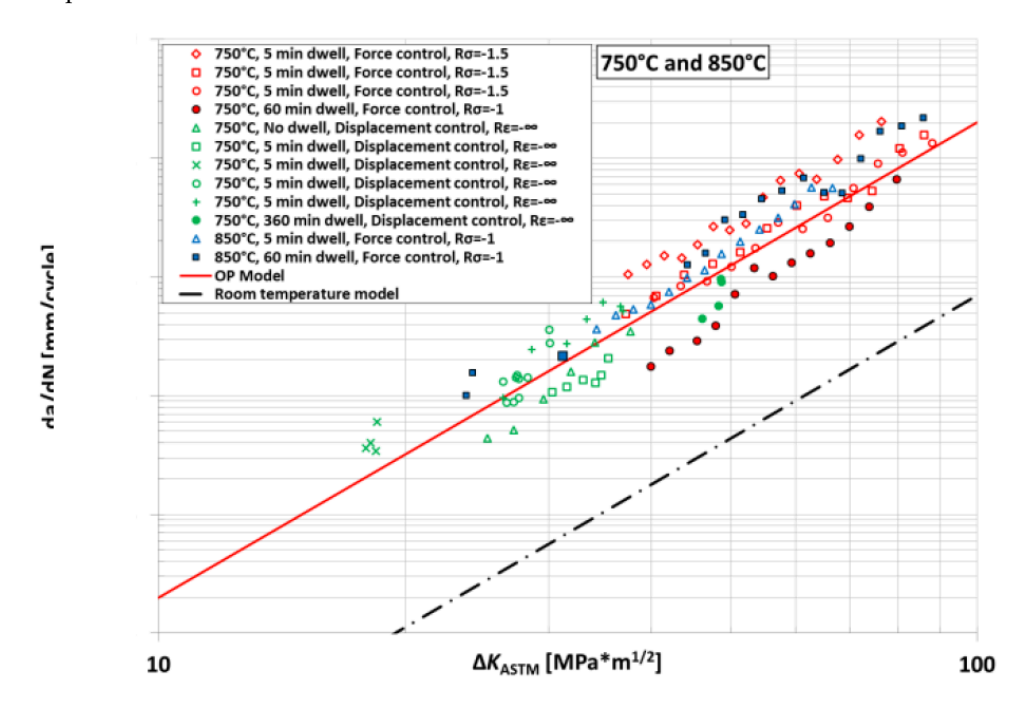


Figure 56 - da/dN vs ΔK_{ASTM} for IN792 under OP-TMF at 100-750°C and 100-850°C. From Almroth et. al. [41]

3.2.3 IN792 crack propagation mechanisms

The crack propagation mechanisms have been studied in more detail by Kontis et. al. [42] and the main findings are summarized below.

The crack propagation during TMF in the temperature range 100-750°C is mainly transgranular, except for IP TMF tests with longer dwell times were intergranular cracking was observed. For OP TMF tests with longer dwell times oxidation assisted recrystallization was observed along the crack path.

A substantial fraction of the MC carbides were found to have cracked after IP testing; voids were also observed to form at the interface between MC and the γ/γ' microstructure. The significant accumulation of plasticity around cracked MC carbides was confirmed by EBSD strain mapping.



3.2.4 STAL15 SX IP-TMF compared to isothermal results

In Figure 57 below, the fatigue crack growth rates of STAL15 SX vs Δ Kastm during isothermal conditions at 750°C are compared to the IP-TMF crack growth tests in the temperature range 100-750°C.

One can see that the IP-TMF tests with no dwell are in good agreement with the isothermal tests with no or just very short (30s) dwell time while the IP-TMF tests with longer dwell times shows an increased crack propagation rate.

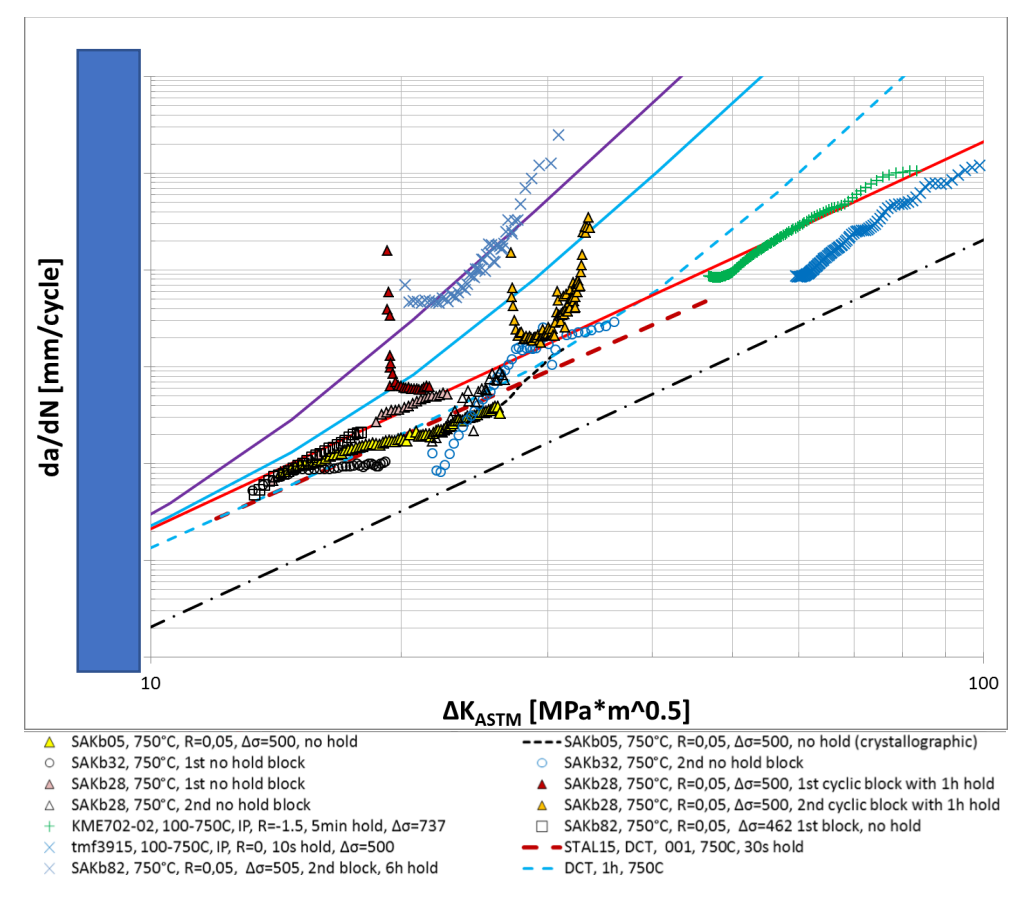


Figure 57 – da/dN vs ΔK_{ASTM} for STAL15 SX at 750C.



3.2.5 STAL15 SX OP-TMF

The crack growth rate of STAL15 SX vs Δ Kastm under OP-TMF is shown in Figure 58. In cases where the crack propagated in a crystallographic manner (non-perpendicular to the loading direction), the crack growth rate has been plotted as a dashed line. The hold time at maximum temperature was varied between 10s and 1h. This variation in hold time had little or no influence on crack growth rate under OP-TMF. A calibration of a material model for polycrystalline superalloys (as described in a separate Siemens report) has been included for comparison. It can be seen that the crack growth rate during non-crystallographic, Mode I crack growth, is similar to that of the polycrystalline alloys. The max and min lines were obtained by multiplying the average line by factors of 10 and 0.1 respectively.

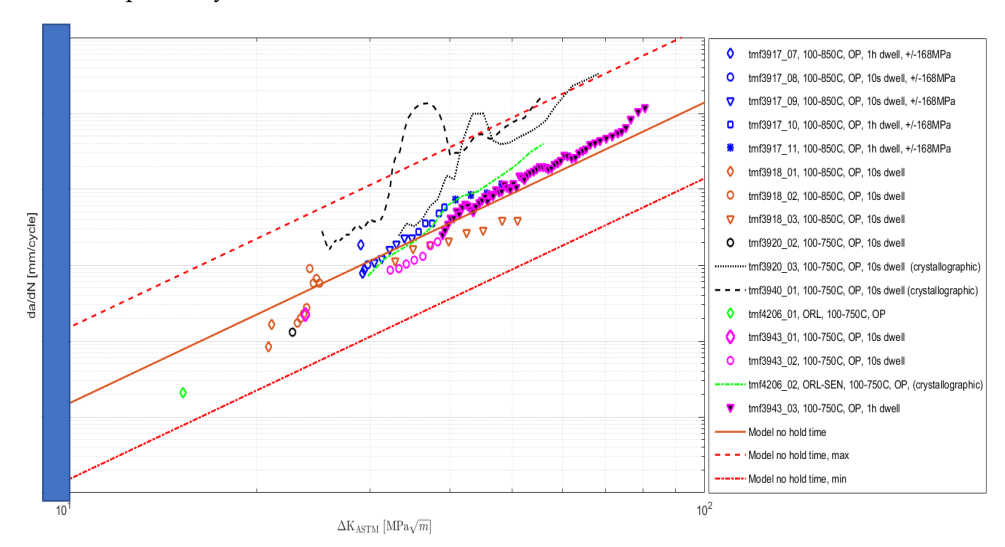


Figure 58 – da/dN vs ΔK_{ASTM} for STAL15 SX under OP-TMF. A crack growth model calibrated for the polycrystalline blade alloys IN792 and Alloy 247 is included for comparison.

3.2.6 Influence of long term ageing on TMF properties of STAL15

In order to investigate the effect of long term ageing on the TMF crack growth resistance of STAL15, samples have been subjected to 50 precycles in order to accumulate some plastic strain in the samples after which they have been exposed to elevated temperature (850°C). The exposure time will be varied between 4000 to 10.000 hours. Some samples exposed to 4000 hours are currently under testing and the samples to be tested after 10.000 hours of exposure is still within the furnace.



3.3 MODELLING RESULTS

3.3.1 Numerical study of the influence of crystallographic orientation and misalignments

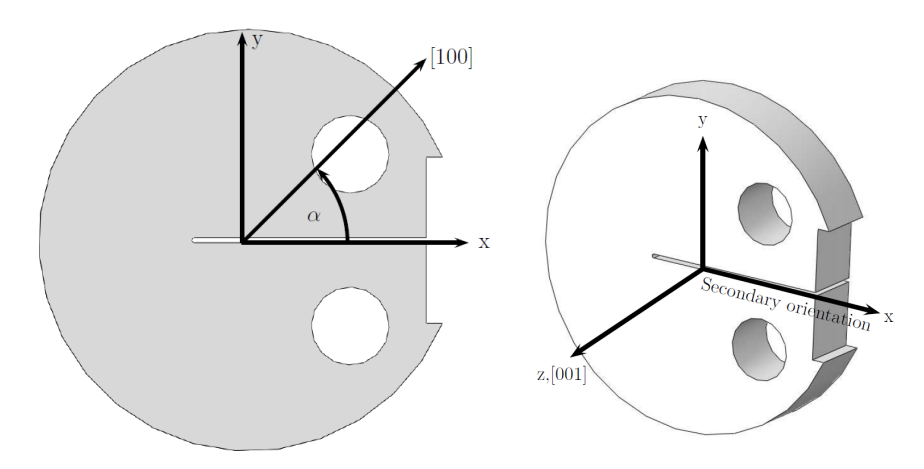


Figure 59 - First set of simulations (S1): with ideal [001].

The first set of simulations considers a rotation of the secondary crystal direction around the model's z-axis which is aligned with the [001] crystal direction. That way the secondary orientation [100] rotates from being aligned with the model's x-axis at 0° to being aligned with the positive y-axis at 90° , cf. α in Figure 59. Simulations are performed for $\alpha = 0^{\circ}$ to 90° in steps of 10° as well as for $\alpha = 45^{\circ}$.

Second set of simulations (S2): with 10° misalignment of the primary orientation. In this set of simulations, not only the different secondary orientations, but also a misalignment of the model's primary orientation is taken into account. The two subsequent rotations can be seen in Figure 60. The ideal crystal orientation is shown in Figure 60a). Then the crystal is rotated around the z-axis by α = [0°: 10°: 90°] as in the first set of simulations, cf. Figure 60b). Additionally, the misalignment of the [001] crystal direction is simulated, where the negative rotation around the new [010] axis is expressed by the angle θ , which indicates the misalignment. For all simulations with different secondary directions θ is taken as 10° due to the previously explained reason. In Figure 61, K_I is depicted as a function of the secondary orientation in terms of the angle α .



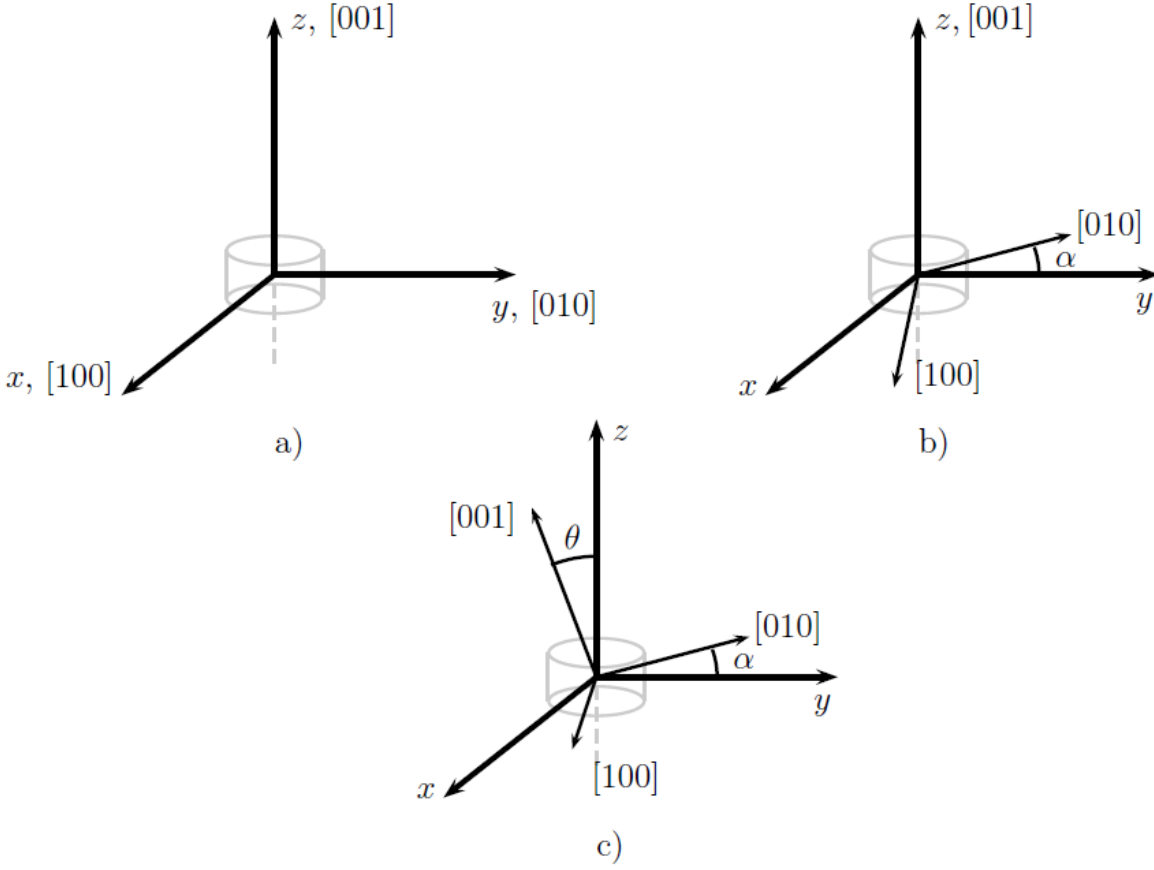


Figure 6060 - Definition of the specimen misalignment of the crystal orientation. a) ideal orientation, b) positive rotation around [001] by α and c) negative rotation around new [010] by θ .

The maximum SIFs for each rotation step around the [001] crystal direction are depicted in Figures 61, 62 and 63. This is done for the S1 and S2. A benchmark solution for the same test specimen considering an isotropic material behaviour is included. It can be seen that the K_I components of the SIFs for S1 are symmetric with respect to α = 45°. The SIFs increase up to α = 45° and then decrease when α approaches 90°. The K_{II} and K_{III} components are negligibly small for S1, cf. Figure 62 and 63, respectively. For S2 a similar behaviour as S1 can be observed. The K_I components of the SIFs increase to a maximum at α = 45° and then decrease without symmetry. The K_I value at α = 90° is lower than at α = 0°. The K_I values for the isotropic material simulation constant, due to the isotropic material behaviour. When comparing S1 and S2 it can be seen that they differ without symmetry. The K_I value at α = 90° is lower than at α = 0°. The K_I values for the isotropic material simulation stay constant, due to the isotropic material behaviour. The K_{II} and K_{III} components of S2 are increasing and decreasing, respectively, with increasing angle

Furthermore, the K_I values along the normalized crack front are shown for the case of α = 0° and α = 90° for S1 and S2, cf. Figure 64. It can be seen that K_I deviates substantially from each other for both cases.



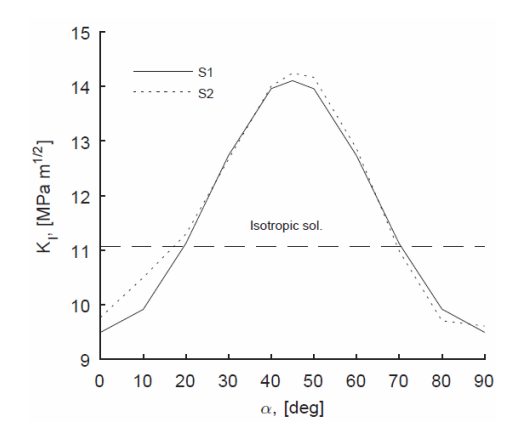


Figure 61 - Mode I SIF as a function of the secondary orientation

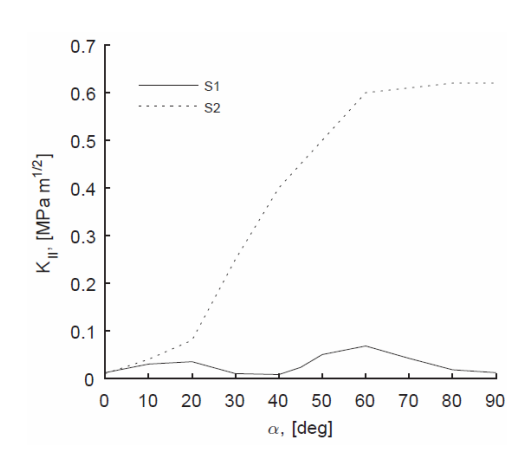


Figure 62 - Mode II SIF as a function of the secondary orientation

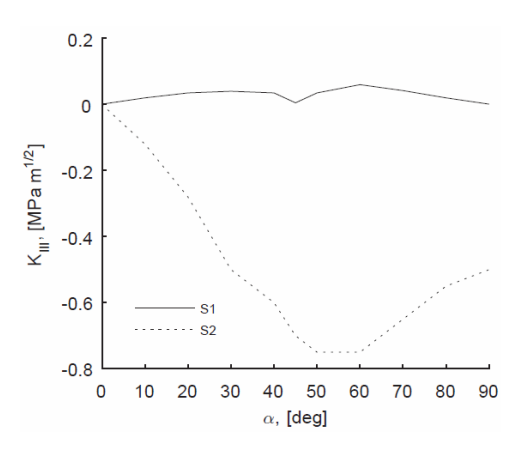
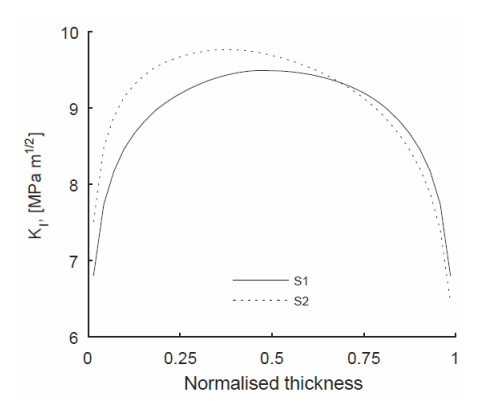


Figure 63 - Mode III SIF as a function of the secondary orientation





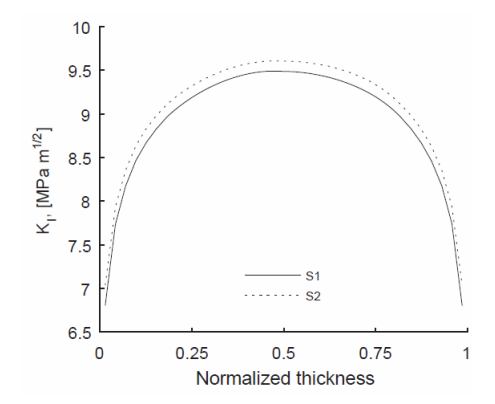


Figure 64 - Mode I SIF along the normalized distance for α =0° (left) and α =90° (right).

In Figure 61 it can be seen that K_1 received from S1 increases from $\alpha = 0^{\circ}$ to a maximum at $\alpha = 45^{\circ}$ and then decreases till $\alpha = 90^{\circ}$ in a symmetric manner. This can be explained by the different stiffnesses in the different crystal orientations. This explains also the maximum at α = 45° when the load direction is in the [011] crystal direction, where the highest stiffness in load direction is present for all angles α . This shows that it is important to account for the different crystal orientations even for an ideal case without misalignment of the [001] direction. In S2 a misalignment in the primary orientation is accounted for by a deviation of $\theta = 10^{\circ}$. It can be seen that the misalignment has a great influence on the SIFs. The solution of the simulation with the isotropic material K₁ values constant for all angles α . When comparing the isotropic and anisotropic simulations, where the same Young's modulus and Poisson's ratio is used (from $\alpha = 0^{\circ}$), it can be seen that they differ. Tinga [17] observed that only the change from isotropic to anisotropic material properties more than doubled the K₁ values for a normal crack orientation. The SIFs in this study confirm his observation with an increase in K_I. This difference can be explained by the influence of anisotropy which changes the local stress state in the vicinity of the notch. Thus, the results suggest that it is important to employ an anisotropic material behaviour to account for multi-axial stresses. In Figure 62 and Figure 63 it can be seen that the K_{II} and K_{III} components stay at around zero for S1. The small values which are present are due to the above explained complex stress state at the vicinity of the notch. For S2 the K_{II} and K_{III} components increase with increasing α . This shows that the misalignment causes shear stresses at the crack tip. In the Figure 64 it can be also seen that the shape of the crack front K₁ values deviate if the misalignment in [001] is accounted for. Especially for the $\alpha = 0^{\circ}$, where the K_1 values are distributed differently along the crack front. This implies that the crack will grow in different directions in the component if a misalignment is present. Accounting for this phenomenon can be of great importance for the industry. The K_I values along the crack front are also presented for $\alpha = 90^{\circ}$ and it can be seen that even though the shape of the SIF distribution is similar, the magnitude is different. It can be seen how important it is to account for the correct crystal orientation since it influences the crack growth and fatigue life behaviour of a component. This can be of much importance in, for example, the blade fir tree root where a local multi-axial stress state is present, even though the blade is cast and loaded in [001] direction.



3.3.2 Crystallographic crack driving force

In this section the above described (see Section 2.7.3) equivalent RSIF parameter keg is evaluated according to the two above presented models. As explained above, the mean value and the error ranges due to inaccuracies of determining the crystallographic orientations were accounted for by evaluating all possible combinations of the generated angles with their standard deviations, thus yielding 729 different sets of crystallographic orientations. The 729 evaluations gave a range for the different kep parameter values that can be understood as one set that corresponds to e.g. the mean of the measured angles and an error range corresponding to the standard deviation in the 95% confidence interval for the measured angles of the dendrites. The lower boundary of the error range was determined by the crystallographic orientation that results in the lowest sum of keq values summed over all nodes along the crack front. Equally so for the upper boundary with its highest total keq parameter value. These need not necessarily correspond to the minimum and maximum angles in the confidence interval of the measured dendrites. This procedure is based on the fact, that the change of crystallographic orientation has the same effect on the keQ values for all nodes along the crack front, and results thus only in an up- or downwards shift of the k_{EQ} -curve. Incorporating the error ranges in the two models, the keq parameter values were evaluated for all specimens and are displayed in Table 5. For Model 1 it can be seen that only the slip direction with the highest keq value on the on each of the slip planes is presented for each side of the crack. For Model 2 the keq value is presented for all slip planes on each side of the crack. The presented values for the left (L) and right (R) side of the specimens were evaluated at a normalised crack front distance of 0.05 and 0.95, respectively, cf. Figure 65.

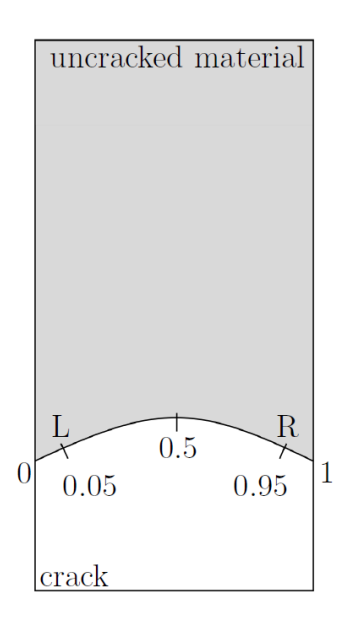


Figure 65 - Normalized distance along the crack front

This is done to avoid numerical errors that occur due to a change of order of the singularity when the crack approaches a free surface of the FE-model. The plane deformation condition is assumed to hold all the way to the free surface when computing the anisotropic SIFs, even though this is not true. More importantly, it is difficult to generate well shaped elements at the crack front near a free surface, and the local errors due to elements that are poorly shaped and not symmetrical about the crack front lead to errors. Furthermore, it could be observed from the experimental results that the location of the cracking mode transition occurred at the surface of the specimen. Hence, the results from the FEsimulations were extracted and evaluated here (at 0.05 and 0.95 along the normalised crack front distance). The evaluated crack lengths in the FE-simulations correspond to the experimentally found crack lengths for the transition from Stage II to Stage I cracking. As the transition crack lengths were different in each of the specimens, and also the lengths of the crack fronts, a

direct comparison between the specimens could not be performed with the normalised crack front lengths. To determine if the correct Stage I cracking plane is predicted with the proposed crystallographic crack growth parameter, the crystallographic planes with the highest keq values at each side of the specimens are to coincide with the Stage I cracking planes in the experiments. Thus, when evaluating keq it can be seen that this is possible. For instance, from the simulations of the Kb1 specimen, it can be seen in Table 5 that on the left side the (~11~1)-plane and on the right side the (~11~11)-plane experience



the highest stress intensities in terms of keq. This can be validated by the experiments which show that the Stage I crack started to grow on these two planes on the corresponding sides. The Stage I crack initiates first on the (-11-1)-plane at a crack length of 0.95 mm and then at 1 mm on the (~1~11)-plane, where a slightly higher keq value for the (-11-1)-plane than for the (-1-11)-plane is obtained in the evaluations. This means that at the crack length of 0.95 mm the transition to the (~11~1)-plane occurs on the left side before the crack transition to the ('1-11)-plane on the right side. Employing the same argument in the other simulations, it can be stated that the correct crystallographic plane on which Stage I crack growth first occurs is predicted in all investigated cases using the keq parameter. It should be noted, that the models are only able to predict the first occurrence of transition to Stage I crack growth. This is due to a redistribution of the stress state when the crack transitions to a Stage I crack on one side of the specimen, since this changes the crack geometry and the stress state. Thus, the presented framework is only valid for the prediction of the Stage I cracking plane of the first transition from Stage II to Stage I cracking or when the transition occurs almost simultaneously, i.e. the stress state and crack shape do not change in any greater extent.

For Kb4 and DCT3, Model 1 predicts the correct Stage I cracking plane only when accounting for the error ranges in the crystallographic orientations. The uncertainties about the crystallographic orientation is especially high in these two specimens, see the higher RMSE-values in Table 5. Thus, it is reasonable to employ the error ranges in these cases. This is exemplified in Figure 66, where the keq parameter is presented as a function of the normalised distance along the crack front for Kb4. It can be seen that only by including the error ranges, which are depicted as shady surfaces, the experimentally observed Stage I cracking plane could be predicted. The curves oscillate because of the geometrical intersections of the crack front coordinate system with the evaluation directions, which is defined in the material coordinate system. Thus, a higher curvature of the crack front results in more oscillation of the curves. Model 2 shows a good capability to predict the correct Stage I cracking planes, when employing the error margins for Kb2, Kb4 and DCT3 it could predict the correct crystallographic slip planes in all specimens.

The importance of the crystallographic orientation can directly be seen in the $k_{\rm EQ}$ magnitudes of the error ranges in Table 5. Depending on the standard deviations for the measured angles the error ranges are smaller or bigger, and can have a major influence on the results. This shows the importance of the material orientation when computing the RSIF parameters.



Table 5 - Summary of the k_{EQ} parameter results. The three presented values are; lower limit of the error range < mean value < upper limit of the error range. The grey highlighted results represent the active slip plane observed in the experiments and the number in parenthesis for Model 1 represents the slip system

$ \text{Kb1} = \begin{cases} $			Side	k_{EQ} on (111)-plane	k_{EQ} on (1 $\bar{1}\bar{1}$)-plane	k_{EQ} on (111)-plane	k_{EQ} on (111)-plane
$ \begin{array}{c c c c c c c c c c c c c c c c c c c $	Kb1	Model 1			6.31 < 6.98 < 7.59 (5)	8.20 < 8.65 < 8.90 (9)	6.97 < 7.64 < 8.18 (11)
$ \begin{tabular}{ c c c c c c c c c c c c c c c c c c c$			R	7.45 < 8.05 < 8.48 (2)	8.05 < 8.40 < 8.75 (6)	6.04 < 6.72 < 7.40 (8)	8.20 < 8.55 < 8.85 (12)
$ \text{Ke} \\ \text{Ke} \\ \text{Ke} \\ \text{Hodel 1} \\ \text{L} \\ \text{2.90} < 3.315 < 3.36 (1) \\ \text{2.81} < 2.92 < 3.03 (5) \\ \text{3.23} < 3.44 < 3.58 (4) \\ \text{2.83} < 2.94 < 3.04 \\ \text{2.90} < 3.10 < 3.10 < 3.21 < 3.24 < 3.34 \\ \text{2.83} < 2.94 < 3.04 \\ \text{2.90} < 3.10 < 3.21 < 3.24 < 3.34 \\ \text{2.83} < 2.94 < 3.04 \\ \text{2.90} < 3.10 < 3.21 < 3.24 < 3.40 \\ \text{2.90} < 3.10 < 3.21 (10) \\ \text{2.83} < 2.94 < 3.04 \\ \text{2.90} < 3.10 < 3.21 (10) \\ \text{2.83} < 2.94 < 3.04 \\ \text{2.90} < 3.10 < 3.21 < 3.24 < 3.40 \\ \text{3.67} < 3.85 < 4.13 \\ \text{2.89} < 3.06 < 3.21 \\ \text{4.04} < 4.19 < 4.35 \\ \text{4.19} < 4.35 \\ \text{4.19} < 4.35 \\ \text{4.19} < 4.35 \\ \text{4.10} < \text{4.10} < 4.35 \\ \text{4.10} < 4.35 \\ \text{4.10} < \text{4.11} < \text{4.10} < 4.35 \\ \text{4.10} < \text{4.10} < \text{4.21} < \text{1.10} \\ \text{4.10} < \text{4.10} < 4.35 \\ \text{4.10} < \text{4.10} < \text{4.21} < \text{1.10} \\ \text{4.10} < \text{4.10} < \text{4.21} < \text{4.10} < \text{4.10} \\ \text{4.10} < \text{4.10} < \text{4.10} < \text{4.10} < \text{4.10} \\ \text{4.10} < \text{4.10} < \text{4.10} < \text{4.10} \\ \text{4.10} < \text{4.10} < \text{4.10} < \text{4.10} \\ \text{4.10} < \text{4.10} < \text{4.10} < \text{4.10} < \text{4.10} \\ \text{4.10} < \text{4.10} < \text{4.10} \\ \text{4.10} < \text{4.10} < \text{4.10} < \text{4.10} \\ \text{4.10} < \text{4.10} < \text{4.10} < \text{4.10} \\ \text{4.10} < \text{4.10} < \text{4.10} \\ \text{4.10} < \text{4.10} < $		Model 2	L	9.25 < 9.65 < 9.9	7.62 < 7.97 < 8.21	9.70 < 10.02 < 10.25	8.32 < 8.51 < 8.76
$ \begin{array}{c ccccccccccccccccccccccccccccccccccc$			R	8.84 < 9.11 < 9.31	9.60 < 9.95 < 10.15	7.14 < 7.53 < 7.72	9.43 < 9.82 < 10.10
$ \begin{array}{c ccccccccccccccccccccccccccccccccccc$	Kb2	Model 1	L	2.90 < 3.15 < 3.36 (1)	2.81 < 2.92 < 3.03 (5)	3.24 < 3.44 < 3.57 (7)	2.86 < 2.93 < 3.04 (11)
$ \begin{tabular}{ c c c c c c c c c c c c c c c c c c c$			R	2.78 < 2.88 < 2.98 (2)	3.23 < 3.44 < 3.58 (4)	2.83 < 2.94 < 3.04	2.90 < 3.10 < 3.31 (10)
$ \begin{tabular}{ c c c c c c c c c c c c c c c c c c c$		Model 2	L	3.87 < 3.93 < 4.15	2.95 < 3.06 < 3.19	4.05 < 4.18 < 4.32	3.11 < 3.28 < 3.43
$ \begin{tabular}{ c c c c c c c c c c c c c c c c c c c$			R	3.12 < 3.24 < 3.40	3.67 < 3.85 < 4.13	2.89 < 3.06 < 3.21	4.04 < 4.19 < 4.35
$ \begin{array}{c ccccccccccccccccccccccccccccccccccc$	Kb3	Model 1	L	1.93 < 2.04 < 2.13 (1)	1.76 < 1.91 < 2.06 (5)	2.14 < 2.24 < 2.31 (7)	1.86 < 1.97 < 2.11 (11)
$ \begin{array}{c ccccccccccccccccccccccccccccccccccc$			R	1.72 < 1.79 < 1.94 (2)	2.13 < 2.25 < 2.33 (4)	1.77 < 1.92 < 2.43 (8)	1.90 < 2.03 < 2.13 (10)
$ \begin{tabular}{ c c c c c c c c c c c c c c c c c c c$		Model 2	L	2.34 < 2.58 < 2.71	1.91 < 2.05 < 2.19	2.56 < 2.74 < 2.91	2.13 < 2.28 < 2.44
$ \begin{tabular}{ c c c c c c c c c c c c c c c c c c c$			R	1.98 < 2.11 < 2.27	2.53 < 2.72 < 2.85	1.95 < 2.07 < 2.20	2.33 < 2.48 < 2.62
$ \begin{array}{c ccccccccccccccccccccccccccccccccccc$	Kb4	Model 1	L	5.81 < 6.21 < 6.54 (3)	5.18 < 5.22 < 5.32 (6)	6.43 < 6.77 < 7.06 (9)	6.47 < 6.90 < 7.27 (11)
$ \begin{array}{c} \operatorname{Model} 2 & L & 7.31 < 7.62 < 7.94 & 5.70 < 5.98 < 6.22 & 7.51 < 7.89 < 8.21 & 7.30 < 7.59 < 7.71 \\ 7.19 < 7.51 < 7.81 & 7.59 < 7.93 < 8.29 & 5.31 < 5.58 < 5.84 & 7.54 < 8.06 < 8.34 \\ \hline \\ \operatorname{Model} 1 & R & 11.65 < 12.45 < 13.40 (3) & 13.03 < 13.49 < 13.84 (4) & 12.42 < 12.95 < 13.45 (7) & 12.39 < 13.02 < 13.78 (10) \\ \hline \\ \operatorname{Model} 2 & R & 11.70 < 12.33 < 12.87 (3) & 11.98 < 12.52 < 12.91 (4) & 13.15 < 13.78 < 14.3 (7) & 11.07 < 11.75 < 12.42 (10) \\ \hline \\ \operatorname{Model} 2 & R & 13.65 < 14.16 < 14.42 & 14.48 < 14.85 < 15.27 & 15.45 < 15.75 < 16.11 & 13.66 < 13.92 < 14.54 \\ \hline \\ \operatorname{Model} 1 & R & 15.6 < 16.1 < 16.37 (1) & 14.42 < 14.44 < 14.71 (4) & 16.83 < 17.30 < 17.6 (7) & 14.32 < 14.34 < 14.4 (10) \\ \hline \\ \operatorname{Model} 2 & R & 17.02 < 17.41 < 17.75 & 17.65 < 18.00 < 18.21 & 18.31 < 18.78 < 19.24 & 17.84 < 18.08 < 18.43 \\ \hline \\ \operatorname{Model} 1 & R & 17.02 < 17.41 < 17.75 & 17.65 < 18.00 < 18.21 & 18.31 < 18.78 < 19.24 & 17.84 < 18.08 < 18.43 \\ \hline \\ \operatorname{Model} 1 & R & 19.04 < 13.65 < 14.16 < 14.49 & 10.13 < 10.20 (4) & 8.67 < 9.02 < 9.36 (7) & 8.42 < 9.22 < 9.85 (10) \\ \hline \\ \operatorname{Model} 2 & R & 10.65 < 10.91 < 11.27 & 10.63 < 11.06 < 11.52 & 10.01 < 10.30 < 10.52 & 9.51 < 9.96 < 10.27 \\ \hline \\ \operatorname{Model} 2 & R & 6.39 < 6.88 < 7.41 & 10.02 < 10.29 < 10.53 & 11.34 < 11.87 < 12.21 & 9.69 < 9.97 < 10.40 \\ \hline \\ \operatorname{Model} 2 & R & 9.28 < 9.97 < 11.46 (3) & 13.67 < 14.64 < 15.14 (5) & 11.53 < 12.82 < 13.85 (7) & 12.33 < 12.46 < 12.95 (12) \\ \hline \\ \operatorname{Model} 2 & R & 9.28 < 9.97 < 11.46 (3) & 13.67 < 14.64 < 15.14 (5) & 11.53 < 12.82 < 13.85 (7) & 12.33 < 12.46 < 12.95 (12) \\ \hline \\ \operatorname{Model} 2 & R & 10.10 < 10.66 < 11.28 & 16.85 < 17.10 < 17.69 & 16.31 < 17.15 < 17.83 & 9.81 < 10.30 < 10.99 \\ \hline \\ \operatorname{Model} 2 & R & 10.10 < 10.66 < 11.28 & 16.85 < 17.10 < 17.69 & 16.31 < 17.15 < 17.83 & 9.81 < 10.30 < 10.99 \\ \hline \\ \operatorname{Model} 2 & R & 10.10 < 10.66 < 11.28 & 16.85 < 17.10 < 17.69 & 16.31 < 17.15 < 17.83 & 9.81 < 10.30 < 10.99 \\ \hline \\ \operatorname{Model} 2 & R & 10.10 < 10.66 < 11.28 & 16.85 < 17.10 < 17.69 & 16.31 < 17.15 < 17.83 & 9.81 < 10.30 < 10.99 \\ \hline \\ \operatorname{Model} 2 & R & 10.10$			R	6.14 < 6.59 < 6.85 (2)	6.31 < 6.37 < 6.59 (6)	4.40 < 4.91 < 5.45 (9)	6.76 < 7.14 < 7.30 (12)
$ \text{DCT1} = \begin{bmatrix} \text{Model 1} & \text{L} & 11.6 < 7.51 < 7.81 & 7.59 < 7.93 < 8.29 & 5.31 < 5.58 < 5.84 & 7.54 < 8.06 < 8.34 \\ \text{Model 1} & \text{R} & 11.6 < 12.45 < 13.40 (3) & 13.03 < 13.49 < 13.84 (4) & 12.42 < 12.95 < 13.45 (7) & 12.39 < 13.02 < 13.78 (10) \\ \text{Model 2} & \text{R} & 11.70 < 12.33 < 12.87 (3) & 11.98 < 12.52 < 12.91 (4) & 13.15 < 13.78 < 14.3 (7) & 11.07 < 11.75 < 12.42 (10) \\ \text{Model 2} & \text{R} & 13.65 < 14.16 < 14.42 & 14.48 < 14.85 < 15.21 & 14.29 < 14.66 < 15.01 & 13.78 < 14.24 < 14.60 \\ \text{R} & 13.65 < 14.16 < 14.42 & 14.48 < 14.85 < 15.27 & 15.45 < 15.75 < 16.11 & 13.66 < 13.92 < 14.54 \\ \text{Model 1} & \text{R} & 14.79 < 15.15 < 15.49 (1) & 15.94 < 16.27 < 16.64 (4) & 14.70 < 15.08 < 15.42 (7) & 15.94 < 16.42 < 16.82 (10) \\ \text{Model 2} & \text{R} & 15.6 < 16.1 < 16.37 (1) & 14.42 < 14.44 < 14.71 (4) & 16.83 < 17.30 < 17.6 (7) & 14.32 < 14.34 < 14.4 (10) \\ \text{Model 2} & \text{R} & 17.02 < 17.41 < 17.75 & 17.65 < 18.00 < 18.21 & 18.31 < 17.78 < 18.11 & 17.51 < 17.98 < 18.48 \\ \text{Model 1} & \text{R} & 19.24 & 17.44 < 19.775 & 17.65 < 18.00 < 18.21 & 18.31 < 18.78 < 19.24 & 17.84 < 18.08 < 18.43 \\ \text{Model 2} & \text{R} & 7.09 < 8.27 < 9.08 (3) & 8.84 < 9.23 < 9.45 (4) & 10.3 < 10.61 < 10.81 (7) & 8.04 < 8.65 < 9.20 (12) \\ \text{Model 2} & \text{R} & 6.39 < 6.88 < 7.41 & 10.02 < 10.29 < 10.53 & 11.34 < 11.87 < 12.21 & 9.69 < 9.97 < 10.40 \\ \text{Model 2} & \text{R} & 9.28 < 9.97 < 11.46 (3) & 13.67 < 14.64 < 15.14 (5) & 11.53 < 12.82 < 13.85 (7) & 12.33 < 10.99 \\ \text{Model 2} & \text{R} & 9.28 < 9.97 < 11.46 (3) & 13.67 < 14.64 < 15.14 (5) & 11.53 < 12.82 < 13.85 (7) & 12.30 < 10.99 \\ \text{Model 2} & \text{R} & 13.47 < 14.14 < 14.76 & 16.35 < 17.10 < 17.69 & 16.31 < 17.15 < 17.83 & 9.81 < 10.30 < 10.99 \\ \text{Model 2} & \text{R} & 10.10 < 10.66 < 11.28 & 16.85 < 17.39 < 18.11 & 15.94 < 16.59 < 17.10 & 13.60 < 14.22 < 14.81 \\ \text{Model 2} & \text{R} & 10.10 < 10.66 < 11.28 & 16.85 < 17.39 < 18.11 & 15.94 < 16.59 < 17.10 & 13.60 < 14.22 < 14.81 \\ \text{Model 3} & \text{R} & 10.10 < 10.66 < 11.28 & 16.85 < 17.39 < 18.11 & 15.94 < 16.59 < 17.10 & 13.60 < 14.22 < 14.81 \\ \text{Model 4} & R$		Model 2	L	7.31 < 7.62 < 7.94	5.70 < 5.98 < 6.22	7.51 < 7.89 < 8.21	7.30 < 7.59 < 7.71
			R	7.19 < 7.51 < 7.81	7.59 < 7.93 < 8.29	5.31 < 5.58 < 5.84	7.54 < 8.06 < 8.34
$ \begin{array}{c ccccccccccccccccccccccccccccccccccc$	DCT1	Model 1	L	11.65 < 12.45 < 13.40 (3)	13.03 < 13.49 < 13.84 (4)	12.42 < 12.95 < 13.45 (7)	12.39 < 13.02 < 13.78 (10)
$ \begin{array}{c ccccccccccccccccccccccccccccccccccc$			R	11.70 < 12.33 < 12.87 (3)	11.98 < 12.52 < 12.91 (4)	13.15 < 13.78 < 14.3 (7)	11.07 < 11.75 < 12.42 (10)
$ \text{DCT2} = \begin{bmatrix} \text{Model 1} & \text{L} & 13.65 < 14.16 < 14.42 & 14.48 < 14.85 < 15.27 & 15.45 < 15.75 < 16.11 & 13.66 < 13.92 < 14.54 \\ & 14.79 < 15.15 < 15.49 \ (1) & 15.94 < 16.27 < 16.64 \ (4) & 14.70 < 15.08 < 15.42 \ (7) & 15.94 < 16.42 < 16.82 \ (10) \\ \hline & 15.6 < 16.1 < 16.37 \ (1) & 14.42 < 14.44 < 14.71 \ (4) & 16.83 < 17.30 < 17.6 \ (7) & 14.32 < 14.34 < 14.4 \ (10) \\ \hline & 16.83 < 17.30 < 17.6 \ (7) & 14.32 < 14.34 < 14.4 \ (10) \\ \hline & 16.83 < 17.30 < 17.6 \ (7) & 14.32 < 14.34 < 14.4 \ (10) \\ \hline & 16.83 < 17.30 < 17.6 \ (7) & 14.32 < 14.34 < 14.4 \ (10) \\ \hline & 17.45 < 17.91 < 18.37 & 17.43 < 17.75 < 18.06 & 17.31 < 17.78 < 18.11 & 17.51 < 17.98 < 18.48 \\ \hline & 17.02 < 17.41 < 17.75 & 17.65 < 18.00 < 18.21 & 18.31 < 18.78 < 19.24 & 17.84 < 18.08 < 18.43 \\ \hline & 17.09 < 8.27 < 9.08 \ (3) & 8.84 < 9.23 < 9.45 \ (4) & 10.3 < 10.61 < 10.81 \ (7) & 8.04 < 8.65 < 9.20 \ (12) \\ \hline & 10.65 < 10.91 < 11.27 & 10.63 < 11.06 < 11.52 & 10.01 < 10.30 < 10.52 & 9.51 < 9.96 < 10.27 \\ \hline & 10.04 < 10.32 < 10.20 & 10.29 < 10.53 & 11.34 < 11.87 < 12.21 & 9.69 < 9.97 < 10.40 \\ \hline & 10.34 < 11.87 < 12.21 & 9.69 < 9.97 < 10.40 \\ \hline & 10.34 < 11.87 < 12.21 & 9.69 < 9.97 < 10.40 \\ \hline & 10.34 < 11.87 < 12.21 & 9.69 < 9.97 < 10.40 \\ \hline & 10.34 < 11.87 < 12.21 & 9.69 < 9.97 < 10.40 \\ \hline & 10.34 < 11.87 < 12.21 & 9.69 < 9.97 < 10.40 \\ \hline & 10.34 < 11.87 < 12.21 & 9.69 < 9.97 < 10.40 \\ \hline & 10.34 < 11.87 < 12.82 < 13.85 \ (7) & 12.33 < 12.46 < 12.95 \ (12) \\ \hline & 10.01 < 10.66 < 11.28 & 16.85 < 17.10 < 17.69 & 16.31 < 17.15 < 17.83 & 9.81 < 10.30 < 10.99 \\ \hline & 16.31 < 17.15 < 17.83 & 9.81 < 10.30 < 10.99 \\ \hline & 16.31 < 17.15 < 17.83 & 9.81 < 10.30 < 10.99 \\ \hline & 10.34 < 11.10 < 10.66 < 11.28 & 16.85 < 17.39 < 18.11 & 15.94 < 16.59 < 17.10 & 13.60 < 14.22 < 14.81 \\ \hline & 10.10 < 10.66 < 11.28 & 16.85 < 17.39 < 18.11 & 15.94 < 16.59 < 17.10 & 13.60 < 14.22 < 14.81 \\ \hline & 10.10 < 10.66 < 11.28 & 16.85 < 17.39 < 18.11 & 15.94 < 16.59 < 17.10 & 13.60 < 14.22 < 14.81 \\ \hline & 10.10 < 10.66 < 11.28 & 16.85 < 17.39 < 18.11 & 15.94 < 16.59 < 17.10 & 13.60 < 14.22 < 14.8$	DOTT	Model 2	L	14.59 < 14.92 < 15.31	14.56 < 14.88 < 15.21	14.29 < 14.66 < 15.01	13.78 < 14.24 < 14.60
			R	13.65 < 14.16 < 14.42	14.48 < 14.85 < 15.27	15.45 < 15.75 < 16.11	13.66 < 13.92 < 14.54
$ \begin{array}{c ccccccccccccccccccccccccccccccccccc$	DCT2	Model 1	L	14.79 < 15.15 < 15.49 (1)	15.94 < 16.27 < 16.64 (4)	14.70 < 15.08 < 15.42 (7)	15.94 < 16.42 < 16.82 (10)
$ \begin{array}{c ccccccccccccccccccccccccccccccccccc$			R	15.6 < 16.1 < 16.37 (1)	14.42 < 14.44 < 14.71 (4)	16.83 < 17.30 < 17.6 (7)	14.32 < 14.34 < 14.4 (10)
$ DCT3 = \begin{bmatrix} Model \ 1 & L & 8.90 < 9.10 < 9.44 \ (3) & 8.84 < 9.23 < 9.45 \ (4) & 10.3 < 10.61 < 10.81 \ (7) & 8.04 < 8.65 < 9.20 \ (12) \\ \hline Model \ 2 & L & 10.65 < 10.91 < 11.27 & 10.63 < 11.06 < 11.52 & 10.01 < 10.30 < 10.52 & 9.51 < 9.96 < 10.27 \\ \hline Model \ 1 & L & 12.03 < 12.53 < 13.29 \ (3) & 13.23 < 14.02 < 14.61 \ (4) & 12.56 < 13.77 < 14.57 \ (8) & 8.42 < 9.22 < 9.85 \ (10) & 8.04 < 8.65 < 9.20 \ (12) & 10.01 < 10.30 < 10.52 & 9.51 < 9.96 < 10.27 \\ \hline Model \ 2 & R & 6.39 < 6.88 < 7.41 & 10.02 < 10.29 < 10.53 & 11.34 < 11.87 < 12.21 & 9.69 < 9.97 < 10.40 \\ \hline Model \ 1 & R & 9.28 < 9.97 < 11.46 \ (3) & 13.67 < 14.64 < 15.14 \ (5) & 11.53 < 12.82 < 13.85 \ (7) & 12.33 < 12.46 < 12.95 \ (12) & 12.03 < 12.53 < 12.46 < 12.95 \ (12) & 12.03 < 12.54 < 12.95 \ (12) & 12.03 < 12.54 < 12.95 \ (12) & 12.03 < 12.46 < 12.95 \ (12) & 12.347 < 14.14 < 14.76 & 16.35 < 17.10 < 17.69 & 16.31 < 17.15 < 17.83 & 9.81 < 10.30 < 10.99 \\ \hline Model \ 2 & R & 10.10 < 10.66 < 11.28 & 16.85 < 17.39 < 18.11 & 15.94 < 16.59 < 17.10 & 13.60 < 14.22 < 14.81 \\ \hline \end{tabular}$		Model 2	L	17.45 < 17.91 < 18.37	17.43 < 17.75 < 18.06	17.31 < 17.78 < 18.11	17.51 < 17.98 < 18.48
			R	17.02 < 17.41 < 17.75	17.65 < 18.00 < 18.21	18.31 < 18.78 < 19.24	17.84 < 18.08 < 18.43
$ \begin{array}{c ccccccccccccccccccccccccccccccccccc$	DCT3	Model 1			9.74 < 10.13 < 10.20 (4)	8.67 < 9.02 < 9.36 (7)	8.42 < 9.22 < 9.85 (10)
$ \begin{array}{c ccccccccccccccccccccccccccccccccccc$			R	7.09 < 8.27 < 9.08 (3)	8.84 < 9.23 < 9.45 (4)	10.3 < 10.61 < 10.81 (7)	8.04 < 8.65 < 9.20 (12)
		Model 2	L	10.65 < 10.91 < 11.27	10.63 < 11.06 < 11.52	10.01 < 10.30 < 10.52	9.51 < 9.96 < 10.27
			R	6.39 < 6.88 < 7.41	10.02 < 10.29 < 10.53	11.34 < 11.87 < 12.21	9.69 < 9.97 < 10.40
$ \begin{array}{c ccccccccccccccccccccccccccccccccccc$	DCT//*	Model 1	L		13.23 < 14.02 < 14.61 (4)	12.56 < 13.77 < 14.57 (8)	8.42 < 9.20 < 10.88 (12)
$ \begin{array}{c ccccccccccccccccccccccccccccccccccc$			R		13.67 < 14.64 < 15.14 (5)		12.33 < 12.46 < 12.95 (12)
R 10.10 < 10.66 < 11.28 16.85 < 17.39 < 18.11 15.94 < 16.59 < 17.10 13.60 < 14.22 < 14.81	1014	Model 2	L				
			R		16.85 < 17.39 < 18.11	15.94 < 16.59 < 17.10	13.60 < 14.22 < 14.81

^{*} no Stage I crack growth in DCT4



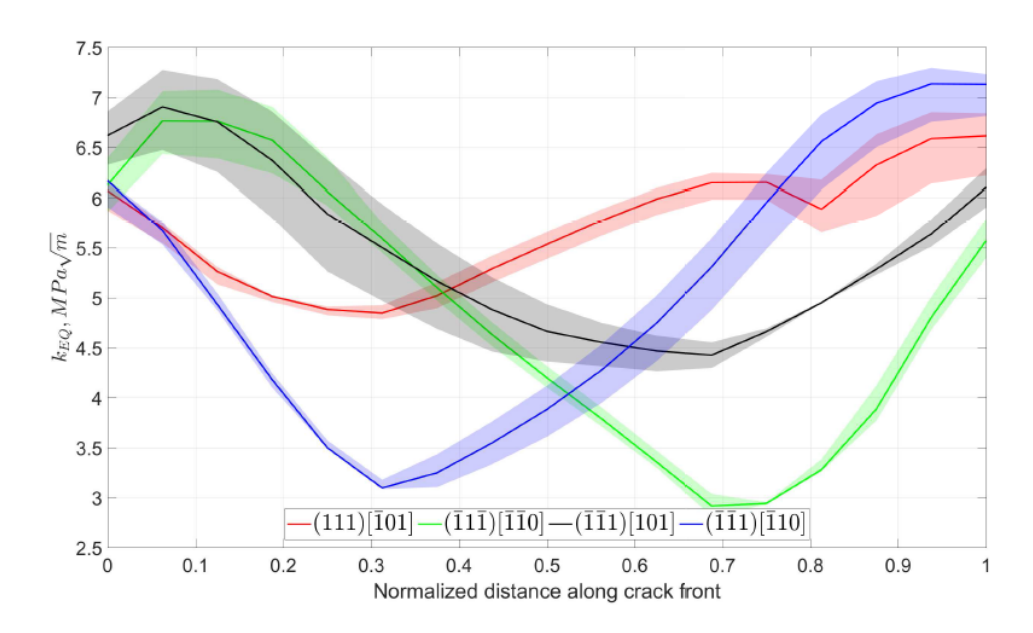


Figure 66 - The k_{EQ} parameter evaluated by Model 1 as a function of normalised crack growth distance for two slip systems giving the highest values on each side of the model for Kb4 at the transition crack length 1 mm with the corresponding crack depth of 0.9 mm.

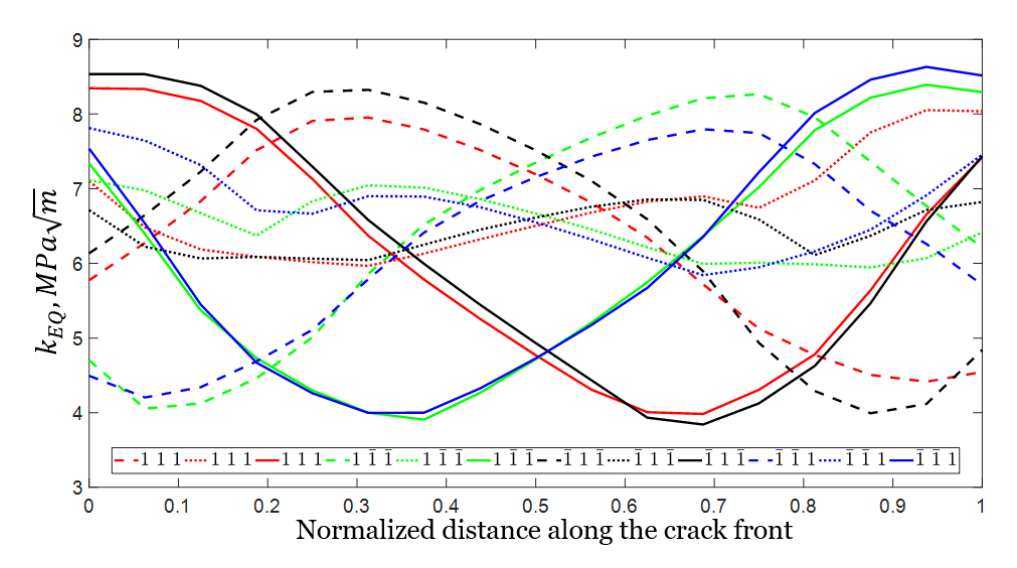


Figure 67 - The k_{EQ} parameter evaluated by Model 1 as a function of normalised crack growth distance for all slip systems for Kb1 at the transition crack length



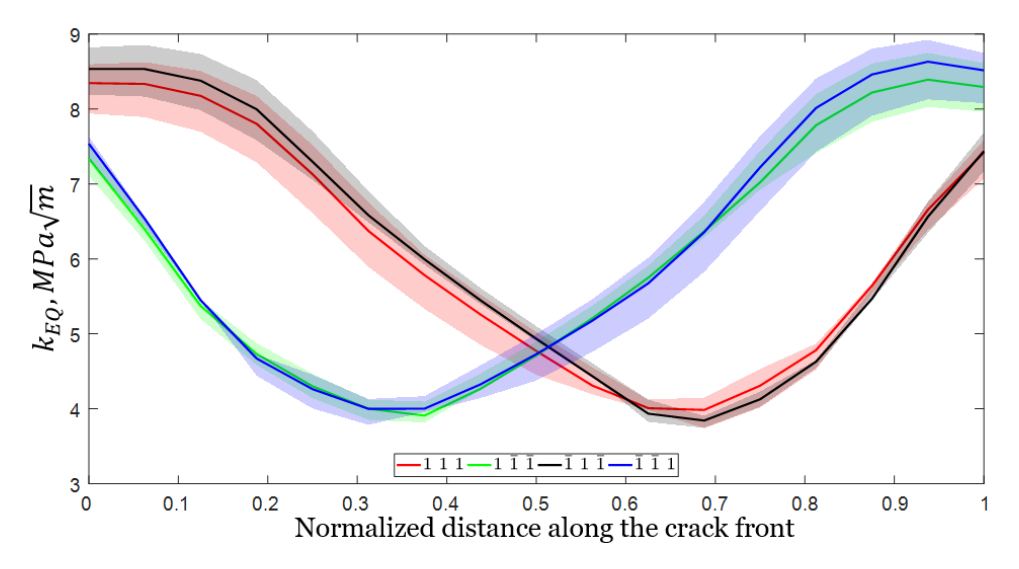


Figure 68 - The k_{EQ} parameter evaluated by Model 1, including the scatter ranges, as a function of normalised crack growth distance for two slip systems giving the highest values on each side of the model for Kb1 at the transition crack length

It can be stated that the above presented method to predict the crystallographic cracking planes was able to successfully predict the correct active crystallographic cracking plane in all cases. The values of the calibration parameters ψ_{\perp} I,II,III were chosen to fit the experimental results from the DCT specimens based on the FE-simulations of the DCT model. This was done by an iterative fitting of the calculated RSIF parameters in relation to the observed experimental crystallographic cracking planes. The calibration parameters were then used to predict the Stage I cracking plane in the Kb specimens. Fitting to the DCT specimens was done due to fewer specimens with crystallographic crack growth compared to the Kb specimens; and that the circumstances regarding the simulation set-up and evaluation procedure were more complicated. For Model 1, $\psi_{I,II,II}$ is equal to 0.1, 1, 1 and for Model 2 0.2, 1, 1. From the values of the calibration parameters it can be concluded that the resolved shear stresses (kii and kiii) as well as the normal stress (k₁) to the crystallographic slip plane are of importance. It should be stated that the execution time of Model 2 is substantially higher than the one of Model 1, since a lot more directions have to be evaluated. In addition, the angle between the evaluation direction in Model 2, which gives the highest keq value (red direction vector), and the Burgers' vectors (positive and negative) in Model 1 (black direction vectors) is schematically depicted in Figure 69. The inserted symbols represent the angle between the direction vector resulting in the highest keq value in Model 2 and the three Burgers' vectors on the active crystallographic cracking plane ("11") according to Model 1 for DCT1. It can be seen that in an interval between 0.61 and 0.83 of the normalised crack front, the evaluation direction, which gives the highest keq value in Model 2, switches direction and thus the angles to the Burgers' vector change. Apart from the mentioned interval, it can be noted that the depicted angles as a function of normalised distance along the crack front are continuous with a continuous first derivative and are almost constant. The minimum angle is always around 20°-30°, meaning that the maximum keq -direction will never coincide with the favoured slip directions (Burgers' directions) with the least material resistance to slip, as in Model 1. This study focuses on the prediction of the active Stage I cracking planes from a planar crack front perpendicular to the loading direction. However, the results suggest that Model 1 and 2, with the proposed RSIF parameter k_{EQ}, are promising candidates to also serve as a foundation for quantifying the



transition between Stage II and Stage I cracking and to predict the Stage I crack growth behaviour.

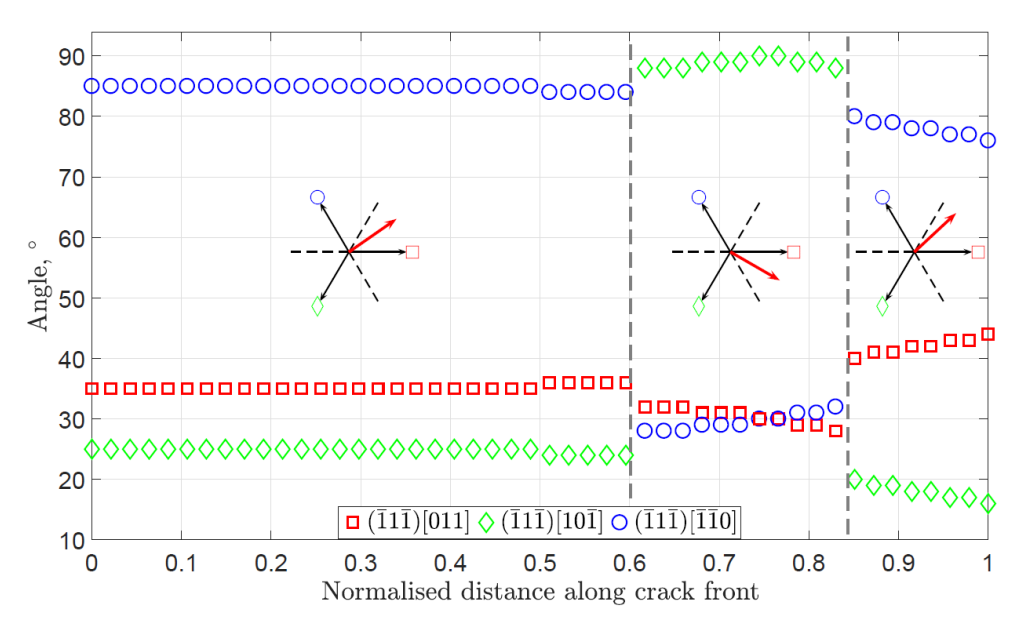


Figure 69 - Angle between maximum k_{EQ} (red direction vector) in Model 2 and the three Burgers' vectors on the $(\bar{1}1\bar{1})$ -plane along the normalised crack front for DCT1 at the transition crack length 2.6 mm.

Some difficulties should be noted while evaluating the presented RSIF parameter. One difficulty lies in the evaluation of the crystallographic misalignments of the specimens, which are measured from the dendrites' projections on the surface of the specimens, where measuring inaccuracies can cause errors. It should be kept in mind that this issue will also occur in real applications where it is often difficult to determine the secondary crystallographic orientation. Furthermore, the crack front shape before transition from Stage II to Stage I cracking was only idealised and assumed to be semi-circular and semi-elliptical, respectively. The actual crack front shape can deviate from this and therefore change the stress field around the crack tip, thus influencing the results.



4 Conclusions

The main conclusions from the experimental work are summarized below:

- From the isothermal tests the following conclusion has been drawn:
 - The crack growth rate increases with increasing testing temperature in the tested temperature range of 20–750 °C.
 - o In the 20 °C tests, non-crystallographic crack growth was dominant. Crystallographic cracking occurred locally at the side surfaces of the specimens. At the highest stress levels in (0 0 1) specimens, crystallographic secondary cracks could also be found in the interior of the specimens.
 - o For non-crystallographic cracks propagating in Mode I, the difference in noncrystallographic crack growth rate between the different orientations appears to be smaller than the scatter of the results for a certain crystal orientation.
 - The propensity for crystallographic crack growth was highest at the intermediate testing temperature of 500 °C. This behaviour could not be explained by confinement of inelastic strains to the γ matrix based on the temperature dependences of the critical resolved shear stress of the γ and γ' phases respectively. The reason for the noncrystallographic nature of the crack growth at 20 °C remains a topic for future investigation.
 - o In the 500 °C tests partly crystallographic crack growth was observed in the (0 0 1) and (0 1 2) tests, but not in the (0 1 1) tests. The crystallographic cracks initiated at the side surfaces of the specimens, where the stress state was close to plane stress. There was a region in the middle of the crack front where the crack growth remained non-crystallographic throughout the entire test.
 - o In the present tests at 750 °C, the crack growth rate da/dN was observed to increase with increasing hold time at maximum load. The hold time influence decreased with decreasing stress intensity factor range ΔK . For $\Delta K < 30$ MPa*m^{0.5} ($da/dN < 10^{-3}$ mm/cycle), no significant difference in da/dN at 750 °C could be observed between 1 h dwell and 30 s dwell time.
- From the TMF crack propagation tests the following conclusion has been drawn:
 - Material data for the cast polycrystalline nickel-based superalloy IN792 and the single-crystal superalloy STAL15 have been generated by TMF crack growth testing with and without long dwell times. A rigid SEN test specimen capable of negative R-ratio loading has been used.
 - o Under IP-TMF conditions for IN792, a transition from transgranular to intergranular crack propagation was observed as the dwell time increases.
 - IP crack growth rate increase with increasing temperature and length of the dwell, as expected. However, OP crack growth is not to be affected by temperature and dwell if plotted versus ΔK_{ASTM} . OP crack growth is faster than isothermal low temperature data when plotted versus ΔK_{ASTM} .
 - The crack propagation rates for the single-crystal superalloy STAL15 shows similar trends as for the polycrystalline superalloy IN792.



The main conclusions from the modelling work are:

- An effective approach to handle inelastic deformations using linear elastic fracture mechanics has been displayed. The residual stress state from an elasticplastic FE-analysis of an uncracked model is superimposed on a linear elastic crack evaluation of the corresponding cracked model.
- The stress state in a single-crystal component has to be accounted for by an appropriate material model, especially in the vicinity of a notched feature where the complexity increases and the likeliness of crack initiation and subsequent propagation increases.
- The crystal orientation is important when evaluating the stress intensity factors, since an anisotropic effect is present in the component. Furthermore, it is important to account for the misalignments in a cast component, since the orientation will have a major influence on the crack propagation behaviour.
- The developed crystallographic crack driving force parameter k_{EQ} is able to successfully predict the active crystallographic cracking plane after transitioning from an initially global Mode I crack.
- This developed crystallographic crack driving force parameter can be used in an
 industrial crack growth assessment procedure that will contribute in making life
 predictions more accurate. Hence, leading to less conservative safety margins.



5 Goal fulfilment

The overall research goals of this project are given below and the fulfilment of each of them are disscussed:

- 1. Validation of a TMF crack growth test method that can be used to generate high quality data for cast nickel-based superalloys, including single-crystals.
 - This goal is fulfilled since a large number of TMF crack growth tests have been conducted on two different alloys and compared to isothermal tests. Overall the data shows an accaptable degree of scatter, comparable to the scatter found in standardized isothermal tests. The data in general show a good consistency between different test conditions (Temperatures, load vs strain control, dwell time etc) and the repeatability is found to be good.
- 2. Generation of high quality test data for TMF crack growth in conventionally cast IN792 and the single-crystal superalloy STAL15.
 - This goal is fulfilled since enough data has been generated in order to start developing a model describing the TMF crack growth behaviour under various temperature ranges and dwell times for the two different alloys. Of course, more testing will always lead to better statistics and more accurate models.
- Improvement of the knowledge regarding the mechanisms that controls the crack growth rate for conventionally cast superalloys as well as for single-crystal superalloys (e.g. influence of crystal orientation, phase shift and temperaturestrain history).
 - This goal is fulfilled at least in that sense that an improvement has been made regarding the understanding of the mechanisms controlling the crack growth mechanisms. As always, good research gives at lot of new questions that needs further investigation. These are highlighted in the next section.
- 4. Development of TMF crack growth models and life prediction methodologies that will reduce the need high safety margins. Today the safety of single-crystal crack growth is in the order of three decades. The idea is to bring this order of magnitude down by one decade.
 - A first stage of this goal has been fulfilled, regarding the driving force for the crystallographic crack propagation model. This will contribute in making life predictions of single-crystal components more accurate, leading to less conservative safety margins. The developed crack growth model correlates well with the observed experimental behaviour for the investigated aspects, despite the high complexity which is involved in modelling the crack growth behaviour in single-crystal nickel-base superalloys. Furthermore, new questions have arisen during the project, which need to be handled prior fulfilment, see the next section.
- 5. Validation of the models for component near conditions.
 - This is ongoing work at Siemens Industrial Turbomachinery AB.



6 Suggestions for future research work

6.1 EXPERIMENTAL WORK

A more in-depth evaluation of the crack propagation mechanism during OP-TMF loading is needed in order to fully understand the behaviour of cast superalloys under this type of loading conditions. No rational explanation exists to the observation that neither temperature nor dwell time has a significant effect on the crack propagation rate. Also, the significant difference between isothermal tests and the OP TMF-tests is a bit puzzling and needs further investigation.

The effect of long term ageing, which is known to degrade the microstructure of cast and γ' strengthened superalloys, needs to be investigated further. Furnace exposure and testing is ongoing but needs to be evaluated.

Other phases shifts during TMF than IP and OP will probably be of interest to investigate in the future in order to have material data and models covering all possible thermal and load histories that can occur in real applications.

6.2 MODELLING WORK

From a modelling context the entire research question regarding crack growth in singlecrystal nickel-base superalloys is related to the development of a methodology for predicting the crack propagation behaviour. This can be summarised into: When, where and how? As seen in the above presented work within the KME-702 project, the crack has transitioned from a Mode I crack onto a crystallographic slip plane and continued to expand there. Hence, the moment when the crack transition takes place is of interest and plays an important role in the crystallographic cracking framework. An idea here is that the previous loadings will damage the slip planes and consequently "open-up" for a crack to grow more easily on the most damaged plane. This is closely coupled to the plastic deformation which is governed by shear stresses on the internal slip systems as is also the developed crack driving force parameter keq. Thus, a transition criterion has to be defined and calibrated for the material in question. The most damaged crystallographic slip plane is likely where the crack will continue to grow on. This specific crystallographic plane has already been identified during the completed KME-702 project with the developed k_{EQ} -parameter. Hence, utilisation of this in conjunction with a transition criterion will be able to predict the observed transition behaviour. After the transition, as can been seen from the fracture surface evaluations, the crystallographic crack front shape is more hyperbolic and advancing at a higher rate compared to the Mode I crack front. Hence, an evaluation of how the crack length and propagation rate on the crystallographic slip planes develop is necessary to be able to quantify a Paris' law expression for single-crystal nickel-base superalloys. Furthermore, the entire crack front is divided into pure Mode I and crystallographic cracking regions, and thus a mixed type of global response is present, and need to be represented in the model.



It is to be pointed out that the modelling work is, and will be, developed in close conjunction with the inherent internal structure of the single-crystal superalloy, where the crystallographic slip planes and slip directions are staging the arena.

Research questions:

- When: Crystallographic transition criterion
- Where: Crystallographic slip plane (completed)
- How: Crystallographic crack propagation rate and crack length development (on-going)



7 Literature references

- [1] Nazmy M, Denk J, Baumann R, Künzler A. Scr Mater 2003;48:519.
- [2] Leggett AJ, Simms NJ, Rickerby DS. Turbine Blade Coating Selection for Sulphidation Resistance, in: Parsons 2007. UK: IOM; 2007.
- [3] Zhang JX, Harada H, Koizumi Y, Kobayashi T. Scr Mater 2009;61:1105.
- [4] Moverare J, Johansson S, Reed RC. Acta Mater 2009;57:2266.
- [5] Moverare JJ, Johansson S. Mater Sci Eng A 2010;527:553.
- [6] Segersäll M, Moverare JJ, Simonsson K, Johansson S. Deformation and Damage Mechanisms During Thermomechanical Fatigue of a Single---Crystal Superalloy in the <001> AND <011> Directions, in: Superalloys 2012. 2012.
- [7] Kersey RK, Staroselsky A., Dudzinski DC, Genest M. Int J Fatigue 2013;55:183.
- [8] Okazaki M, Sakaguchi M, Yamagishi S. Procedia Eng 2013;55:677.
- [9] Bouvard JL, Gallerneau F, Paulmier P, Chaboche JL. Int J Fatigue 2012;38:130.
- [10] Zhao J, Wu X, Liu R, Zhang Z. Eng Fract Mech 2004;71:1873.
- [11] Leidermark D, Moverare J, Johansson S, Simonsson K, Sjöström S. Acta Mater 2010;58:4986.
- [12] Neuner F, Tetzlaff U, Mughrabi H. Enhancement of Thermo---Mechanical Fatigue Resistance of a Monocrystalline Nickel---Base Superalloy by Pre---Rafting, in: ASTM STP 1428. ASTM International; 2003
- [13] Reed RC, Moverare J, Sato A, Karlsson F, Hasselqvist M. A New Single-crystal Superalloy for Power Generation Applications, in: Superalloys 2012. 2012.
- [14] Ewest D, Almroth P, Sjödin B, Simonsson K, Leidermark D, Moverare J, Int J Fatigue 2016;92:61.
- [15] Newman Jr J.C., "Stress-intensity factors and crack-opening displacements for round compact specimens", International journal of fracture, Vol. 17, No. 6, December 1981.
- [16] Chan K.S. and Cruse T.A., "Stress intensity factors for anisotropic compacttension specimens with inclined cracks", Engineering fracture mechanics, Vol. 23, No. 5, pp. 863-874, 1986
- [17] Tinga T., "Stress intensity factors and crack propagation in a single-crystal nickel-based superalloy", Engineering Fracture Mechanics 73, 2006.
- [18] Antolovich B.F., Saxena A. and Antolovich S.D., "Fatigue Crack Propagataion in Single-Crystal CMSX-2 at Elevated Temperature", Journal of materials engineering and performance, Vol. 2, pp 489-496, 1993
- [19] Mathworks, Matlab 2014b, 2000.
- [20] Abaqus, ABAQUS 6.12 Documentation. Providence, USA: Dassault Systèmes, 2014
- [21] FRANC3D, FRANC3D Reference Manual. Ithaca, USA: Fracture Analysis Consultants Inc., 2016.
- [22] Busse C., Gustafsson D., Rasmusson P., Sjödin B., Moverare J.J., Simonsson K., Leidermark D., Three-Dimensional LEFM Prediction of Fatigue Crack Propagation in a Gas Turbine Disk Material at Component Near Conditions (2016) Journal of Engineering for Gas Turbines and Power, 138 (4), pp. 042506-1-8.
- [23] Busse C., Loureiro Homs J., Gustafsson D., Palmert F., Sjödin B., Moverare J.J., Simonsson K., Leidermark D., A Finite Element Study of the Effect of Crystal Orientation and Misalignment on the Crack Driving Force in a Single-Crystal Superalloy (2016) ASME Turbo Expo 2016: Turbine Technical Conference and Exposition, 7A, pp. V07AT28A002.



- [24] Telesman J., Ghosn L.J., Fatigue crack growth behavior of PWA 1484 single crystal superalloy at elevated temperatures, Journal of Engineering for Gas Turbines and Power 118 (1996) 399–405.
- [25] Anderson T.L., Fracture mechanics: fundamentals and applications, 3rd ed., CRC Press, Boca Raton, 1995.
- [26] Wawrzynek P.A., Carter B.J., Banks-Sills L., The M-integral for computing stress intensity factors in generally anisotropic materials, NASA, Marshall Space Flight Center, Huntsville, USA, 2005.
- [27] Hoenig A., Near-tip behavior of a crack in a plane anisotropic elastic body, Engineering Fracture Mechanics 16 (1982) 393–403.
- [28] Busse C., Palmert F., Sjödin B., Almroth P., Gustafsson D., Simonsson K., Leidermark D. (2017). Prediction of crystallographic cracking planes in a singlecrystal nickel-base superalloy. To be submitted.
- [29] Askeland D.R., Phule P.P., The Science and Engineering of Materials, fifth edit ed., Thomson, Canada, Toronto, 2006.
- [30] Pope DP, Ezz SS, Mechanical properties of Ni3Al and nickel-base alloys with high volume fraction of gamma prime, International metals reviews 29 (1984) 136–167.
- [31] Leidermark D, Moverare J, Simonsson K, Sjöström S, Johansson S. Comput Mater Sci., 2009;47:366.
- [32] Laird, C., Smith, G.C. "Crack propagation in high stress fatigue", Philosophical Magazine 8, 847-57, 1962.
- [33] Copley S.M., Kear B.H., Rowe G.M., "The temperature and orientation dependence of yielding in Mar-M200 single crystals," *Materials Science and Engineering*, vol. 10, pp. 87–92, 1972.
- [34] Nembach E., "The high temperature peak of the yield strength of γ '-strengthened superalloys," *Materials Science and Engineering: A*, vol. 429, no. 1-2, pp. 277–286, 2006.
- [35] Mulford R.A., Pope D.P., "The yield stress of Ni3(Al, W)," *Acta Metallurgica*, vol. 21, no. 10, pp. 1375–1380, 1973.
- [36] Feller-Kniepmeier M., Link T., Poschmann I., Scheunemann-Frerker G., Schulze C., "Temperature dependence of deformation mechanisms in a single crystal nickel-base alloy with high volume fraction of γ' phase," *Acta Materialia*, vol. 44, no. 6, pp. 2397–2407, 1996.
- [37] Milligan W.W., Antolovich S.D., "Deformation Modeling and Constitutive Modeling for Anisotropic Superalloys", NASA contractor report 4215, 1989
- [38] Reed R.C., "The Superalloys: Fundamentals and applications", Cambridge, 2006
- [39] Kagawa H., Mukai Y., "The Effect of Crystal Orientation and Temperature on Fatigue Crack Growth of Ni-based Single Crystal Superalloy", Superalloys 2012: 12th International Symposium on Superalloys, TMS, 2012
- [40] Sengupta A., Putatunda S.K., "Influence of dynamic strain aging on the near-threshold fatigue crack growth behavior of a new single crystal nickel-based superalloy", Scripta Metallurgica et Materialia, vol. 31, No 9, pp. 1163-1168, 1994.
- [41] Almroth P., Gustafsson D., On thermomechanical fatigue crack growth analysis in gas turbine blading in a 3D finite element context, (2017) Conference: LCF8, Dresden, Germany.
- [42] Kontis P., Collins D.M., Johansson s., Wilkinson A.J., Moverare J.J., Reed R.C., Crack initiation and propagation during thermal-mechanical fatigue of IN792: Effect of dwell time (2016) Superalloys 2016: Proceeding of the 13th International symposioum on Superalloys, pp. 763-772.



8 Publications

Journal and conference papers published within the KME702-project:

- Busse C., Gustafsson D., Rasmusson P., Sjödin B., Moverare J.J., Simonsson K., Leidermark D., Three-Dimensional LEFM Prediction of Fatigue Crack Propagation in a Gas Turbine Disk Material at Component Near Conditions (2016) Journal of Engineering for Gas Turbines and Power, 138 (4), pp. 042506-1-8.
- Busse C., Loureiro Homs J., Gustafsson D., Palmert F., Sjödin B., Moverare J.J., Simonsson K., Leidermark D., A Finite Element Study of the Effect of Crystal Orientation and Misalignment on the Crack Driving Force in a Single-Crystal Superalloy (2016) ASME Turbo Expo 2016: Turbine Technical Conference and Exposition, 7A, pp. V07AT28A002.
- Kontis P., Collins D.M., Johansson s., Wilkinson A.J., Moverare J.J., Reed R.C., Crack initiation and propagation during thermal-mechanical fatigue of IN792: Effect of dwell time (2016) Superalloys 2016: Proceeding of the 13th International symposioum on Superalloys, pp. 763-772.
- 4. Busse C., Palmert F., Sjödin B., Almroth P., Gustafsson D., Simonsson K., Leidermark D. (2017). Prediction of crystallographic cracking planes in a single-crystal nickel-base superalloy. To be submitted.
- 5. Palmert F., Moverare J., Gustafsson D., Busse C., Fatigue crack growth behaviour of an alternative single-crystal nickel base superalloy (2018) International Journal of Fatigue, 109, pp. 166-181.
- Almroth P., Gustafsson D., On thermomechanical fatigue crack growth analysis in gas turbine blading in a 3D finite element context, (2017) Conference: LCF8, Dresden, Germany.
- 7. Westin P., SGT-800B1/B2/B2M Blade 1 and disc 1: Component Near Testing Mechanical Integrity Calculations, Siemens Industrial Turbomachinery AB, 1CS167643
- 8. Segersäll M., Kontis P., Pedrazzini S., Bagot P.A.J., Moody M.P., Moverare J.J., Reed R.C., Thermal-mechanical fatigue behaviour of a new single-crystal superalloy: Effects of Si and Re alloying (2015) Acta Materialia 95,12102, pp. 456-467
- 9. Segersäll M., Leidermark D., Moverare J.J., Influence of crystal orientation on the thermomechanical fatigue behaviour in a single-crystal superalloy (2015) Materials Science and Engineering A 623, pp. 68-77
- Leidermark D., Moverare J., Comparative Analysis of Stress Relaxation and Creep in a Single-Crystal Superalloy (2016) ASME Turbo Expo 2016: Turbine Technical Conference and Exposition, 7A, pp. V07AT28A005.
- 11. Busse C, Aspects of Crack Growth in Single-Crystal Nickel-Base Superalloys, (2017) Licentiate thesis, Linköping University.



LCF AND TMF CRACK GROWTH IN CAST NICKEL-BASED SUPERALLOYS, KME-702

In this project, crack growth during thermomechanical fatigue in two different types of cast nickel-based alloys for turbine blades have been investigated. One of them is a newly developed alloy specially designed for industrial gas turbines to meet the challenges of increasing demand for flexibility and cyclic operation. As the alloy is a so-called single-crystal, completely without grain boundaries, crack growth differs significantly from conventional materials. Among other things, these materials show two distinctly different modes of crack propagation behaviour as the crack under certain load and temperature conditions changes to a crystallographic failure mode. In the project, this behaviour has been mapped for a variety of temperature and load conditions.

The results from material studies and mechanical testing have been used to develop a new calculation methodology and new fracture mechanics parameters for crack growth in material for gas turbine blades.

Results from the project are already implemented by Siemens Industrial Turbomachinery AB, in their development of new turbines focusing on fuel flexibility and cyclical operation.

Energiforsk is the Swedish Energy Research Centre — an industrially owned body dedicated to meeting the common energy challenges faced by industries, authorities and society. Our vision is to be hub of Swedish energy research and our mission is to make the world of energy smarter. www.energiforsk.se

